Detection of Aerosols *via* Coalescence Capture

Lillian Rose Manzoni

A dissertation submitted to the University of Bristol in accordance with the requirements of the degree of Master of Research in the School of Chemistry, Faculty of Science

August 2018

37500 words

Abstract

The detection of Chemical Warfare Agents, CWAs is vital in order to reduce the life limiting and harmful effects of CWAs on the surrounding populations. The work in this thesis was done to further assess the potential of the aerosol optical tweezers (AOT) approach for the real time sampling of CWAs. This application of the AOT technique is unique and the detection of CWAs in real time, with low false alarm rate and high sensitivity, is difficult to achieve. There are a limited number of techniques which can detect aerosol phase CWAs and the AOT technique was found to have potential in this application. To assess the potential for application to this problem, the baseline sensitivity of the AOT technique was established using statistical and experimental analyses. The baseline sensitivity was determined, on both a commercially built system and a purpose-built research grade instrument. The two instruments were compared and a protocol for assessing the sensitivity of future AOT instruments was established. As part of the sensitivity analysis, using an Allan variance analysis, the components of noise in an AOT dataset were characterised and the optimal sampling time of 40 seconds per spectra was determined, and the recommended probe droplet size range was 4 – 5 micrometres.

Additionally, this work investigated the physical design constraints of an AOT instrument for the detection of CWAs. A range of methods for delivering humidifying gas flow, and sample aerosol to a probe droplet were compared. It was recommended that the sample aerosol is delivered as a minor component of a gas flow. Finally, this work performed accretion measurements on an AOT instrument with observed accretion rates of between 1.7×10^{-4} to 0.2 pg s^{-1}. The sampling aerosol, the probe droplet, was exposed to was characterised using an optical particle sizer and a Nanoscan scanning mobility particle sizer. This work seeks to fully characterise the noise characteristics of an AOT instrument, and to understand what steps can be taken to improve the sensitivity of the technique. This work seeks to test the ideal layout of the AOT instrument for the detection of an ensemble of aerosol using an optically tweezed droplet.

Acknowledgements

First and foremost, I am grateful to my supervisor, Jonathan, who has been fantastic in supporting me during my master's project. Thank you for all your support and guidance throughout these projects.

I am also grateful to the wonderful BARC group. To the big office, ridiculous conversations and catchy catchy minty games aside, you've helped me at every point in this project, thank you all. To the little office, the place I went when I was really stuck, thank you for all of your unwavering patience and guidance.

I think the person who has dealt with most of the fallout from this project was probably Ed, thank you for putting up with me. Thank you for trying to read this for me.

My family, really, they just smile and nod when I talk about science, but I appreciate it. The (non-science) person who reads furthest gets a prize.

And finally, Jacob Powell who plied me with an endless supply of tea and pastries to get me through, thank you.

Author's Declaration

I declare that the work in this dissertation was carried out in accordance with the requirements of the University's Regulations and Code of Practise for Research Degree Programmes and that it has not been submitted for any other academic award. Except where indicated by special reference in the text, the work is the candidate's own work. Work done in collaboration with, or with the assistance of, others, is indicated as such. Any views expressed in the dissertation are those of the author.

SIGNED: ……. DATE: …….

Contents

1. Introduction

1.1. Definition of Aerosols

An aerosol is a liquid or solid dispersed as a particle within a medium of gas.[1] Aerosols are a type of colloid and exist in a meta-stable state due to kinetic limitations governing lifetimes. Within the field of colloids the term aerosol refers to both the particle and the dispersion medium which surrounds it. However, within the field of atmospheric sciences the term aerosol is often used to refer only to the particle. This thesis will refer to an aerosol as the particle only. The dispersion medium will be referred to as the surrounding environment.

Aerosols exhibit a range of physical and chemical properties including; shape, size, composition, phase and mixing state with spatial and temporal distribution. This leads to a vastly dynamic system with the state of an aerosol ever evolving. In the atmosphere, the optical, physical and chemical properties of an aerosol change as it ages. Consequentially, the field of aerosol research is complex and challenging. Aerosol research is pertinent to many areas. Some examples include forecasting changes to the climate and studying the use of aerosols in industry. These research areas tend to be applicable to the global environment and the health of global populations.

1.2. Sources of Aerosols in the Atmosphere

Aerosols can be introduced to the atmosphere from anthropogenic and natural sources or can be formed directly in the atmosphere. There are two methods of emission: primary and secondary. Primary emission is the release of aerosol directly into the atmosphere whereas secondary emission aerosol is formed *in situ* within the atmosphere. Examples of primary natural emissions are sea spray, volcanic eruptions and mineral dusts. The predominant example of primary anthropogenic emissions is through the burning of fossil fuels. An example of the formation of secondary aerosol is through the oxidation of volatile organic compounds (VOCs) which then form particles through the homogeneous or heterogeneous nucleation of the species from the gas phase in the atmosphere.

The type of anthropogenic aerosol which is of most relevance to this thesis is a collection of man-made compounds which have been chemically designed to inflict harm and could be emitted in aerosol form. When released in the aerosol phase these weaponised chemicals

can have catastrophic effects on the surrounding populations. Known in this project as chemical warfare agents (CWAs), a total of 7 compounds have been chosen as exemplar compounds to assess their potential to be detected using the aerosol optical tweezers (AOT) technique.[2]

1.2.1. Aerosol Size and Mass Distributions and the Implications for Detection Sensitivities

The distribution of aerosol within an atmosphere is not constant because the residence times of particles are insufficient for them to become well mixed throughout the atmosphere. Therefore, the concentration of any one type of aerosol is highly varied both spatially and temporally. Aerosol size distribution, lifetimes and populations will have a significant impact on the detection requirements for an instrument designed to detect aerosol phase CWAs. Naturally, it is imperative to determine what lifetime, size distribution, and mass distribution of CWA sample is required to satisfy the instrument detection limits.

Aerosols can exist in a wide range of particle sizes, spanning five orders of magnitude, from nanometre to hundreds of micrometres in diameter. There are three distinct regimes of aerosol size distribution: nucleation, accumulation and coarse mode, as shown in Figure 2.1. Particles smaller than 100 nm are within the nucleation / Aitken mode of size. Particles

which are between 100 – 1000 nm are of the accumulation mode and particles greater than 1000 nm are coarse mode.

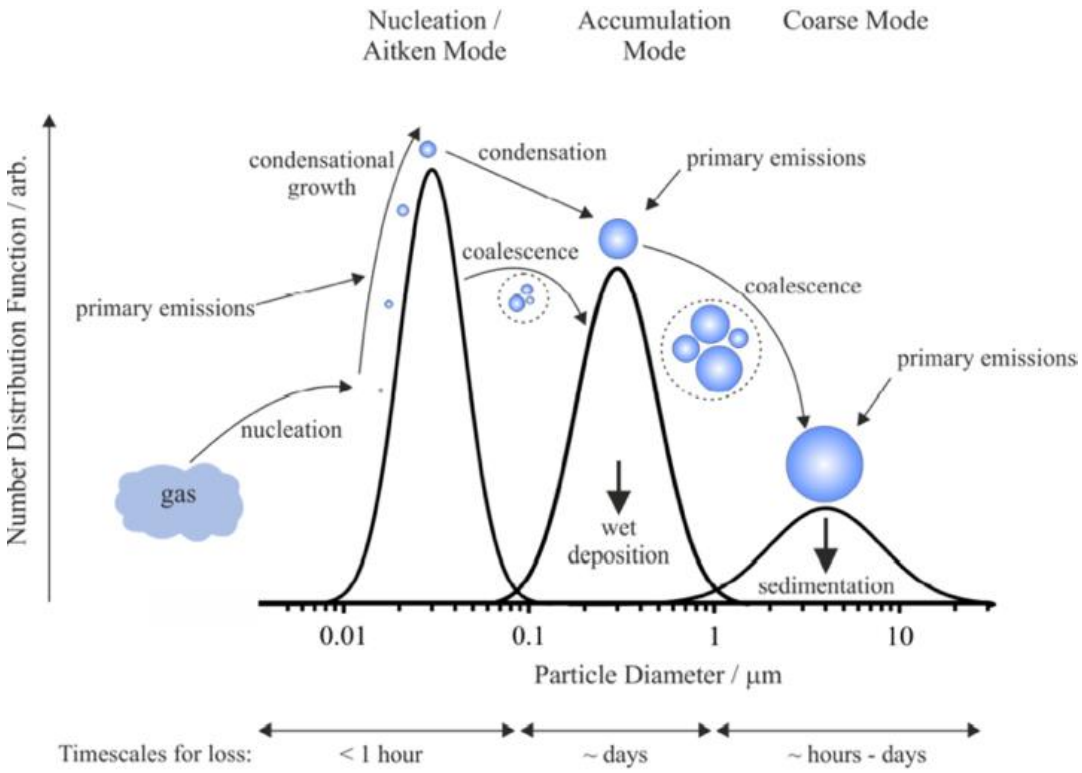

Figure 2.1: A schematic of the production, conversion and terminations for aerosols and the relevance in these mechanisms to particle size.

Particles which are of the coarse mode tend to be produced through resuspension processes, both natural and anthropogenic. Natural aerosols are produced through mechanical processes including the formation of sea spray at the top of a breaking wave, or the erosion of soil and sand. Anthropogenic aerosols are produced through mechanical processes such as construction and transportation. Coarse mode particles tend to be composed of mineral dust, sea salt and industrial and biological fragments. Coarse mode particles tend to originate through primary processes and quickly sediment via dry deposition. The rate of removal is dependent upon the particle specific sedimentation velocity. The sedimentation velocity is determined by the particle density, shape and size and the atmospheric turbulence which surrounds the particle. The larger the coarse mode particle, the shorter its

lifetime. Coarse mode particles remain in the atmosphere for hours, before being removed through sedimentation or deposition.

Accumulation mode particles constitute both a large proportion of the total atmospheric mass and the majority of surface area of aerosol within the atmosphere. Accumulation mode particles can be formed through coalescence of nucleation mode particles, heterogeneous condensation of atmospheric species on to existing aerosol, and primary emissions. The removal of particles in the accumulation mode is less rapid than for coarse or nucleation mode particles. Particles within the accumulation mode tend to live the longest and can remain in the atmosphere for days. The primary method of removal is wet deposition, where aerosol is removed through precipitation. There are two types of wet deposition: the first is wash out, where particles are integrated into cloud droplets which then precipitate; the second is drop out, where particles beneath clouds are consumed by falling rain droplets.

Nucleation mode particles are commonly generated *via* gas-to-particle conversion of low volatility atmospheric vapours, or the high temperature vapours which result from combustion. Nucleation mode particles account for the largest aerosol number density but the limited particle size means the nucleation mode does not contribute a significant amount to the mass fraction or total surface area of atmospheric aerosol. Additionally, these particles have lifetimes shorter than an hour, at which point they tend to coalesce to form accumulation mode particles.

The aerosols discussed in this thesis are accumulation and coarse mode aerosols with sizes between 50 – 1000 nm.

1.2.2. Typical Background Concentration and Size Distributions of Ambient Aerosol

The atmosphere is filled with particles emitted from natural and anthropogenic sources, which are highly varied in concentration. An instrument for detection of CWA will require the ability to account for any background aerosol concentrations. Typical aerosol concentrations in densely populated urban areas, such as large cities, are ~15,000 particles per cm^3.[3] The aerosol profile in a city has a varied composition, constituted primarily of: volatile organic carbons (VOCs), semi-volatile organic carbons (SVOCs), black carbon (BC), brown carbon (BrC), NO_x, SO_2, SO_4^{2-}, CO_3^-, and NH_4^+. Aerosols in densely populated areas have a greater number of particles in the fine and accumulation modes.[4]

Comparatively, the aerosol concentrations in largely unpopulated, natural areas is ~10,000 particles per cm^3.

Table 2.1: A table showing some number concentrations, particle diameters, and geometric standard deviations for aerosols in urban and rural environments. [3,4]

Type	Fine Mode		Accumulation Mode		Coarse Mode	
	N/ cm^3	D_p / μm	N/ cm^3	D_p / μm	N/ cm^3	D_p / μm
Urban	7100	0.012	6320	0.037	960	0.151
Rural	6650	0.015	147	0.05	1990	0.084

The aerosols in unpopulated, rural areas are comprised of mineral dusts from agriculture, pollens and natural aerosols. Aerosols in sparsely populated areas have a greater number of particles in the fine and coarse modes. Aerosols in natural areas tend to be larger, with a more varied size distribution.

As an example, the European Union emission standards for particulate matter > 10 micrometres (PM 10), and > 2.5 micrometres (PM 2.5), are set at an annual mean of 40 and 25 μg m^{-3}, respectively. In the United Kingdom the PM 10 concentrations reported by the department for Environment, Food and Rural Affairs (DEFRA) in 2003 were 20 μg m^{-3} in urban environments, and 16 μg m^{-3} in rural environments. Comparatively the PM 10 concentration was 25 μg m^{-3} at the side of a road.

The AOT technique must be able to resolve a signal of CWA against these background noise levels, which can be immensely varied in different environments.

1.3. CHEMICAL WARFARE AGENTS (CWAS)

1.3.1. OVERVIEW

CWAs are chemical substances which are highly toxic to humans and are therefore designed and used with the intention to harm, harass or kill. There are limited open source publications on CWAs as a result of the difficulty of working with such acutely toxic compounds and the confidential environments in which they are studied for defensive purposes.

CWAs fall into several categories: harassing agents, incapacitating agents, lethal agents (including mustards and arsenicals), choking agents, blood agents and nerve agents. The

nerve agents are some of the most recently developed compounds and, alongside some mustard agents, are the central compounds discussed in this work.

Nerve agents differ from other types of agents because of their phosphonate structure (RO(O=P(R')OR''), a central phosphorus which bonded to three R-groups and a terminal oxide.[5] Organophosphate compounds, such as the nerve agents, irreversibly inhibit the critical acetylcholinesterase enzyme (AChE). Degradation of the AChE enzyme affects all organ systems in the body, rendering the nerve agents highly toxic to humans. There are a large number of nerve agents with R groups varying from a simple fluorine to complex

aminothioalkenes. The chemical structures of the CWAs used in this project as exemplars of compounds with appropriate physiochemical properties shown below in Figure 2.2.

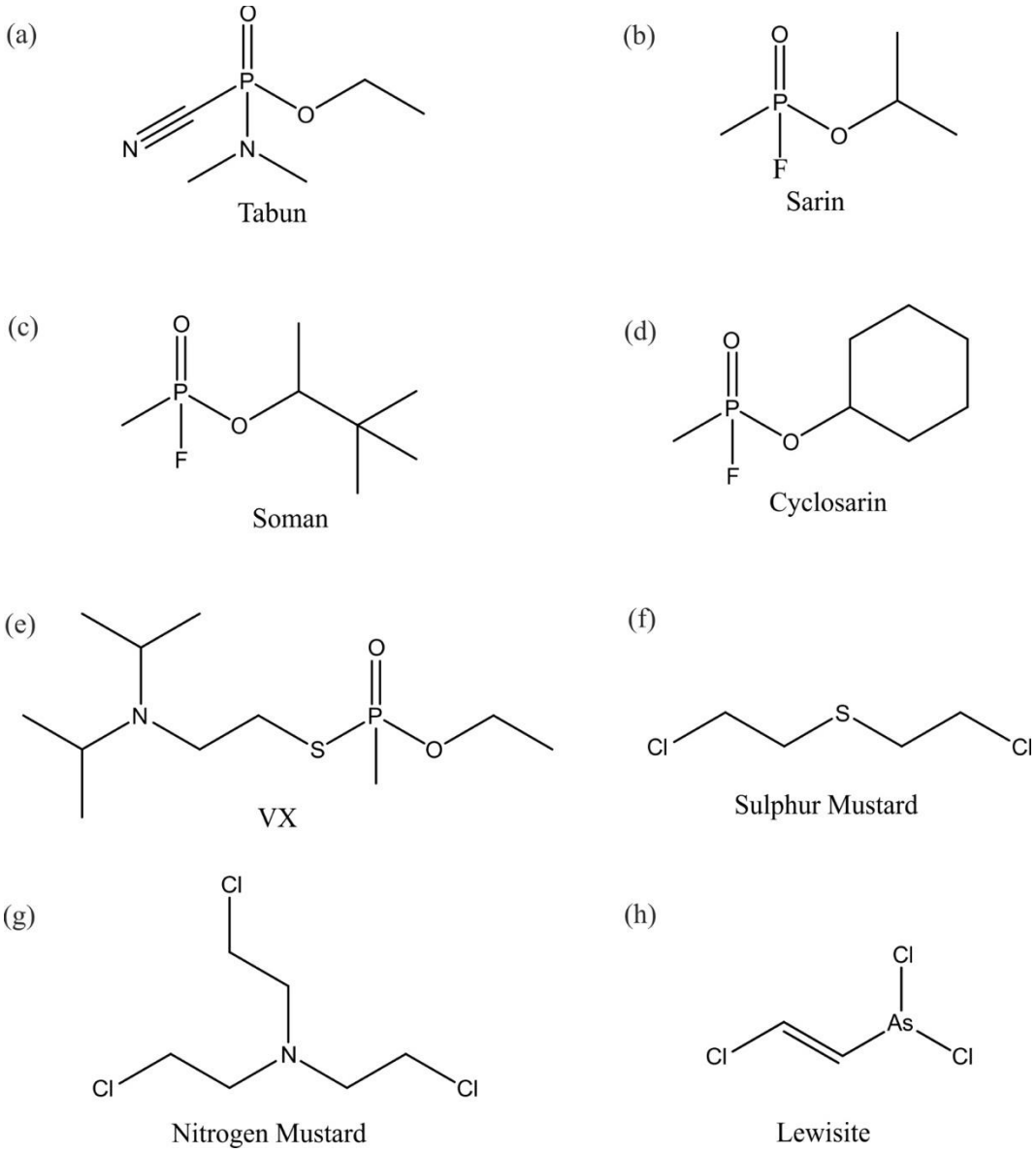

Figure 2.2: A schematic of the CWAs discussed in this work.

CWAs can exist in solid, liquid, aerosol and gas phases and the maximum exposure has a high situational dependence. The multiphase nature of CWAs is a challenging factor in their detection. Detection of CWAs can be *in-situ* or 'on-line', meaning that the technique is deployed in the field and detects immediately. Detection of CWAs can also be 'off-line', whereby a sample is taken and analysed at a later time or in a different location. Both *in-*

situ and off-line methods of detection have uses, but the benefit of *in-situ* methods of detection is the ability to warn of a hazard to enable conservation of life and containment.

1.3.2. EXPOSURE GUIDELINES

To estimate the required detection sensitivities, it is first important to consider the guidelines on exposure. In any analytical approach, the concentration of a CWA in the atmosphere is measured as a function of the time since release. An acute exposure guideline level (AEGL) value is a measure of the threshold exposure limit for a harmful substance.[6] An AEGL-3 value is a reported concentration, in parts per billion, which is the highest concentration of a compound that will not cause death or life-threatening health effects to the surrounding populations. The required sensitivity level for the AOT technique in this project will be set by the detection of CWAs at concentrations identified by AEGL-3 values for a 10 minute exposure period. These values are shown in Table 2.2.

Table 2.2: A table of the AEGL-3 values for the 7 CWAs discussed in this thesis.[6]

Compound	AEGL-3 (10 min exposure)/ ppbv
VX	2.7
Sarin	64
Tabun	110
Soman	49
Cyclosarin	53
Sulphur Mustard	590
Nitrogen Mustard	260

1.4. DETECTION OF CWAS

1.4.1. THE PROBLEM

When faced with the catastrophic consequences of these compounds it is essential to detect them very quickly. There is an aspiration to develop a real-time detector capable of warning of the presence of an aerosol and/or vapour hazard with high specificity and sensitivity to enable appropriate subsequent actions, such as the donning of personal protective equipment (PPE), the administration of medical countermeasures and decontamination, to be performed- as described below.

Techniques for sensing CWAs have to fulfil a significant number of requirements. These include but are not limited to: high analyte sensitivity (due to the very low concentrations at which these compounds cause harm), short response times, an ability to withstand a variety of environmental conditions, a low false alarm rate and a simple user interface. An ideal technique for detecting CWAs would have the capacity to identify a broad range of

target materials. In short, detection of CWAs is an extremely complex challenge spanning the fields of chemistry, physics, engineering and biology.

1.4.2. CURRENT TECHNIQUES FOR DETECTING CWAS

The multi-phase nature of CWAs requires specialised detection techniques. For example, the detection of vapours can be performed using mass spectrometry and ion mobility spectrometry (IMS), whereas the detection of liquids and solids is done with a combination of spectroscopy, mass spectrometry, IMS and detector paper for liquid samples. The detection of aerosol is possible using Fourier Transform IR spectroscopy and will be discussed further at the end of this section. Each of these techniques for detection and identification will be discussed individually.

There are many off the shelf handheld detection devices,[7] an example of a device used to detect vapour phase CWA is the Smiths Detection LCD 3.3 handheld detection instrument.[8] This device utilises non-radioactive IMS to detect the presence of vapour phase CWA, and to scan for residual CWA once a threat has been established. IMS is a relatively simple technique with very few moving parts which can detect very low concentrations of chemicals. It is possible to detect many compounds at concentrations between parts per billion to parts per million.[9] However, IMS based techniques can have high false alarm rates due to the non-discriminatory nature of the process of ionisation, meaning that compounds of little relevance can obscure the signal.[9,10] Additionally, IMS is quite sensitive to temperature and humidity variation. As temperature changes, the mobility of ions is affected which can cause a peak position to shift, which may prevent the identification of a target compound. At high humidities, ionised compounds may condense to form droplets of solution which will change the detected position of the peak.[9,10]

A well-established on-line technique for detecting CWAs in the liquid phase is detector paper. Detector paper has a fast response and can classify an agent as a member of a group of agents such as the nerve agents (V or G classes) or blister agents. Detector paper is usually comprised of two dyes and a pH indicator, when a potential CWA comes into contact with the detector paper the colour will change. For example, VX dissolves yellow dyes, and turns the pH indicator blue, the combination of these colour changes produces a green to black change in colour. Other detector paper types can distinguish between classes of CWA such as M8 and M9 detection paper. [7,11,12] Detector papers are low cost and easy to operate. However, they are not very precise and can result in false positives from

contamination with chemicals which occur in society (insect repellents, brake fluid, antifreeze etc). [13]

There are many different types of chemical sensors for detecting the presence of a CWA. Some rely on the formation of coloured transition metal complexes[14–17] others rely on fluorescence[18,19] or phosphorescence[20] to detect CWAs. A noteworthy technique by Pavlov *et al.* employs gold nanoparticles which change colour in solution as the nanoparticle size varies, the change in size of the gold nanoparticles is catalysed by the degradation of the acetylcholinesterase enzyme (AChE).[21] On-line CWA identification by sensors tends to be compound specific and rely on the individual chemical properties of each CWA. However, it is possible to detect a broad range of CWAs using spectroscopic techniques.

Many spectroscopic techniques for detecting liquid and solid CWAs are expensive, difficult to transport and are largely off-line. Analytical techniques such as gas chromatography, mass spectrometry, Infra-Red (IR), Raman spectroscopy and (multinuclear) nuclear magnetic resonance (NMR) spectroscopy, can be used for detecting CWAs. These spectroscopic techniques are rapid in their detection of a target agent, but some of them are not able to explicitly identify a CWA. An unequivocal identification of a CWA is done using liquid chromatography mass spectrometry (LC-MS) and nuclear magnetic resonance spectrometry (NMR). Laboratory grade spectrographs and spectrometers are complex instruments which are expensive and are often non-portable. However, with recent advancements in these spectroscopic technologies, smaller, more portable and less expensive spectrographs[22–24] and detectors[25–27] are becoming commercially available with implications for online detection.

IR spectroscopy is frequently applied to the CWA detection problem, particularly due to the strong phosphoryl stretch and other common stretching frequencies specific to many of the target agents. There are few available techniques for the detection of aerosol phase CWAs, of particular note, is the development of a Fourier transform infra-red (FTIR) spectroscopic technique for detection of deposited thin-film liquids and gas phase CWAs which measures the light scattering and absorption of compounds deposited on a surface up to 5-10 meters from the detector.[28] This is achieved using a femtosecond optical parametric oscillator light source, which generates an averaged power of 1 mW over a spectral bandwidth of 1000 cm^{-1}. The scattered light is then collected by a lens and an FTIR

detector generates a transmission spectrum, in which certain spectral ranges coincide with specific unilateral mode excitations depending on the chemical environment of absorption.

1.5. A New Analytical Tool for Flexible, On-line Sampling and Detection of CWAs

This thesis presents an approach to the detection of gas or aerosol phase CWAs by passing them over an optically tweezed probe droplet to identify their composition. The flow of aerosol and gas phase CWA is referred to as the ensemble flow. Through minute changes to the probe droplet radius, refractive index (RI) and spontaneous Raman band intensity it is possible to identify the presence of specific compounds in the ensemble flow.[29] Figure 2.3 shows a cartoon of a droplet confined in an optical trap, exposed to both aerosol and gaseous samples. The recorded Raman intensity ratio, radius and RI are increasing as more sample is accreted into the droplet. Aerosolised sample is shown to undergo discrete coalescence events with the probe droplet. Gaseous samples are shown to undergo gas-to-particle conversion whereby the gas condenses onto the probe droplet.

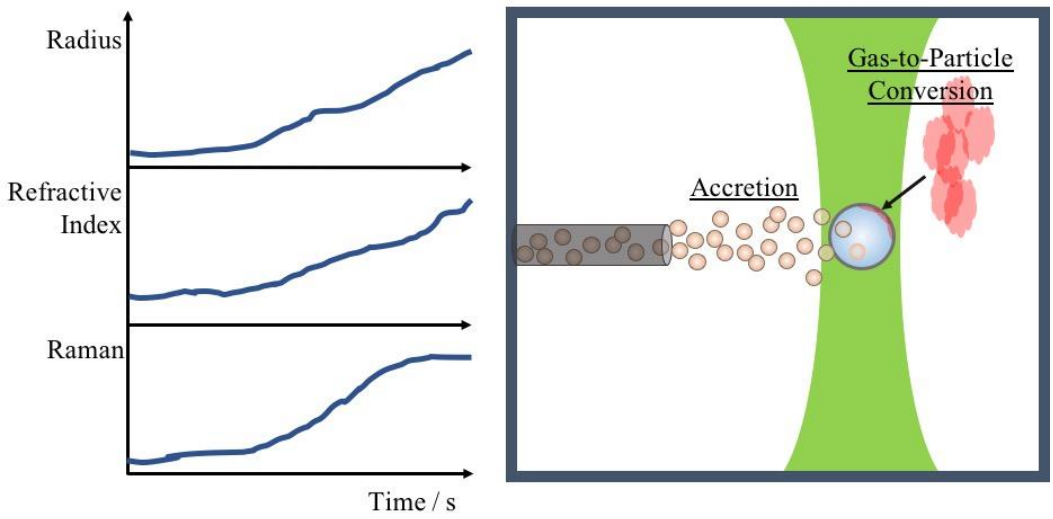

Figure 2.3: Seen on the right-hand side is a representation of a droplet held in an optical trap, exposed to a sample through both accretion and gas-to-particle conversion. On the left hand side, a representation of the droplet radius, RI and Raman intensity ratio changing over time.

As matter is condensed or coalesced into the probe droplet, the radius will increase over time. The RI measured will deviate from the RI of the probe droplet towards the RI of the accreting substance. The radius and RI are retrieved from the Raman spectrum, which can be collected at a rate of 0.05 – 100 frames per second. As the droplet composition changes the Raman intensity of the spontaneous bands changes over time, the Raman intensity ratio shows changes to droplet composition over time. The evolution of specific peaks, such as

the sharp nitrate or phosphate bands, can indicate the presence of CWAs. The changes to probe droplet radius, RI and Raman intensity ratio can be used to detect the accretion, or gas-to-particle conversion of targeted substances.

This technique can be easily tailored to detect specific agents, by selecting specific probe droplet compositions. Additionally, it is possible to scan for a broad range of CWAs by loading a series of different probe droplets sequentially. Sequential loading of the trap would utilise different solutions of droplets for detecting agents with different solubility and Raman signatures (for example a strong nitrate peak).

To detect CWAs using the AOT technique it is imperative to assess the baseline sensitivity. Further, there are many physical aspects of AOT which must be optimized for detection of CWAs, specifically, noise in the Raman signature, the probe droplet size and orientation of delivery of the ensemble flow. This project seeks to determine the optimum conditions to enhance the rate of accretion of CWA into the probe droplet.

1.6. METHODS FOR ESTABLISHING A PICOLITRE SAMPLER: SINGLE PARTICLE TRAPS

Aerosols are never isolated within the atmosphere, they exist as an ensemble of particles in a variety of sizes, phases, shapes, mixing states and compositions. There are many techniques which measure the optical properties of an aerosol ensemble. These measurements are subject to assumptions made when appropriating single particle scattering theory to predict the optical properties of a group of aerosol particles.[30] When the number density and diameter of the particles is lower in value, several assumptions are made. The particles are thought of as widely spaced. The light scattered by the surrounding particles is negligible when compared to the scattering of the incident field. Any separation of individual particles is regarded as random and a systematic phase relationship of radiation scattered by many particles does not exist.

Ensemble measurement techniques approximate the light scattered by an individual particle, results are merely a measure of the total scattering of light. Consequently, the retrieved parameters are the mean values of the constituent particles, and so measurements

of size, shape and refractive index are the mean of the ensemble. Single particle techniques do not require averaging to retrieve information about the particle.

Single particle measurement techniques facilitate precise studies of particle properties. Such techniques include electrostatic traps, fibre acoustic traps and optical traps. Each of these isolation techniques will be discussed in the sections below.

In this thesis, an ensemble of aerosol is measured by changes to an optically trapped single particle, which acts as a miniature sampling volume. Changes to properties such as composition, size and RI of the sampling aerosol can be attributed to the coalesced ensemble of aerosol. Therefore, this technique is a unique combination of ensemble and single particle optical aerosol techniques.

1.6.1. ELECTRODYNAMIC BALANCE (EDB)

One of the most widely known techniques, the electrodynamic balance, can be used to trap particles with sizes of 5 – 100 μm.[31] A droplet is dispensed and charged as it passes through an induction electrode into a chamber which contains two electrodes. High voltage AC and DC signals are supplied to the electrodes. An electrostatic force is applied to the droplet, which levitates the droplet within the chamber. Coupling levitation with a light source facilitates the collection of elastically scattered light. Any light which is scattered by the droplet is collected and recorded as a function of scattering angle.

It is possible to fit the resulting phase function to Mie theory and retrieve the particle size and RI. The EDB technique has been utilised in the study of evaporation kinetics and hygroscopic responses of aerosols,[32–35] and oxidation reactions in the aerosol phase.[36] In 2013, Leisner *et al.* investigated contact freezing of aerosol resulting from coalescence with a dry particle in an electrodynamic balance.[37] However, the trap strength in an electrodynamic balance is much lower than in optical tweezers. It is very difficult to load additional material into a droplet levitated in an EDB.

1.6.2. ACOUSTIC TRAPPING

It is possible to employ a high frequency sound wave to trap particles of aerosol, a process which is referred to as acoustic trapping. A standing sound wave is created using an ultrasonic frequency generator, situated directly opposite to a reflector plate. This creates nodes and anti-nodes at which droplets may be confined.[38] The lowest size which can be

confined in an acoustic trap is ~ 100 μm, which is too large for the experiments performed in this thesis.

Using acoustic traps groups have measured the surface tension of liquid droplets[39,40] and the evaporation of water droplets.[41,42] Groups have also confined particles in acoustic traps and exposed them to an ensemble of particles to determine scavenging efficiencies.[43] However, a sound wave has a pressure component which could act to distort the sphericity of the droplet and compromise the applicability of experimental results to atmospheric conditions.

1.6.3. OPTICAL LEVITATION

The most well-known optical trapping technique is optical tweezing which is discussed in detail in Chapter 2. A different optical technique which has been utilised in aerosol science is optical levitation using a Bessel beam. A Bessel beam has a high energy core surrounded by a series of concentric rings, and it is formed when a Gaussian beam is passed through an axicon.[44,45] When a Bessel beam levitates an aerosol particle, the gradient force confines the particle in the transverse orientation, and the strong radiation pressure of the central core confines the particle in the longitudinal direction.[46]

Lu *et al.* used two Bessel beams, in a counter-propagating configuration to trap particles of dodecane and hexadecane, upon cooling the trap to -50 ° C to study the kinetics of freezing.[47] Carruthers *et al.* used two counter propagating Bessel beams to trap multiple aerosol particles in a chain configuration.[48] Bessel beam traps have been used to measure the vapour pressure of semi-volatile species,[49] droplet hygroscopicity[50,51]and droplet viscosity.[52] Bessel beams are unique because they can confine particles less than 5 μm in diameter, with reported trapping of droplets as small as 0.5 μm.[50,51] This makes Bessel beam traps capable of trapping the smallest particles of all the single particle aerosol techniques. Although studying aerosols between 0.5 – 5 μm is vital for environmental atmospheric research, for this application, droplets between 3 – 7 micrometres will be used. This size range is larger than for atmospherically relevant particles as they are easier to trap, and the larger sizes (~ 7 – 10 μm) are avoided as a large droplet reduces the sensitivity of the instrument for detection. This means that a Bessel beam optical trap is not applicable for the detection of CWAs.

A widely used technique of optical levitation is the optical tweezers. Optical tweezers is a robust technique used in a variety of fields. Specifically, in the field of aerosol science,

optical tweezers are used to study droplets between 1 – 10 μm in radius. In 2015, Tolbert *et al.* investigated the efflorescence of droplets which resulted from coalescence between free flowing dry particles and an aqueous droplet trapped in an optical tweezers.[53] Again, this is an interesting effect of the coalescence of a dry powder aerosol with a probe droplet.

1.6.4. THE AOT TECHNIQUE FOR DETECTION OF CWAS

The AOT technique presents a unique potential solution to the detection of chemical warfare agents. The specific advantages of such a technique are evident as measurements are reliant upon specific chemical signatures, making it a versatile detection process. The AOT technique has no phase state dependency as it has the capacity to detect target materials in both the gas and aerosol phase. The detection of gas phase CWA is through absorptive partitioning of a target material into a trapped droplet. The target material can be detected in various aerosolised forms (solid; non-spherical, dry powder, wet solution aerosol, glassy aerosol *etc*) giving the technique a high degree of flexibility. The AOT technique is not size specific as it can detect a wide range of aerosol sizes. Additionally, probe droplets can be customised for the detection of specific chemical signatures and multiple probe droplets could be analysed in a time period of 1- 10 minutes.

The AOT technique has the potential to become a valuable technique for sampling CWAs. The AOT technique is more appropriate for this application because it can trap particles which are smaller in size, 1-10 μm, rather than the 100 μm particles in acoustic levitation. Smaller probe droplet sizes are more sensitive to sampling CWAs, due to the enhanced sensitivity to a change in the optical and physical properties.[2] The AOT technique is ideal because it can be easily coupled with powerful analytical tools such as Raman spectroscopy, it may also be suitable for coupling with other spectroscopic techniques, such as IR spectroscopy at a later stage. The AOT technique is superior to an optical trapping EDB as it has a more robust trap. Although a wide range of particles can be trapped and probed using an EDB, it is very sensitive to loading additional material for accretion sampling.

The development of the AOT aerosol detection technique is an advancement in the detection of CWAs, but also has the potential for adaptation into fields such as detection and monitoring of environmental pollutants and hazardous explosive chemicals.

1.7. WORK ON THE AOT TECHNIQUE UNDERTAKEN BEFORE THIS THESIS

The work prior to this thesis was conducted by other senior members of the Reid group and was presented in four reports.

The first report compiled for DSTL presented a framework for determining the minimum concentration of 7 CWAs detectable by the AOT approach, and the accompanying Henry's law coefficients required to achieve detection for gas phase CWAs. Henry's law describes the amount of a given gas that is dissolved within a volume of a given solution which is held at a constant temperature, and that amount is directly proportional to the partial pressure of that gas in equilibrium with the liquid. The constant of proportionality, the Henrys law coefficient, is specific to the solvent, the solute and the temperature. Henry's law is shown in Equation 2.1 where K_H^{cp} is the Henry's law coefficient, c_{aq} is the molarity of the gas phase species and p is the partial pressure of the gas above the solution.

$$K_H^{cp} = \frac{c_{aq}}{p} \qquad \text{Equation 2.1}$$

The Henry's law coefficient determines the extent to which a gas phase CWA will partition into the probe droplet and is therefore important in this project for understanding whether the primary mechanism of accretion of a CWA is through gas to particle partitioning, or coalescence of the ensemble aerosol with the probe droplet. Gas to particle partitioning occurs when secondary organic carbons (SOC), with low volatility condense onto a particle.

The first report concluded that without the development of a correlational framework (correlating changes in radius and RI simultaneously) "*none of the CWAs are detectable in a trapped droplet for gas phase loadings of 1pptv."* However, these values were calculated with a range Henry's law coefficients taken from the literature. The Henry's law coefficients in the literature are retrieved using experimental and theoretical methods and can differ greatly.

The first report also identified the fundamental factors influencing detection of CWAs through changes to radius (probe droplet size), RI (mis-match between probe and CWA RI) and Raman intensity ratio (Raman scattering cross section). It concluded that detection of a target species is expected to exhibit higher sensitivity to changes in radius than to changes in RI and to changes in RI than to changes to the spontaneous Raman signal.

The second task report investigated the sensitivity of the AOT technique to the detection of aerosol phase CWA, with specific interest in the enhanced uptake of target material as a

result of hydrolysis chemistry occurring between the CWA and the aqueous probe droplet. Once again, the lack of specific data regarding the Henry's law constants and the hydrolysis rate constants encumbered this work. The second report calculated the number of coalescing particles required to make specific changes to the probe droplet radius and RI for 3 and 8 μm probe droplets for each CWA.

The third report included an experimental setup of an accretion measurement, shown with results in Figure 2.4. Also published in a paper in 2016, the 5.4 micrometre droplet (droplet composition of aqueous sucrose) was exposed first to an ensemble of atomized solution of aqueous sodium chloride, and second to an atomized solution of aqueous sucrose.[54] It is possible to see, in the yellow sections, periods of accretion at ~2000 and ~4000 seconds respectively.

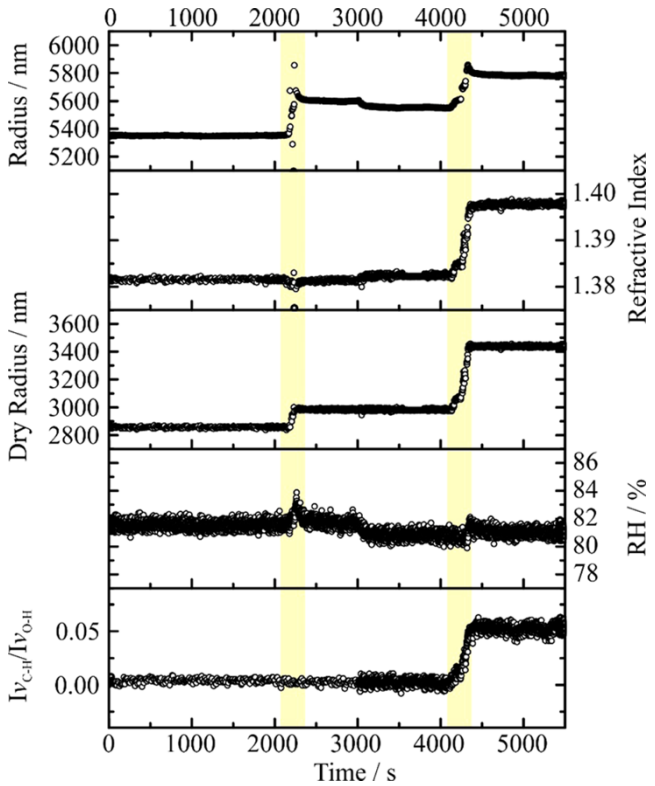

Figure 2.4: A figure showing five panels, in descending order, of the droplet radius, RI, Dry radius, RH and Raman intensity ratio over 5500 seconds. The yellow sections show two periods of accretion, the first is a period of accretion where an aqueous sodium chloride solution is atomized, into the aqueous sodium chloride droplet. The second yellow section shows a period of accretion of aqueous sucrose aerosol. Taken from Haddrell *et al.*[54]

The second and third reports determined a framework for predicting the sampling flux of accumulation mode aerosol by a probe droplet, predicting a collection efficiency of 5×10^{-5} %. The third report also conducted accretion measurements with a collection efficiency of 5×10^{-4} %. The collection efficiency can be defined as the percentage of aerosol which

was accreted into the probe droplet in relation to the total volume of aerosol passed through the cell. The order of magnitude improvement in the collection efficiency was hypothesized as being due to the enhancements caused by strong optical forces directing the ensemble flow towards the probe droplet. The experimental and theoretical accretion rates, or accretion flux were between 0.8 – 1.2 pg / min. The accretion flux was defined in task two by Equation 2.2 where Δm_{sample} denotes the mass of aerosol which has been sampled by, or coalesced into, the droplet every second, C is a correction factor for enhancements in collection efficiency, f is the fractional area of aerosol flow which was obstructed by the sampling droplet and Δm denotes the mass of aerosol transported into the cell.

$$\Delta m_{sample} = C \times f \times \Delta m \qquad \text{Equation 2.2}$$

The second task report also included a rigorous assessment of the accretion rate dependence on aerosol size distribution. The accretion rate was defined in Equation 2.3 in which N(t) denotes the time dependence of the number concentration, N_0 denotes the starting concentration of aerosol, t denotes the time and K is the coalescence rate constant, K is sometimes referred to as the coalescence kernel.

$$N(t) = \frac{N_0}{1 + N_0 K t} \qquad \text{Equation 2.3}$$

In this report the relationship between number and mass concentrations, and the representation of number and mass concentrations in log-space was addressed. The instruments used in this work measures absolute concentrations of aerosol, N_i, in bin sizes that select or sample aerosol over a discrete breadth in size. The aerosol distribution, n_i, for

a size interval, *i*, can be written as the ratio of absolute aerosol concentration, N_i, for this interval to the size range covered by the size bin ΔD_p. This is shown in Equation 2.4.

$$N_i = n_i \Delta D_p \quad \text{Equation 2.4}$$

The size distribution function $n_N(D_p)$ can be defined in such a way that $n_N(D_p)dD_p$ is equal to the number of particles per cm^3, when the particles have diameters in the range D_p to $D_p + \Delta D_p$, and $n_N D_p$ has units of $\mu m^{-1}\ cm^{-3}$ (Equation 2.5).

$$n_N(D_p) = \frac{dN}{dD_p} \quad \text{Equation 2.5}$$

The total number of particles within a unit volume is shown by N in Equation 2.6 where N has units of units of cm^{-3}.

$$N = \int_0^\infty n_N(D_p) dD_p \quad \text{Equation 2.6}$$

The aerosol volume distribution $n_V(D_p)$ can be defined in such a way that $n_V(D_p)dD_p$ is equal to the volume of particles per cubic centimetre of air. Where the particles have diameters between D_p and $D_p + \Delta D_p$, where $n_V D_p$ has units of $\mu m^{-2}\ cm^{-3}$ (Equation 2.7). The total aerosol volume, V has units of $\mu m^3\ cm^{-3}$, and is shown in Equation 2.8.

$$n_V(D_p) = \frac{\pi}{6} D_p^3 n_N(D_p) \quad \text{Equation 2.7}$$

$$V = \int_0^\infty n_V(D_p) dD_p = \int_0^\infty \frac{\pi}{6} D_p^3 n_N(D_p) dD_p \quad \text{Equation 2.8}$$

Similarly, the surface area distribution, $n_S(D_p)$ can defined in such a way that $n_S(D_p)dD_p$ is equal to the surface area of the particles and has units of particles per cm^3. Where the particles have diameters in the range of D_p to $D_p + \Delta D_p$. The surface area distribution function and total aerosol volume, S, are shown in Equation 2.9 Equation 2.10.

$$n_S(D_p) = \frac{\pi}{6} D_p^3 n_N(D_p) \quad \text{Equation 2.9}$$

$$S = \int_0^\infty n_S(D_p) dD_p = \int_0^\infty \frac{\pi}{6} D_p^3 n_N(D_p) dD_p \quad \text{Equation 2.10}$$

If it is assumed that the density of all of the particles is uniform, then the mass distribution function $n_M(D_p)$, is defined by Equation 2.11 and has units of $\mu g\ \mu m^{-1}\ cm^{-3}$. In Equation 2.11, ρ_p denotes particle density, and the factor of 10^6 changes the units of particle density

from the conventional g cm^{-3} to μg cm^{-3}. The total mass of particles within a unit volume, M, is derived in Equation 2.12.

$$n_M(D_p) = \frac{\rho_p}{10^6} n_V(D_p) \qquad \text{Equation 2.11}$$

$$M = \int_0^\infty n_M(D_p) dD_p = \int_0^\infty \frac{\rho_p}{10^6} \frac{\pi}{6} D_p^3 n_N(D_p) dD_p \qquad \text{Equation 2.12}$$

The number distribution is commonly shown on a scale of log(D_p, Diameter), accounting for the fact that the diameter of particles in the distribution can span orders of magnitude.

The size distribution function n_N^e (ln D_p), shown in Equation 2.13, has units of cm^{-3} and can be expressed in natural log form by the natural log-normal distribution.[55]

$$n_N^e(lnD_p) = \frac{dN}{d\ ln\ D_p} = \frac{N}{(2\pi)^{\frac{1}{2}}\ ln\ \sigma_g}\ exp\left(-\frac{\left(lnD_p - ln\bar{D}_g\right)^2}{2\ln^2\sigma_g}\right) \qquad \text{Equation 2.13}$$

Where N is the total aerosol number concentration (m^{-3}), $\bar{D}_g$ is the mean particle diameter and σ_g is the geometric standard deviation. In addition, in Equation 2.14 the size distribution function $n_N D_p$ ($\mu m^{-1}\ cm^{-3}$) is often used instead of n_N^e (ln D_p).[55]

$$n_N(D_p) = \frac{dN}{dD_p} = \frac{N}{(2\pi)^{\frac{1}{2}}\ ln\ \sigma_g}\ exp\left(-\frac{\left(lnD_p - ln\bar{D}_g\right)^2}{2\ln^2\sigma_g}\right) \qquad \text{Equation 2.14}$$

Figure 2.5 shows the size distribution function from Equation 1.11. The geometric standard deviation, σ_g, is a diameter, below this value 84.1% of particles lie towards the median diameter.

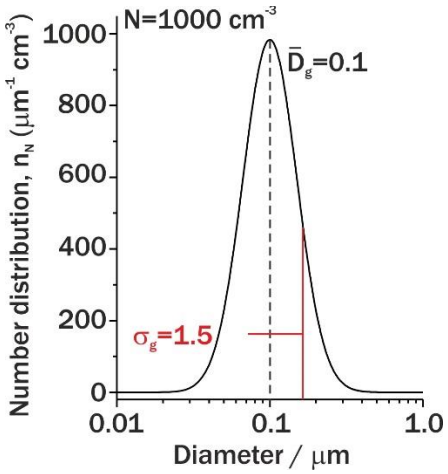

Figure 2.5: An example of the size distribution function $n_N(D_p)$, on a logarithmic scale. This is the shape of a log-normal number distribution of aerosol particles. Taken from DSTL report July 2015.[56]

A distribution function is most frequently represented in log-based 10 space by n_N^0(logD_p),[55] where:

$$n_N^0(logD_p) = 2.303 D_p n_N(D_p) \qquad \text{Equation 2.15}$$

and

$$n_N^0(logD_p) = \frac{dN}{dlogD_p} = \frac{N}{(2\pi)^{\frac{1}{2}}\, log\ \sigma_g}\ exp\left(-\frac{\left(logD_p - log\bar{D}_g\right)^2}{2\log^2 \sigma_g}\right)$$

Equation 2.16

For all distributions, the integral under the distribution is equal to the total number of particles in the aerosol sample with similar integrals to Equation 2.8. Aerosol ensembles tend to have distributions similar to those shown in **Figure 2.6**. A logarithmic distribution is employed due to the wide range of an aerosol size distribution, often greater than 10. In panel (a), with a logarithmic axis, the number distribution is log-normally spaced, however, in panel (b), on a linear axis, the number distribution is asymmetric towards the larger particle sizes.

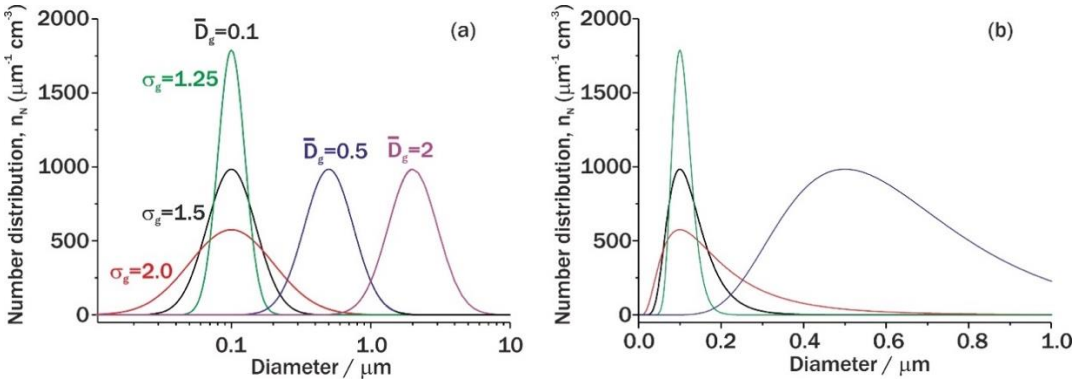

Figure 2.6: Panel (a) Shows the dependence of particle number distribution on breadth and median diameter. Panel (b) Shows the same particle number distributions as in (a) but presented on a linear scale. Taken from DSTL report July 2015.[56]

As particles of different size ranges are often produced from different sources, it is possible to represent the total aerosol as isolated distributions for the nucleation, accumulation and coarse modes. This can be seen in **Figure 2.7**, and is written as a sum of the distribution

functions in Equation 2.17, in which j represents a summation over the different isolated distributions for each aerosol size mode.

$$n_N^0(logD) = \sum_j \frac{N_j}{\left(\frac{2}{\pi}\right)^{\frac{1}{2}} log\sigma_{g,j}} \exp\left(-\frac{\left(logD - log\bar{D}_{g,j}\right)^2}{2\, log^2\, \sigma_{g,j}}\right) \qquad \text{Equation 2.17}$$

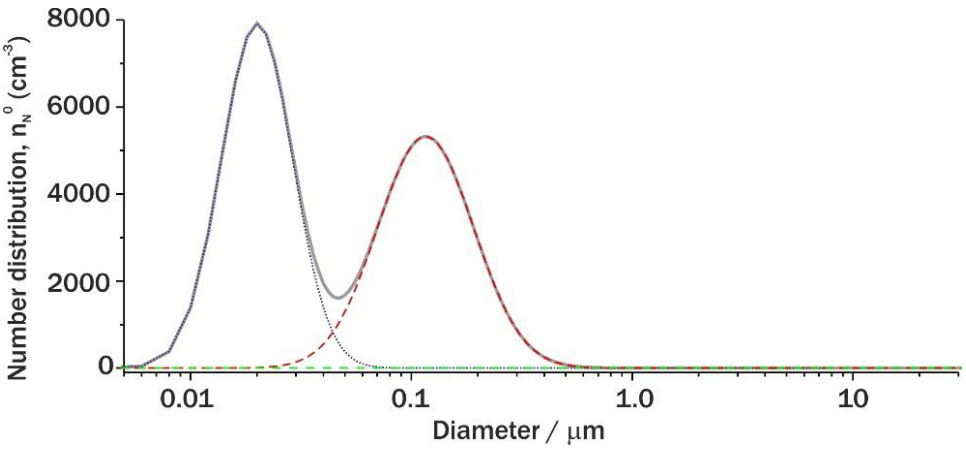

Figure 2.7: A sample summation (grey) of three isolated number distributions for nucleation, accumulation and coarse mode aerosol ensembles in blue, red and green respectively. Taken from DSTL report July 2015.[56]

It is important to tailor the selection of aerosol size distribution. Choosing one of surface area, volume and number concentrations is important and depends on what property is under investigation. Each of these properties can be applicable to a measurement depending on the size distribution of aerosol. The aerosol number distribution is frequently made primarily of nucleation mode particles. The surface area distribution is often dominated by accumulation mode particles. The volume distribution is often primarily made up of coarse

mode particles, despite often exhibiting the lowest number concentration. Each of these size distributions are displayed in **Figure 2.8**.

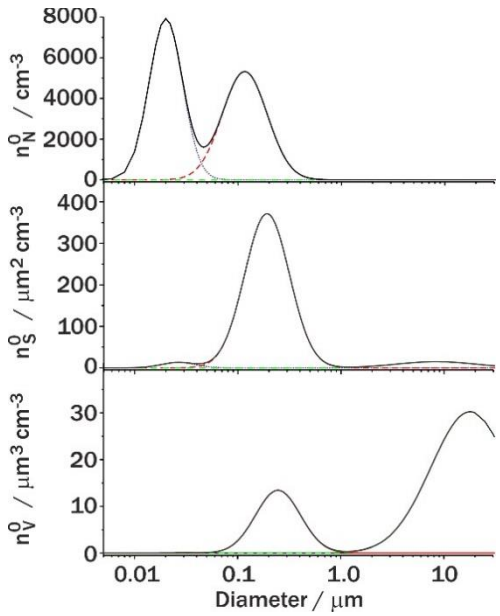

Figure 2.8: Three graphs, in descending order, of the typical number, size and volume size distributions. Taken from DSTL July 2015.[56]

Further, the integrals under the volume and surface area distributions can be expressed in terms of $n_N^0(\log D_p)$ and can be defined similarly to Equation 2.8 and then can be used to calculate the cumulative mass distribution.

$$V = \int_0^\infty n_V^0(logD_p)d\ logD_p = \int_0^\infty 2.303\ D_p n_V(D_p)d\ logD_p \qquad \text{Equation 2.18}$$

$$S = \int_0^\infty n_S^0(logD_p)d\ logD_p = \int_0^\infty 2.303\ D_p n_S(D_p)d\ logD_p$$

From

$$n_V^0(logD_p) = 2.303 D_p n_V(D_p) \qquad \text{Equation 2.19}$$

$$n_S^0(logD_p) = 2.303 D_p n_S(D_p)$$

Then

$$M = \int_0^\infty n_M^0(logD_p)d\ logD_p \qquad \text{Equation 2.20}$$

$$M = \int_0^\infty 2.303 \frac{\rho_p}{10^6}\frac{\pi}{6} D_p^3 \times D_p \times n_N(D_p)d\ log\ D_p \qquad \text{Equation 2.21}$$

A graph of the cumulative mass and number size distributions is shown in **Figure 2.9** with the data from Figure 2.5. At higher sizes the cumulative mass concentration increases, this is a consequence of the higher contribution to aerosol mass provided by particles in the coarse mode.

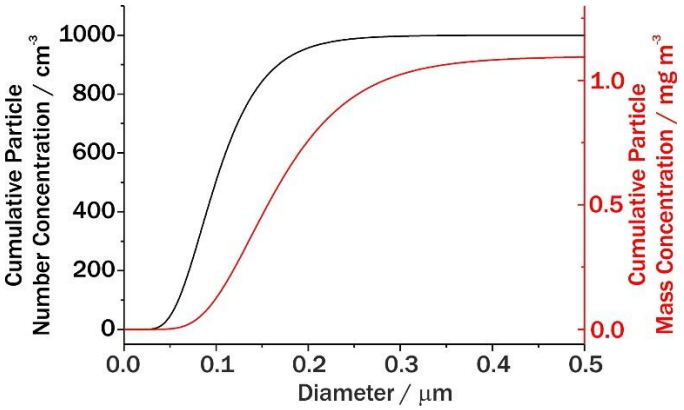

Figure 2.9: A graph showing the cumulative particle number concentration, black line, and the cumulative mass distribution, red line, for the distribution shown in Figure 2.5. The total mass concentration is 1.09 mg m^{-3} and the total number of particles is 1000. Taken from DSTL report July 2015.[56]

The fourth task report worked to refine the accretion experiment, adding a condensation particle counter, differential mobility analyser and a series of saturators and nafion driers. The experimental setup enabled preliminary experiments and led to conclude that the accretion measurement is dependent on the level of dilution when the aerosol size distribution peaks at ~100 nm.

1.8. THESIS OBJECTIVES

The following chapter seeks to assess the sensitivity of the AOT technique to the radius, RI and spontaneous Raman signature. A sensitivity assessment is performed to determine optimal probe droplet size and sample integration time in order to maximise the sensitivity of the technique. Chapter three discusses the experimental process in detail and looks at elements of the basic design with the intention of improving the technique for detection. Chapter four details measurements of accretion of sodium chloride and phosphate aerosol and details a series of accretion system designs for enhancing the accretion rate.

2. Building and Benchmarking: An Aerosol Optical Tweezers Instrument

In this chapter, the aerosol optical tweezers (AOT) technique is introduced and the building process described. This experimental method has been widely published in the literature.[57] A new trapping cell for confining aerosol was designed and tested to investigate the feasibility of introducing aerosol into an AOT along the axis of propagation of the trapping beam direction. A rigorous assessment of the trap stability was performed. The new system was benchmarked against a commercial system for comparison.

2.1. Introduction to Aerosol Optical Tweezers

Optical tweezing is the steady 3D optical confinement of a particle using a tightly focused Gaussian beam. The first successful optical tweezing of an aerosol particle was published by Magome *et al.* in 2003.[58] To successfully tweeze a particle, the gradient force has to be larger than the scattering force. This occurs when a tightly focussed beam, which has been formed using a high numerical aperture objective, passes through a particle, and when the refractive index (RI) of such a particle, n_p, is larger than the RI of the surrounding medium, n_m. A trapped particle is then levitated, confined in a positional equilibrium at the point of greatest light intensity within the beam. The restoring forces at the equilibrium position largely counteract external influences, for example, Brownian motion.[59]

In 2012, Miles *et al.* employed the AOT technique to retrieve the real component of RI with an uncertainty of ± 0.0012 and the droplet radius with an error of ± 0.05 %.[60] The AOT technique has also been employed in the measurement of hygroscopicity of salt droplets over a broad range of relative humidities (RH).[50] The advantages of an AOT lie in the stability of droplet position over long time scales and beneficial coupling with Raman spectroscopy to determine droplet radius. However, accurate measurements are only recorded using particles which have a radius greater than ~3 μm (coarse mode aerosol). It

is currently impossible to directly take measurements of fine or accumulation mode aerosol particles using AOT.

An AOT confines solid or liquid particles using light, and development of this technique has significantly advanced the field of aerosol science.[61] AOT can assist observations of physical processes, such as evaporation or condensation of matter into or out of a trapped aerosol droplet and microphysical properties such as the droplet viscosity or density, or to investigate dynamics and phase behaviour on a molecular to sub-micrometre scale.[2,62,63] The AOT technique is advantageous as highly accurate measurements of a single particle can be extrapolated to simulate atmospheric conditions for an aerosol ensemble. An example of AOT measurements is the retrieval of the RI of a binary solution salt droplet. The RI is an important input parameter for global climate models as it describes the interaction of cloud droplets with solar radiation.[64] AOT have been used in physical chemistry to determine the surface tension and viscosity from the droplet shape oscillations which are produced from a coalescence event.[65]

2.2. Optical Trapping Forces

The optical forces induced by light interacting with a particle can be used to levitate or even manipulate the particle. The technique of optical levitation was first examined by Ashkin *et al.* and optical levitation of an aerosol particle was first reported in 1970.[66] Ashkin utilized the radiation pressure of light, levitating dielectric particles which had diameters of nano and micrometres. The first optical tweezers experiment was published in 1987 in which a series of polymer beads were manipulated in solution with optical tweezers using infra-red laser beams.[67,68] For aerosols, the AOT technique is unique as it facilitates the isolation and independent manipulation of both the aerosol particle and the trapping environment.

The particle is suspended in the surrounding gas medium and, therefore, does not come into contact with chamber walls rendering the measurement of aerosol properties non-destructive to the particle. Because the particle is confined in space, optical trapping can be coupled with powerful spectroscopic techniques, such as Raman spectroscopy, which allows detailed studies into the fundamental properties of single aerosol particles. The coupling of optical tweezers with Raman spectroscopy introduces a significant advantage over other experimental techniques such as smog chambers, cascade impactors, or differential mobility analysers where compositional and physical analysis is often performed offline. Measurements of single aerosol particles are not routine within the field

but can be considerably more precise due to the absence of the errors incurred when averaging properties, such as size and composition, over an ensemble of aerosol particles.

There are two forces which are induced when a particle is exposed to a tightly focussed Gausian beam in the vertical orientation: the scattering force and the gradient force.[59,69] The scattering force describes the momentum transferred from the incident light beam onto the particle. The light intensity, *I*, is directly proportional to the scattering force. Put differently, the scattering force can be thought of as the back reflection of photons from a particle, which results in particle momentum which moves the particle in the direction of beam propagation. The magnitude of the scattering force is related to the dipole induced in the particle, the degree of polarisation which occurs as a result of the electric field component of the light beam acting on the particle. The magnitude of the polarisation is the polarizability, α, of the particle. The scattering force, F_{sca}, is described by Equation 2.1 and Equation 2.2 in which α denotes polarizability of the particle, *r* denotes the particle

radius, I is the intensity of the beam, E is the electric field, n_m is the refractive index of the surrounding medium and n_p is the refractive index of the particle.[57]

$$F_{sca} = \alpha^2 E^2 \qquad \text{Equation 2.1}$$

$$F_{sca} = (n_m - n_p) r^6 I \qquad \text{Equation 2.2}$$

The scattering force is depicted in section (a) of Figure 2.1 the gradient force is depicted in sections (b) and (c).

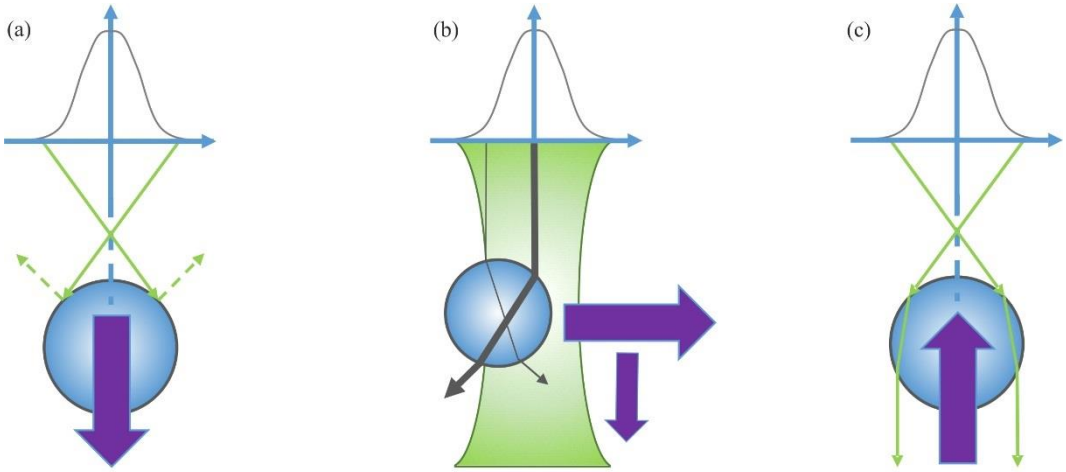

Figure 2.1: An illustration of the effect of scattering and gradient forces acting upon a trapped particle. The larger purple arrow represents the net direction in which the particle will move.

The gradient force is applied to the particle in three dimensions, this causes the particle to move into the position of greatest intensity of light. The particle is moved by the transfer of momentum of light through the particle. In section (b) of Figure 2.1, a particle is shown to be slightly displaced from the equilibrium position of the trap. The largest portion of light, shown by the thick grey arrow, travels through the right-hand side of the particle, it is then refracted out of the particle on the left-hand side. The particle has caused the transfer of momentum in the light beam from the right to the left side. The light, in turn, caused the particle to move from the left to the right. Through this process the particle has returned to the most position of greatest light intensity and is now in the equilibrium position discussed earlier. This is in accordance with Newton's laws, to every action there is a reaction, in this case, the conservation of momentum of the particle and light.

Within the trapped particle, the induced dipole is attracted to the varying field of light; therefore, the net force is continually drawing the particles into the point of greatest light

intensity within the beam. Equation 2.3 calculates the gradient force, F_{grad}, in which α denotes the polarizability of the particle and E^2 denotes the amplitude of the illuminating beam.

$$F_{grad} = \left(\frac{\alpha}{2}\right) \nabla E^2 \qquad \text{Equation 2.3}$$

In optical tweezers a highly focussed Gaussian beam, directed through a high numerical aperture (NA) objective, gives a large cone angle. This large cone angle, steeply varies the intensity, i.e. producing a large gradient in light intensity. In optical tweezers the gradient force is greater than the scattering force or gravity ensuring the particle is relatively stable in three dimensions.

2.3. PHYSICAL AND OPTICAL PROPERTIES OF AN AEROSOL

The experiment described in this thesis retrieves physical (radius) and optical (refractive index) properties of an aerosol particle. This section will discuss each of these properties within the context of optical trapping.

When a beam of light is directed towards a particle, the particle will affect the light through absorption or scattering. Scattering is a generic term which also describes refraction, diffraction and reflection of light (Figure 2.2). The electric component of the light beam excites the electrons of molecules within the particle. The energy of the excited electrons can be translated into other types of energy, primarily thermal energy, through absorption by the particle. This energy conversion process is dependent on the composition of the particle, the absorption characteristics of a droplet are complex. The excited energy can

also be reradiated and is emitted in all directions from the particle, this is known as scattering.

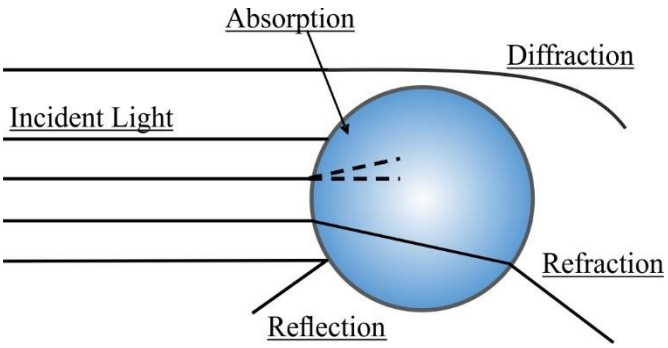

Figure 2.2: A diagram of the interactions between a small spherical particle and light.

Light scattering can be characterised by two terms, elastic and inelastic. Inelastic scattering occurs when the wavelength and energy of reradiated light is not equal to the energy of the incident light. Examples of inelastic scattering are fluorescence and Raman scattering. Light scattering is elastic if the reradiated light has same wavelength as the incident light. This project does not utilise elastic scattering.

2.3.1. PARTICLE SIZE

When the wavelength of the incident light beam is greater than the particle diameter (generally the particle diameter is $< \lambda/20$), the light scattered by the particle is best described by the Rayleigh approximations to Mie theory. When light is scattered by these particles, the phase of both the scattered and incident light is unchanged. In cases where the wavelength of the incident light beam is equal to or less than the diameter of the particle, the scattered light is best described by Mie theory. Particles of this size do change the phase of the scattered light, and this produces interference patterns which can be seen in the

photograph in Figure 2.3. For particles that are significantly greater than the wavelength of illuminating light, an approximation to ray geometrics can be used.

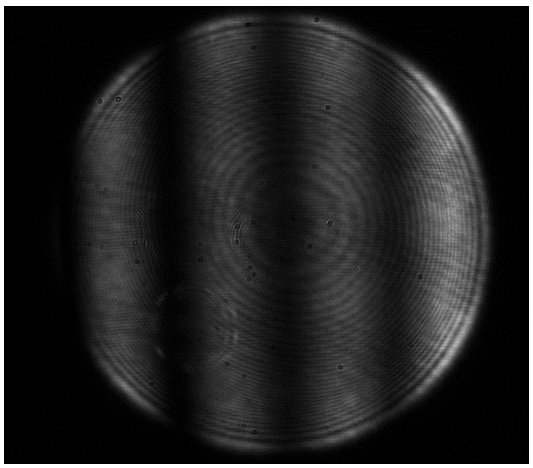

Figure 2.3: An image of a phase function of a droplet with the light 'fringes' on the droplet representing a higher intensity of light.

The droplets discussed in this project are within the Mie regime. Mie theory was developed in 1908 by Gustav Mie, it describes the scattering of electromagnetic radiation by a homogeneous sphere. The Lorenz-Mie solutions to Maxwell's equations are used in this thesis to fit the radius, RI and dispersion in RI of a trapped aerosol particle. This fitting process assumes that the trapped particle is completely homogeneous and spherical and will be discussed in more detail in section 2.5.2.

2.3.2. REFRACTIVE INDEX

The optical properties of an aerosol particle are defined by its refractive index. The refractive index, N, is a complex number in which the real component, n, resolves the extent and amplitude of scattering and the imaginary component, ik, resolves the extent of absorption as shown by Equation 2.4. This thesis assumes the absorption component of the compounds studied (sodium chloride, sodium phosphate, sucrose) to be negligible and therefore only the real part of the refractive index must be known.

$$N = n + ik \qquad \text{Equation 2.4}$$

There are two processes which occur when particle acts on a beam of light and they are determined by the RI. The first process is demonstrated by considering an incident light beam crossing a boundary layer, or interface, of RI between the particle and the surrounding

medium. Upon crossing the interface, a change in beam propagation is observed. In Figure 2.4 the RI of the surrounding medium, n_m, is less than the RI of the particle, n_p.

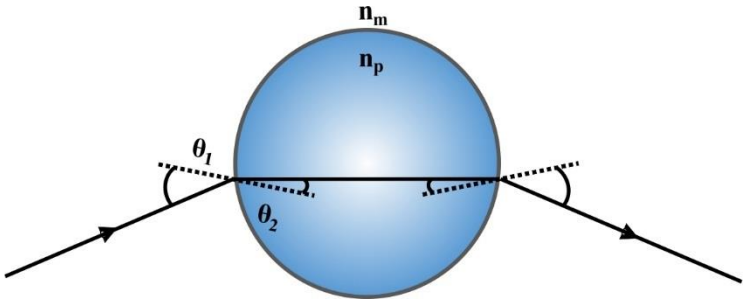

Figure 2.4: An illustration of light becoming refracted as it passes through a particle.

The relationship between these refractive indices at the phase boundaries is described by Equation 2.5.

$$n_1 sin\theta_1 = n_2 sin\theta_2 \qquad \text{Equation 2.5}$$

The RI of a particle acting upon a beam of light is also defined as the extent to which the speed of light is altered upon propagation through the particle. A beam of light travels more slowly through the particle medium than through air or vacuum. The difference between the speed of a light beam through a particle and the surrounding medium leads to phase differences between the light passing around and through the particle. The phase difference generated by light travelling through the particle is dependent upon the distance travelled by light passing through the particle relative to the distance light travels around the particle boundary.

2.3.3. LIGHT SCATTERING AND MIE THEORY

When a droplet is illuminated with plane wave, a proportion of light is elastically scattered and can be collected to infer properties of the particle. The size parameter, *x*, describes the relationship between the wavelength of incident light and the size of a particle and is

defined in Equation 2.6. The droplet size is denoted by r, the wavelength of incident light by λ, and N is the refractive index of the surrounding medium.

$$x = \frac{2\pi rN}{\lambda} \qquad \text{Equation 2.6}$$

When the particle radius is considerably smaller than the illuminating wavelength, it is said to be fall within the Rayleigh regime. The droplet can be thought of as a point dipole from which light scattering occurs without dependence on the particle radius. When the particle radius is larger than the wavelength of incident light it is described by an approximation to ray optics, a particle is treated as a lens and any dependence on the incident wavelength need not be considered. When the particle size is comparable to the wavelength of incident light the particle can be described by Mie theory.

Mie theory consists of a set of mathematical solutions to the Maxwell equations expressing the interaction of light with a spherical homogeneous particle. Both the internal and scattered field can be calculated. The angular scattering is referred to as the phase function. Mie theory can be applied to particles which have a diameter comparable to the wavelength of illuminating light. However, Mie theory assumes that a particle has a constant refractive index, is illuminated by a monochromatic plane wave and is completely spherical and homogeneous in composition.

Several groups have effectively employed the solutions to Mie theory to calculate the radius and RI of aerosol particles. Some examples are, Lu *et al.* who published the phase function of aerosol phase binary sucrose droplets exposed to decreasing RH between 75 % to 5 %. Lu *et al.* conducted this experiment to explore the equilibration dynamics of ultra-viscous glassy state aerosol.[70] Liu *et al.* used Mie Theory to predict the light absorption by fine particles of brown carbon aerosols in the atmosphere.[71] The scattering of light from a particle is a valuable phenomenon which can be recorded to probe the evolution of aerosol properties over time.

2.4. RAMAN SPECTROSCOPY

Coupling Raman spectroscopy with optical tweezers is a widely published approach which yields information regarding the composition, size and optical properties of an aerosol droplet. In the Mie regime the droplet radius is comparable to the wavelength of incident light and this can lead to the existence of cavity resonances formed of standing waves

within a spherical particle.[50,59] It therefore stands that the wavelengths of cavity enhanced Raman spectroscopy are dependent upon droplet RI and radius.

2.4.1. SPONTANEOUS RAMAN SPECTROSCOPY

When a molecule interacts with a photon it can become excited from the ground vibrational state into a virtual state of higher energy.[50] Upon relaxing back to the original vibrational sate, a photon is scattered. The energy of the photon determines the type of scattering which has occurred. Elastic scattering occurs when the emitted photon has an energy which is equal to that of the incident photon. However, in some cases the emitted photon has an energy which is not equal to that of the incident photon; this is known as inelastic, or Raman scattering. Raman scattering can be categorised by two different types of inelastic scattering, anti-Stokes and Stokes, due to differences in the energy of the photon released. Anti-Stokes scattering occurs when the emitted photon has a larger energy than the incident photon, rendering the wavelength of the relaxing photon shorter than the incident wavelength. Stokes scattering occurs when the emitted photon has a lower energy than the incident photon, the wavelength of the relaxing photon is longer than the incident

wavelength. The different types of scattering of light by a molecule are displayed in Figure 2.5.

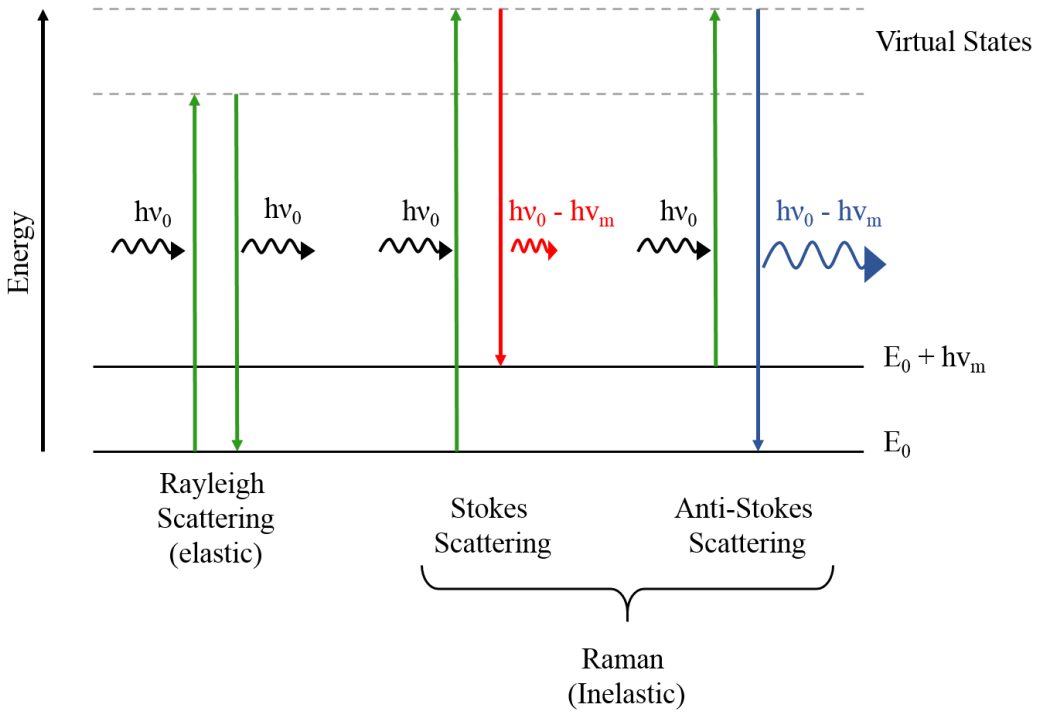

Figure 2.5: A schematic displaying the different types of scattering, elastic and inelastic. Within the inelastic scattering pattern is Stokes and anti-Stokes scattering.

Raman scattering is weaker than Rayleigh scattering: only 1 in 10^6 – 10^8 of the incident photons arise from an inelastic transition to the ground state or excited state.[72] A Raman transition is the direct result of a transition in the vibration energy of a bond. Although the prevalence of elastic scattering over Raman transitions renders Raman spectroscopy relatively inefficient, notch filters can be used to prevent the elastic scattering from saturating the spectrograph and obscuring the Raman signal.

The energy difference between the incident and emitted photon is described by the Raman shift. The chemical functionality of a molecule is shown in its specific Raman shift fingerprint. A molecule is Raman active if the electric field of the incident light can invoke an oscillating dipole within the molecule.[50] A table of the stimulated Raman peaks which are frequently examined in this thesis are shown in **Error! Reference source not found.**. The Raman wavelength of the peak can be converted into a Raman shift value of wavenumbers in cm^{-1}, Δw, by Equation 2.7 where λ_{ex} is the excitation wavelength, and λ

is the Raman wavelength in nanometres. In this thesis the excitation wavelength was 532 nm and the Raman wavelength was 650 nm.

$$\Delta w = \left(\frac{1}{\lambda_{ex}} - \frac{1}{\lambda}\right) \times 10^{-7} \qquad \text{Equation 2.7}$$

Table 2.1: A table of the Raman shift and Raman Wavelength values associated with bond stretches of compounds which are used throughout this thesis, [73] and four CWAs. The values for phosphate are the values for potassium dihydrogen phosphate and shown are the peaks for $P(OH)_2$ and PO_2 respectively.[74]

Bond Stretch	Raman Wavelength at 532 nm / nm	Raman Shift / cm^{-1}
O-H	637-665	3100-3650
C-H	626-634	2800-3025
Nitrate	562-565	723-1395
Phosphate	558, 564	877, 1077
C=O	578-589	1550-1820
C-O	563-572	1040-1300
VX	554	744
Sarin (P-C)	553	725
Tabun (C≡N)	602	2198
Sulphur Mustard (H-C-H Bend)	571	1296

A Raman spectrum of a droplet containing sucrose and water is shown in Figure 2.6.

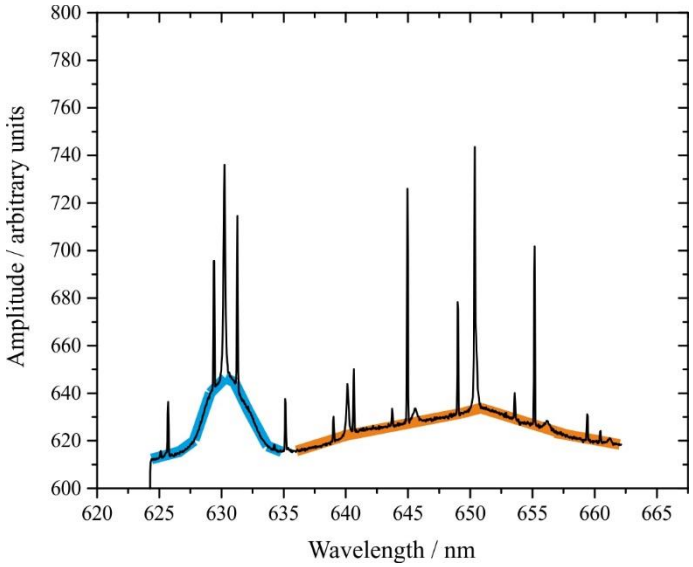

Figure 2.6: A figure showing the Raman spectra of a sucrose droplet over 40 seconds. The blue band represents the spontaneous band for the CH stretching frequency. The orange band represents the spontaneous band for the OH stretching frequency.

The spontaneous band in the lower wavelength region between 626 and 634 nm is the result of the C-H stretching frequency of sucrose. The spontaneous band in the higher wavelength

region between 637-665 nm can be attributed to the OH stretching vibrations of water. This is a particularly wide band because there are multiple hydrogen bonding environments within the droplet and water molecules which generates a series of force constants and Raman shifts. The force constant of the bonds, k, can be related to the frequency of oscillation,ν, in Equation 2.8 where c is the speed of light and μ is the reduced mass of the oscillating molecule. The relative ratio of the integral of each spontaneous band can be used to track the composition of an optically tweezed droplet over time.

$$\nu = \frac{1}{2\pi c}\sqrt{\frac{k}{\mu}} \qquad \text{Equation 2.8}$$

The Raman scatter generated from an optically tweezed aerosol droplet is primarily Stokes scatter due to the relatively low population of the ν = 1 vibrational level relative to the ν = 0 vibrational level, as determined by the Boltzmann distribution. Equation 2.9 defines the number of photons scattered per second, N_R (s^{-1}), over a solid angle, ΔΩ (sr), using the frequency, ν (s^{-1}), and intensity, I_0 (W cm^{-2}), of the incident light, the beam waist, S (cm^2), the number density of the scattering species, N (molecule cm^{-3}), the interaction length, z (cm), and the Raman scattering cross section (δσ/δΩ) (cm^2 $molecule^{-1}$ sr^{-1}).[50]

$$N_R = \left(\frac{\delta\sigma}{\delta\Omega}\right)(\Delta\Omega)\frac{I_0}{h\nu}NSz \qquad \text{Equation 2.9}$$

The Raman scattering cross section, (δσ/δΩ), describes the strength of spontaneous Raman scattering for a particular vibrational mode for a particular molecule. The Raman scattering cross section for a molecule determines the effective 'optical' radius of a molecule with regard to Raman scattering of light. With units of cm^2 $molecule^{-1}$ sr^{-1}, it is a parameter which has an inherent volume as the degree of scattering can only be measured over an angular range determined by a Steer Radian (sr^{-1}).

The Raman scattering cross section determines the compound specific lower limit of detection for Raman active molecules relative to the concentration. For example, the Raman scattering cross section for VX is 10.0×10^{-30} $cm^2mol^{-1}sr^{-1}$,[75] and the Raman scattering cross section for water is 4.0×10^{-30} $cm^2mol^{-1}sr^{-1}$.[76]VX has a higher Raman scattering cross section than water, therefore it has a lower detection limit.

The Raman scattering cross section is used in the calculation of the Raman Gain constant, G, of a stimulated Raman whispering gallery mode (WGM) (described in full in section 2.4.2) and is a wavelength dependent parameter. Raman gain is the resultant amplification from stimulated Raman scattering and is seen as the resonance peaks on top of the broad

spontaneous bands which are seen on the spectrum in Figure 2.6. The wavelengths of these stimulated Raman peaks can be used to calculate the size and refractive index of a droplet.

Table 2.2: A table of the Raman scattering cross section values for some of the molecules studied in this thesis and four CWAs for comparison.[77,75,78]

Molecule	**Pump Wavelength / nm**	**Cross-Section / cm^2 $molecule^{-1}$ sr^{-1}**
Water	532	4.0×10^{-30}
Sodium Nitrate	514.5	9.1×10^{-29}
Sodium Phosphate	532	8.1×10^{-30}
VX	532	10.0×10^{-30}
Sarin	532	6.0×10^{-30}
Tabun	532	7.6×10^{-30}
Sulphur Mustard	532	0.8×10^{-30}

2.4.2. STIMULATED RAMAN SPECTROSCOPY IN DROPLETS

When a spontaneous Raman photon is emitted, a droplet can act as a low loss optical cavity, with the light at the droplet / air interface reflected; creating a standing wave along the periphery of the droplet. This circulating Raman scattered intensity stimulates further scattering which amplifies the intensity of light at discrete wavelengths within the profile of a Raman band. It is only when a particle falls within the Mie regime that it can efficiently form a resonant cavity. This appears as a sharp peak superimposed on the spontaneous band at a whispering gallery mode (WGM) wavelength. This term was first introduced by Lord Rayleigh explaining the popular phenomenon of the whispering gallery in the dome of St Pauls Cathedral, where it is possible to hear a person on the opposite side of the dome

whispering due to an acoustic wave. Figure 2.7 is an example of the radial pathway of a WGM as it formed around the surface of a droplet.

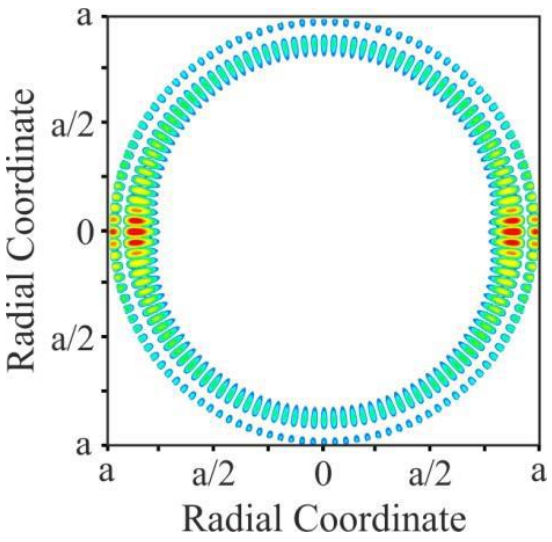

Figure 2.7: The Raman resonance building up through the cavity for a 4.5 μm droplet, specifically a second order mode, with a mode number of 60. Taken from Symes *et al.*[73]

The lifetime of a resonant mode within the optical cavity is determined by a mode quality factor, Q, the ratio of the frequency of the line centre of a mode over the width of the mode. The quality factor can be calculated using Equation 2.10.

$$Q=\frac{\gamma}{\Delta\gamma} \qquad \text{Equation 2.10}$$

The light intensity within the droplet builds up generating sufficient intensity to amplify the Raman scatter at wavelengths resonant with WGMs, leading to a process known as cavity enhanced Raman scattering (CERS). The larger the droplet, the larger the value of Q, the higher the intensity of the internal light field. For smaller droplets, the mode is broader than a WGM of a larger droplet.

Every WGM in a spectrum can be assigned a mode order, l, number, n and a polarisation (transverse electric, TE, or transverse magnetic, TM). The mode number designates the number of wavelengths that form the standing wave within a droplet. The mode order determines the number of maxima/minima of the standing wave in the radial direction. The higher the mode order, the greater volume of the particle the wave penetrates, meaning that

the extent of the light field penetrates deeper into the droplet. Figure 2.8 shows a Raman spectrum which has been fully assigned.

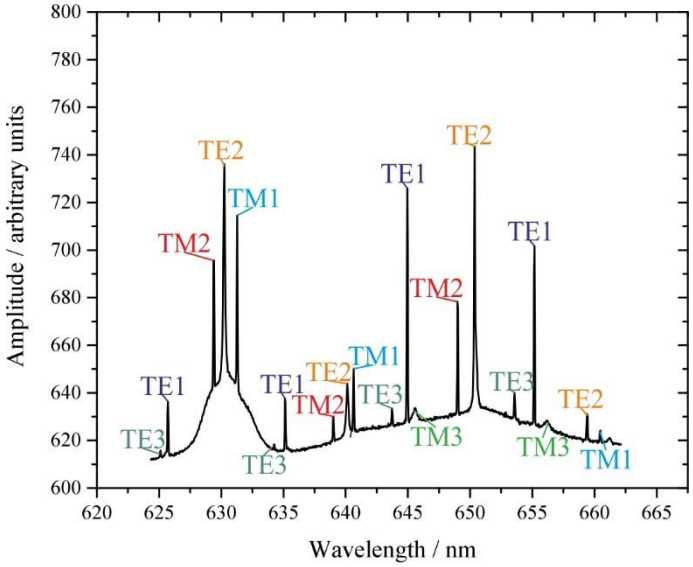

Figure 2.8: A Raman spectrum of an aqueous 4.95 μm sucrose droplet with a RI of 1.46 which has been averaged for 40 seconds. The whispering gallery modes have been assigned.

The quality factor of a WGM directly influences the line shape of the observed WGM. WGMs with a higher mode order are broader and weaker than those of a lower mode order. The quality factor for a single aerosol optical cavity mode has been recorded to range from 10^3 to 10^8 depending on droplet size, RI, mode number and order, which allows the recording of sub-nanometre Raman linewidths.[79] By comparing the experimentally obtained line centre of the WGM, with those predicted by Mie theory, it is possible to accurately estimate the size and RI of an optically tweezed particle.[60]

2.5. Designing and Constructing an Optical Trap

The work completed in Chapter 3 was performed using the commercial AOT-100 developed at the University of Bristol in conjunction with Biral. This system will be referred to as OT1.[80] A second research-based system, OT2, was constructed for the purposes of this project. This system was built to examine the most effective setup to

sample ambient aerosol using an AOT. The experimental setup of OT2 is shown in Figure 2.9. Each feature of the instrument will be discussed individually.

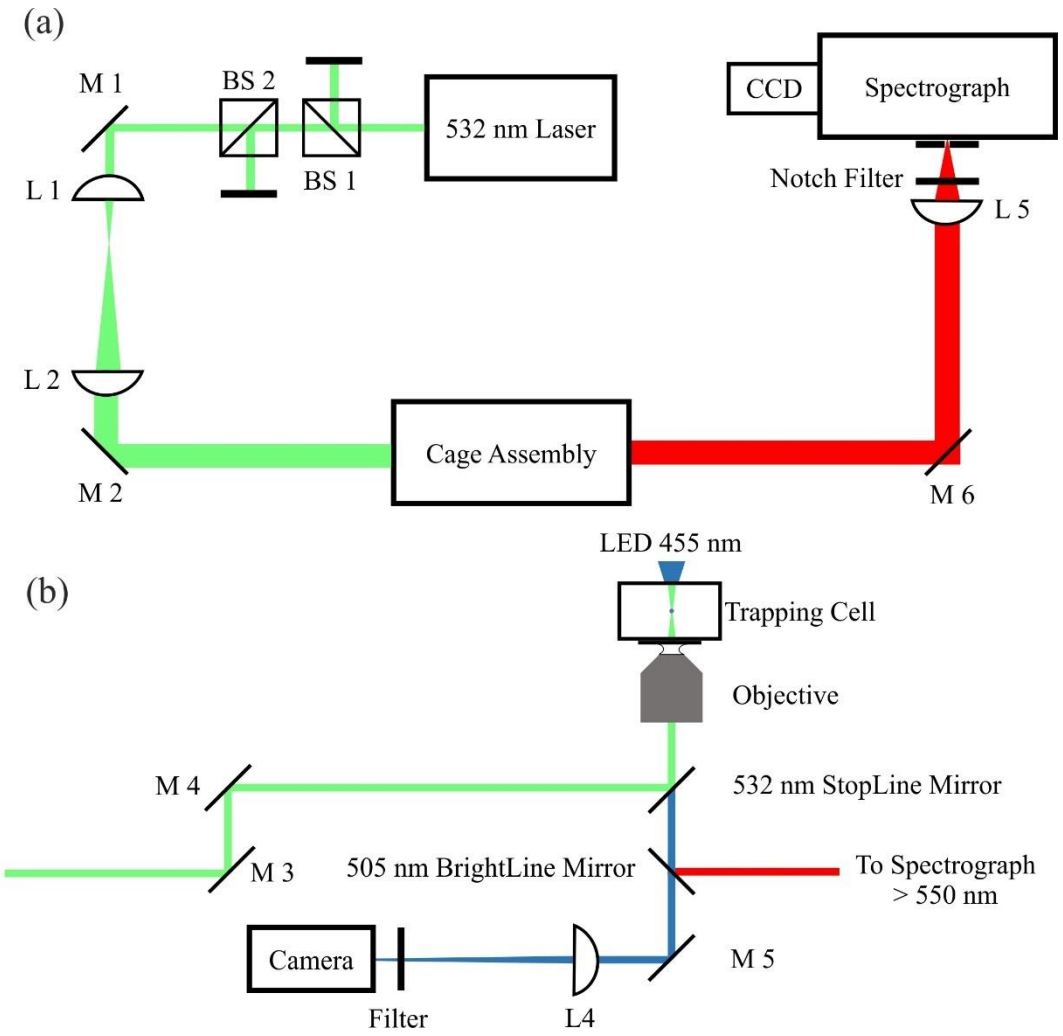

Figure 2.9: A diagram of the experimental setup of the AOT experiment of OT2. Panel (a) shows the experimental setup and panel (b) shows the cage assembly setup. Abbreviations: BS = beam splitter, M = mirror, L = lens, CCD= Charge coupled device.

Figure 2.9(a) displays the optical setup and beam pathway of OT2 from above. A Nd:YAG continuous laser (OPUS 2W, Laser quantum) generated a horizontally polarised beam, which had a diameter of 1.9 mm ± 0.2 mm. The 532 nm beam was passed through two beamsplitters to increase the operating light intensity of the laser beam, to allow it to be operated at a higher laser power while still directing a low (~ 60 mW) laser power to the objective. This will be discussed in more detail in section 2.7.1.

The diameter of the trapping beam was expanded to 4.2 mm by two lenses. The focal length of L1 was 10 cm and the focal length of L2 was 22 cm. This enabled the alignment of the trapping beam onto the back aperture of the microscope objective (~ 5 mm), which is

situated within the cage assembly. The alignment of the cage assembly is also depicted in Figure 2.9.

The microscope objective was inverted. The trapping beam was focussed and directed through an RI matched oil:glass interface. This interface was comprised of immersion oil and a glass coverslip (Chance Glass, microglass thickness No. 1). The resulting focal points fall inside an enclosed cavity, known as the trapping cell. The working distance of the objective was 1.8 mm, the magnification was 100 x and the numerical aperture was 1.25.

The brightfield light (shown in blue in Figure 2.9) and Raman scattered light (red) were also collected by the objective. A laser line mirror with an efficiency of 99.9% (StopLine notch dichroic beamsplitter for CARS, efficiency = 99.9%, Laser 2000 UK) selectively reflected elastically scattered 532 nm light, allowing the brightfield and Raman light to pass through the cage assembly. A Brightline single edge dichroic beamsplitter (Laser 2000) reflected all light above 505 nm towards the Raman spectrometer and transmits the brightfield light towards the camera. This was used to separate blue brightfield light and the Raman scattered light- which has wavelengths greater than 550 nm. More comprehensive descriptions of the Raman spectrograph and the camera are found in sections 2.5.1 and 2.5.4, respectively.

In order to trap a droplet, the chemical species to be probed was prepared in a bulk solution and nebulised by means of a medical grade nebuliser (OMRON, NE-U22-E). The aerosol size distribution generated by the nebuliser is between 1-5 μm with a mean diameter of 3.5 μm. The generator can aerosolize bulk solution at a rate of 1 mL/min. The aerosol plume generated by the nebuliser was directed through the inlet tubes into the trapping cell. A particle becomes confined if its trajectory passed sufficiently close to the optical trap that the gradient force drew it into the trap. The radius of the trapped particle can be increased to a specific size range by additional aerosolization during which coalescence events can occur between the trapped droplet and free flowing aerosol. However, this is a delicate process and often results in loss of the trapped particle from the trap. It is possible to trap particles up to 10 μm in radius. The largest particles studied in this work were up to 7.5 μm in radius.

2.5.1. RAMAN SPECTROGRAPH AND THE CHARGE COUPLED DEVICE (CCD)

The composition and size of an optically tweezed droplet can be determined using CERS. Probing the composition and size of a droplet is only possible when the WGMs are discernible from the background noise in the spectra. High numerical aperture (NA) is

essential to achieve a high collection efficiency and therefore a good signal to noise ratio. The inverted microscope objective, which focussed the 532 nm light to create the optical trap, serves the additional purpose of collecting and collimating the Raman signal.

The microscope objective collimated the backscattered light and a 50 mm lens focussed the light through the entrance aperture (0.4 mm wide) of the Raman spectrograph (PI-Acton, SP500i). A longpass filter was situated immediately before the spectrograph entrance to remove any light below 550 nm (specifically elastically scattered laser light), which would saturate the spectrograph with light causing damage to the CCD. The spectrograph used a diffraction grating to disperse the light by wavelength. The spectrograph has three diffraction gratings (300, 1200 and 2400 grooves / mm) and it was possible to change the diffraction grating during an experiment. The wavelengths of light become more spatially dispersed the greater the number of grooves per mm. A larger dispersion of wavelengths reduces the wavelength range recorded by the CCD but improves the spectral resolution.

In this project, most of the experiments were conducted using the 1200 grooves / mm grating, which facilitated a wavelength range of 625-665 nm with a resolution of 0.04 nm / pixel. This range was selected for the majority of the work as it easily covers the spontaneous OH and CH Raman bands. Some experiments were conducted using the 300 g / mm grating over different wavelength ranges. The wavelengths dispersed Raman light was then projected onto a CCD (Princeton Acton, PIXIS 256E, 1024 x 256 pixels). The CCD was cooled to – 70 °C to reduce noise from dark current. The CCD was set to record spectra at 1 frame per second (fps).

2.5.2. PROCESSING SPECTRA

The variation in light intensity with wavelength was relayed to the computer and analysed by a LabView program. The custom built Live Aerosol Raman Analysis (LARA) software was used to search for the wavelength at the line centre in the Gaussian peak of the WGMs for each frame. By comparing the experimental WGM positions to a library of the theoretical solutions to Mie theory within a set of defined parameters, it is possible to retrieve the radius, RI and dispersion in RI.[81] The retrieval of the radius is determined by the number of modes and the spacing between two modes of the same polarisation, but of different order (a TE1 and TE2 mode). If the RI of a trapped droplet changes but the radius remains constant, the relative positions of the TE and TM modes of the same order changes over time. By determining the position of each of the WGMs in relation to one another it

is possible to fit the radius and RI accurately, determining the retrieval of the real part of RI with an uncertainty of ± 0.0012.[82]

The accuracy in the positions of the experimental wavelength was ensured by regular calibration of the Raman spectrograph using a mercury / neon:argon calibration lamp (Princeton Instruments Intellical) with a reproducibility of ± 0.2 nm. Any error in the calibration of the Raman spectrograph would lead to a systematic error in the spectrum, with a constant shift in the reported wavelength and inaccuracy in size.

2.5.3. The Trapping Cell

Particles were confined within a steel trapping cell which served several functions, allowing precise control of the environment surrounding the trapped droplet (gas phase conditions, temperature) and limiting any disturbance to the droplet by ambient air currents. The cell was comprised of a deep base and shallow lid which could be secured in place. In between the steel lid and base was a Teflon insert which set the internal volume of the cell and reduced the build-up of electrostatic charge which could affect the trapping ability of an AOT instrument. The lid had a top window which was circular and positioned in the middle of the cell. In order to clearly illuminate the particle, an LED was positioned ~5 cm above this window which illuminated the trapped particle from above. At the bottom of the

steel base and Teflon insert, the microglass coverslip was mounted on a circular aperture of 10 mm diameter.

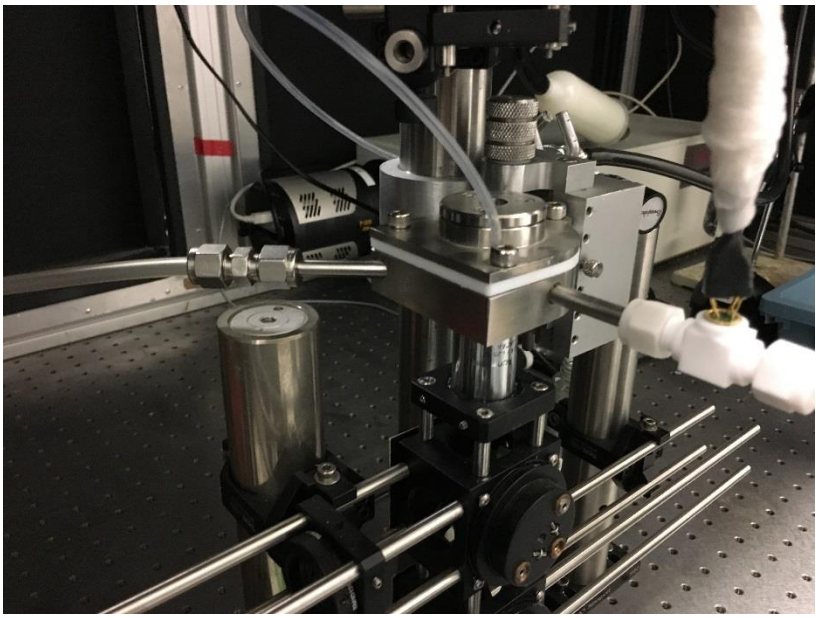

Figure 2.10: A photograph showing the trapping cell mounted above the objective. The ¼ inch tube entering the cell from the left-hand side is the radial gas flow inlet, the 1.8 inch tube coming from the top of the cell is the axial gas flow inlet and the tube on the right hand side of the cell is the exhaust, there is also a Honeywell RH probe placed on the exhaust line. The cell itself has three sections, a steel top, Teflon insert (white) and a steel base.

Several ¼ inch tubes can be seen connected to the cell in the radial orientation (in the horizontal plane) which are used to deliver aerosol and gas flows. At the rear is an exhaust. Further iterations of the cell design were explored during this project. A cell was custom

built to include a 1/8 inch inlet in the axial orientation, directed vertically from above the trapped droplet.

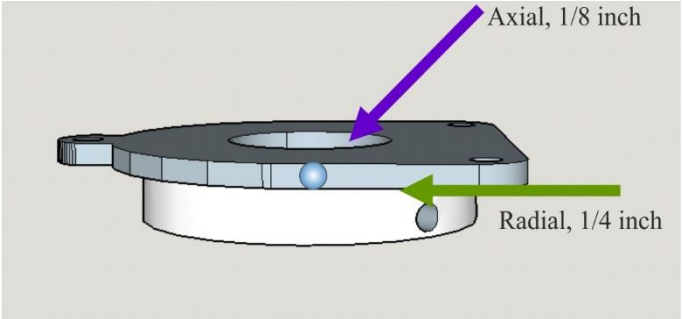

Figure 2.11: Configuration of the inlets for supplying gas flow to the trapping cell on OT2.

All of the inlets are replicated in the Teflon insert with an unobstructed path for gas and aerosol to flow into the cell. The purpose of the axial oriented inlet was to investigate whether directing aerosol into the cell in the radial or axial orientation improved the rate of accretion into the trapped droplet. The internal chamber was cylindrical and had a diameter of 2.43 cm, and a volume of 6.31 cm^3. The volume of the cell was reduced by designing (SketchUp) and 3D printing (RepRapPro, Omerod 2 and Prusa i3 MK3) cell inserts shown

in Figure 2.12. The total internal volume of the cell was reduced by 25, 50 and 75 % to 4.73, 3.16 and 1.58 cm^3 respectively.

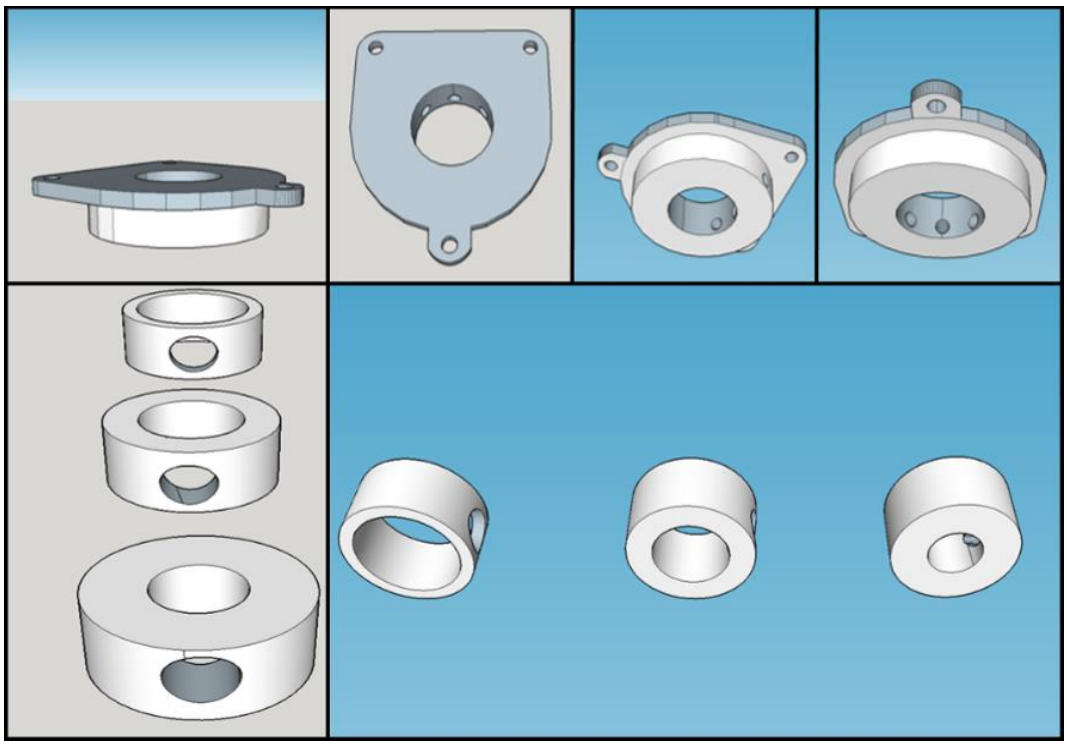

Figure 2.12: Google SketchUp images of the cell and the cell volume reduction inserts. The top row shows the current cell design, the bottom row shows the proposed inserts. These drawings are now used to fabricate the inserts by 3D printing.

2.5.4. Brightfield Imaging

Images and videos could be recorded in the LARA peaksearch fitting program at a rate of 30 Hz. A 500 nm shortpass filter (ThorLabs FES0500) was placed before the camera (ThorLabs DCC1545M) to remove laser light above 500 nm which would overexpose the image. Two lenses resized the image of the droplet ensuring the best image size to image resolution ratio.

2.6. Gas Flow Systems and RH Control

Precise control of the environment surrounding a trapped droplet is crucial to measurement of radius and refractive index as an imbalance in the water activities of the droplet and cell environment can alter the equilibrium water activity of a trapped droplet and, thus, its size and RI. For example, if the RH of the cell is 70 % but the trapped droplet has a water activity of 0.8, some of the water in the droplet evaporates to restore equilibrium until it is equal to 0.7. A series of possible RH control systems were designed and compared to determine the most efficient way to introduce both a humidified gas phase and the sampling

aerosol into the cell. This chapter will deal with the introduction of a humidified gas phase and the introduction of aerosol will be addressed in Chapter 4.

It is possible to use a probe droplet to measure the RH by determining the change in radius and RI of a droplet for which the thermodynamic properties are well characterised, one example of this is sodium chloride aerosol.[83] The solute concentration of the particle can be calculated from the RI if the mass loading of the involatile solute is known. The RH is equal to the water activity, a_w, which is defined as the partial vapour pressure of water over a solution, p, as a fraction of the saturation vapour pressure of pure water, p*, as defined by Equation 2.11. The water activity can be inferred from the concentration of the solute in the solution which can be inferred from the RI. The RH is related to water activity by Equation 2.12.

$$a_w = \frac{p}{p^*} \qquad \text{Equation 2.11}$$

$$RH = a_w \times 100\ \% \qquad \text{Equation 2.12}$$

The nitrogen gas flow system is shown in Figure 2.13. The N_2 is sourced from the liquid nitrogen boil off (purity >98 % from a liquid nitrogen supply) and split into two lines. The first line passes through or over a body of pure water, causing the N_2 to become humidified, while the second line remains dehumidified. The two lines are recombined before passing into the cell and the RH controlled by varying the relative ratio of 'wet': 'dry' N_2. The flow rates (typically 0.05 – 0.5 L/min) were individually controlled using mass flow controllers (MFC's) (Bronkhorst UK). It was possible to access higher flow rates but the increased Stokes drag force imposed on the particle often caused the particle to be lost from the trap.

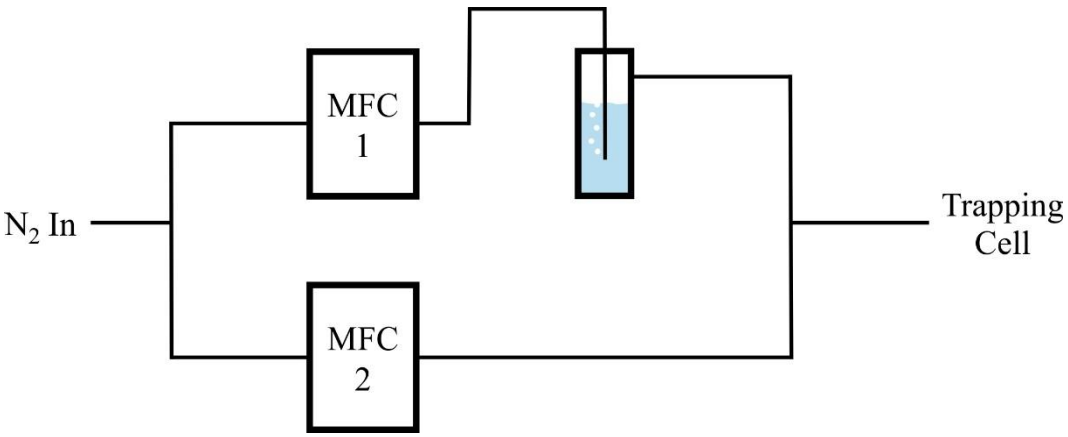

Figure 2.13: Diagram of a basic relative humidity system. Abbreviations: MFC = mass flow controller.

The RH was measured immediately before and after the trapping cell using two capacitance probes (Honeywell). The RH was not directly measured from within the cell as the

introduction of a plume of aerosol can caused deposition of aerosol onto the probe which compromises measurements of RH.

Several variations of the gas flow system layout are displayed in Figure 2.14 and were tested for their efficiency in maintaining a constant RH with and without a trapped droplet, and for the ability to reach high (>98 %) RHs. There are several glassware pieces which can be used to humidify nitrogen: bubblers, diffusers and water boats. The water bubbler humidifies nitrogen as it bubbles through the water in the reservoir from an inlet with a diameter of ~ 1 cm. The diffuser operates on the same principle, but the bubbles are diffused through a silica grit which produces a larger quantity of smaller bubbles. The water boat is a reservoir of water, the nitrogen flows along the surface of the water, becoming humidified during the process.

The most significant difference between the 1/4 inch (in.) diameter radially oriented inlet and the 1/8 in. axially oriented inlet is that gas with the same flow rate experiences a higher velocity when passed through a narrower bore tube. Therefore 0.01 L/min of dry N_2 entering the cell from the axial inlet has a higher velocity than the same flow rate of dry N_2

which imparts greater force on the trapped particle. Table 2.3 shows the maximum RH achieved under different conditions.

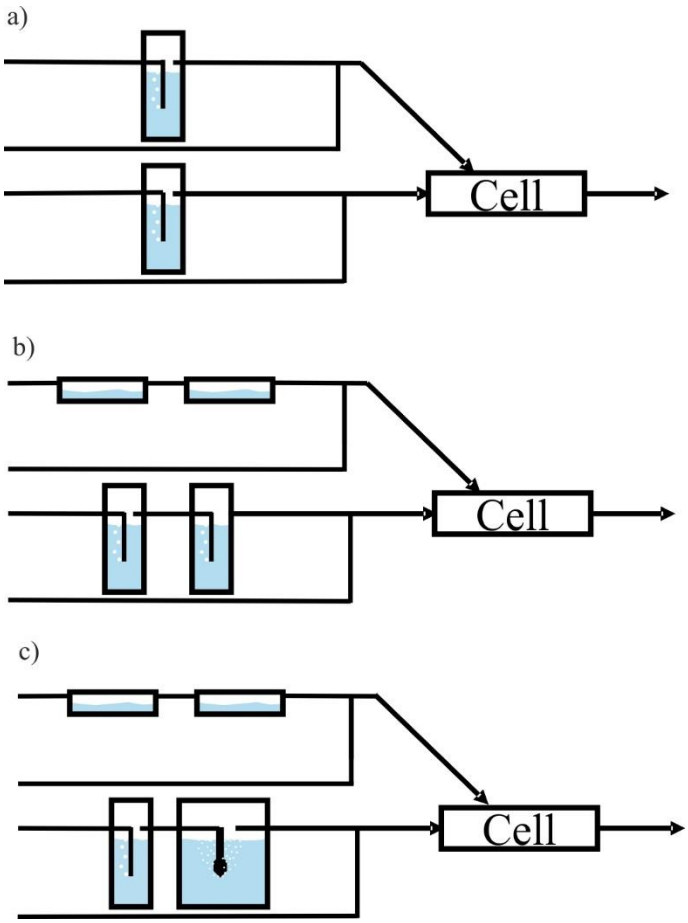

Figure 2.14: A diagram showing the possible variations in gas flow delivery systems.

Table 2.3: Table of the maximum efficiency achieved for different RH control systems. The maximum RH was recorded using a Vaisala probe and left for an hour to equilibrate.

RH Control Setup	Maximum Efficiency / %
One Bubbler	79
Two Boats	82
Two Bubblers	80
One Bubbler and one diffuser	87

For the purposes of stability, the series of boats were used in the axial orientation. The combination of a bubbler and a diffuser was used in the radial orientation to maximise the efficiency in RH control.

2.7. Analysis of Instrument Sensitivity and System Characterisation

The characterisation of OT1 has been used as a baseline for comparison with the performance of new AOT instruments, in this case, OT2. A direct comparison of performance was conducted with the mean standard deviations in the radius, refractive index and transverse electronic first order (TE, l=1) mode wavelength over 200 and 40 second periods. This was a protocol established for assessing performance in Chapter 3. Although the mean residuals for radius and refractive index are subjected to the errors incurred in the fitting process, the wavelength of a whispering gallery mode (WGM) can be used as a more direct proxy for the stability of any AOT system. We use this procedure here as an example of the benchmarking that is performed. Figure 2.15 shows two datasets, one recorded on OT1 (panel a) and another recorded on OT2 (panel b).

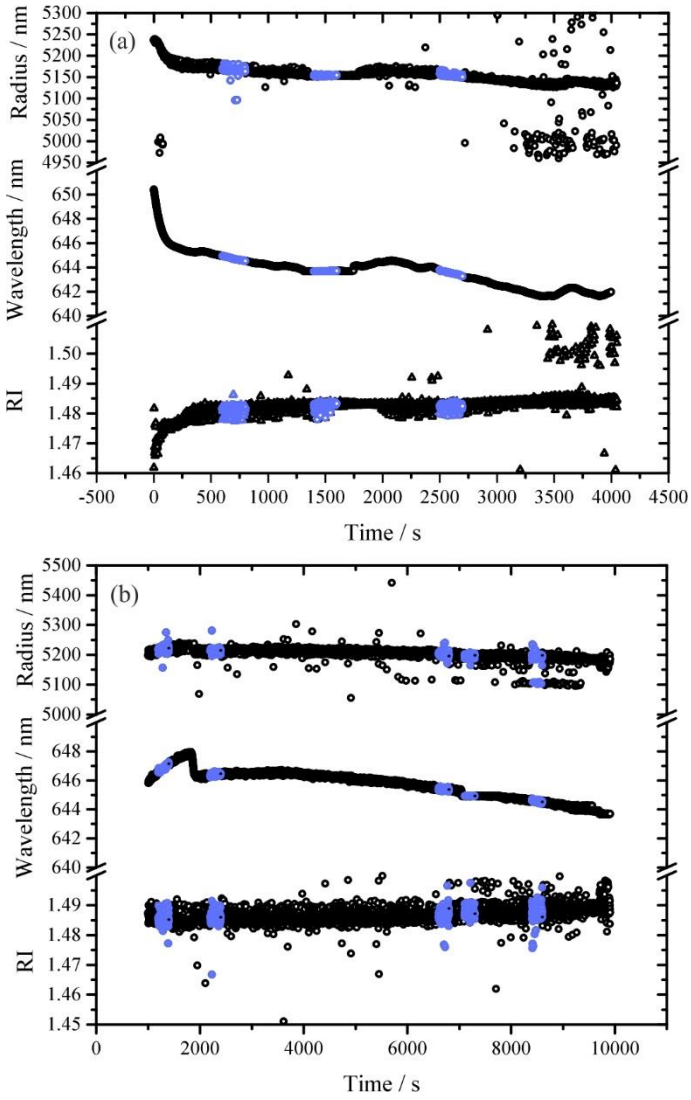

Figure 2.15: Panel a shows the fitted radius, retrieved transverse electronic first order (TE1) whispering gallery mode wavelength and fitted RI of a 5.2 μm droplet trapped using OT1 for ~4000 seconds. Panel b shows the fitted radius, retrieved TE1 wavelength and fitted RI of a 5.15

μm droplet trapped using OT2 for ~ 10,000 seconds. The sections highlighted in blue are 200 s periods of data which are used for analysis.

The two datasets shown in Figure 2.15 are of similar droplet sizes with radii of 5.2 μm and 5.15 μm respectively (OT1, OT2). It is clear that the noise levels associated with the TE1 wavelength, radius and RI are all larger for the OT2 measurement indicating that there is a difference in the sensitivity or noise between the two systems.

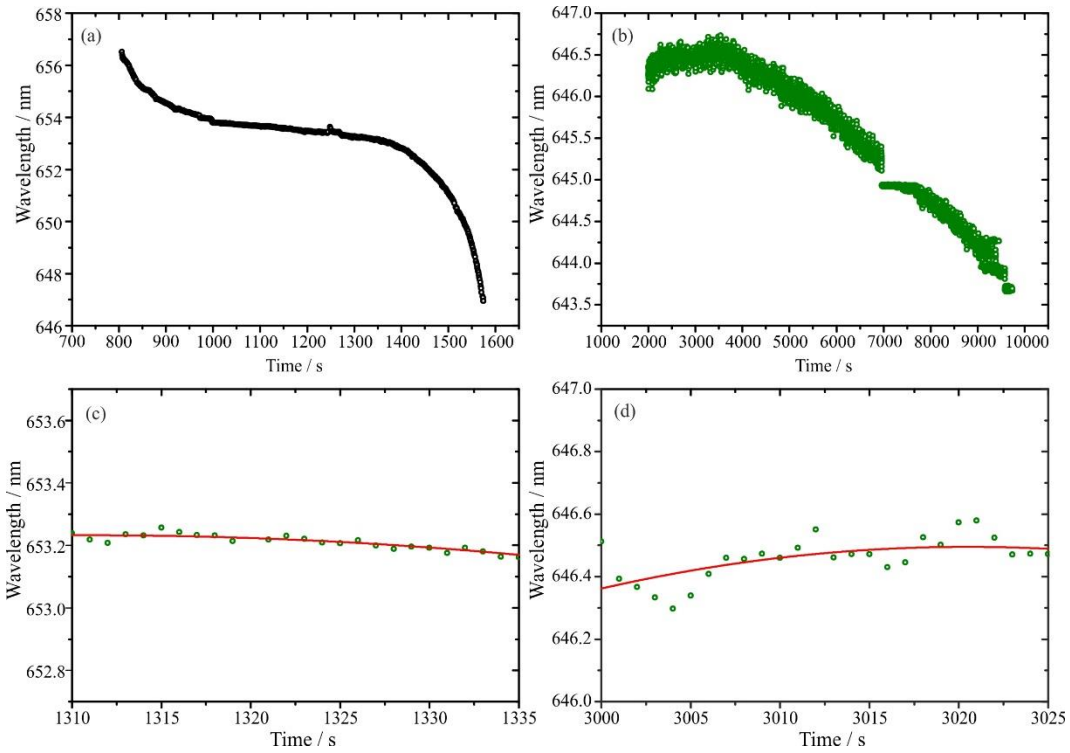

Figure 2.16: Panels a and b show the retrieved transverse electronic first order mode wavelength of OT1, black data, and OT2, green data. Panels c and d show 25 s of time dependence of the TE1 wavelength with a polynomial fit (red) green data.

Figure 2.16 compares the reported TE1 wavelengths for both datasets, showing an expanded view of the time-dependence in wavelength over 25 seconds. The difference in

noise for OT1 and OT2 can be quantified by calculating the mean residual about a polynomial fit trend line normalised for wavelength, shown in Equation 2.13.

$$Normalised\ Residual\ Mean = \frac{\sigma_\lambda}{\lambda} \qquad \text{Equation 2.13}$$

Table 2.4: The average normalised residual for each of the blue sections in **Figure 2.15** for 200 and 40 s time periods.

Averaging Time / s	Average Residual Mean – OT1	Average Residual Mean – OT2
200	1.11E-05	6.54E-05
40	1.71E-06	6.07E-05

The higher average residual means for OT2 suggested that the noise characteristics were inferior to OT1. This could have been due to instabilities in the gas flow or laser power. Each of these areas were individually tested.

2.7.1. Laser Power Fluctuations

Fluctuations in laser power can affect a trapped droplet in two ways. Firstly, the axial position of the droplet in the trap varies as laser power changes, shifting the position of the droplet relative to the laser trap focus.[84] This changes the effective collection efficiency of light by the optical system, which leads to fluctuations in the absolute intensity of Raman light recorded on the CCD and S/N ratio, improving on the accuracy with which the line centres of the WGMs are determined.[82] Secondly, a change in laser power will lead to a slight change in droplet temperature, due to the change in light absorption by the droplet.[82] This promotes evaporation or condensation of water between the trapped droplet and the

cell environment. In turn, this leads to a slight change in droplet radius, shifting the position of the WGM in the Raman spectra and leading to noise in the data.

A laser power meter (Ophir Nova 1z01500) revealed that, when compared to OT1, OT2 displayed significant fluctuations in laser power output, which can be seen in Figure 2.17.

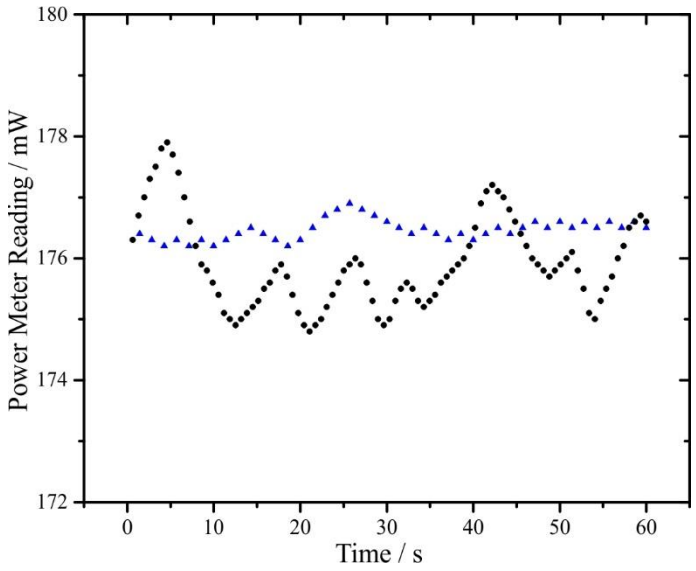

Figure 2.17: A graph showing the fluctuations in laser power over 60 seconds. The blue triangles represent OT1 and the black dots represent OT2.

At low operating powers of ~20 mW, the fluctuations in laser power output over time were ± 1%, which is higher than the <± 0.2% specified by the manufacturer. When compared to the average trapping power on OT1 the fluctuations in laser power were broadening the line centre of the WGM's, the laser was returned to the manufacturer for maintenance checks.

Additionally, two beamsplitters (BS1 50:50, BS2: 70:30) were added to the optical table before the cage assembly (see Figure 2.9) to allow an increase in the operating range of laser power used during experiments and reduce the noise in the line centre of the WGM's. These removed 65 % of the output laser power, directing 35 % to the trapping cell. This helped stabilise the laser power output over time. The optimal operating range was <60 mW: at this laser power 39 mW would be removed by the beamsplitters, directing a 21 mW

trapping beam to the cell which was sufficient to trap a 4 – 5 μm droplet. The laser power was recorded at the cell for OT1 and OT2 and can be seen in Figure 2.18.

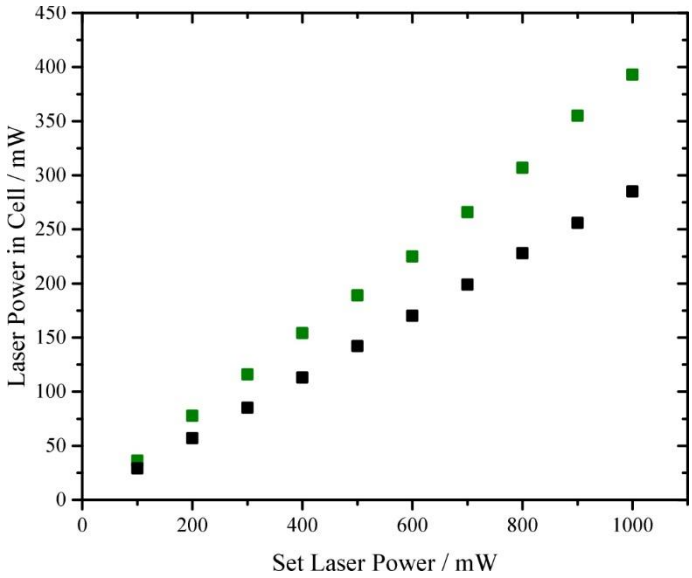

Figure 2.18: Figure showing the recorded laser reaching the cell against the set laser power for OT1 (black) and OT2 (green).

The additional beam splitters allowed the laser to operate at a higher laser power, whilst directing the same proportion of laser power into the cell. This stabilised the droplet in the trap as there were fewer fluctuations in laser power, this is seen as a lower noise in the WGMS wavelengths over time. The residual mean value in the TE1 mode over 200 seconds was reduced from 6.29×10^{-5} to 1.25×10^{-5}, displaying the improvement in laser power stability due to the introduction of the beamsplitter optics. This is similar to the mean residual value on OT1, 1.11×10^{-5}, taken from

Table 2.4.

2.8. Optical Trapping Stability

There were two methods employed to investigate the stability of an optical trap. The first method is to displace a droplet from the trap by gradually increasing the gas flow rate.[85] The second method is to measure the lowest power at which a droplet is retained in the trap by gradually decreasing the trapping laser power.[86] The gas flow method was attempted but it was not successful for determination of trapping stability: a maximum gas flow rate available on either OT1 or OT2 was 0.5 L/min and 0.3 L/min, respectively, and insufficient to reliably measure the maximum gas flow rate a droplet could withstand. Thus, the relative trapping efficiency of the AOT instruments OT1 and OT2 was measured using the second method. Droplets between 3 – 7 μm were equilibrated after trapping for a minimum of 5 minutes and the laser power was reduced at a rate of 2 mW per 10 seconds. The minimum

trapping power at which the droplet fell from the trap was recorded and the variation with droplet size was explored as shown in Figure 2.19. The minimum trapping power is recorded as the amount of laser power sent to the cell, not set on the laser.

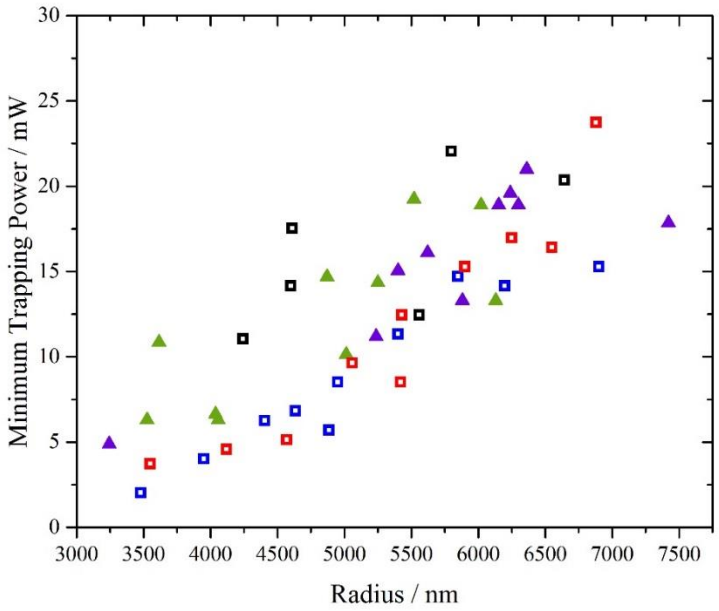

Figure 2.19: A graph showing the minimum trapping laser power (mW) against radius (nm) for both the OT1, squares, and OT2, triangles. On the OT1 system, the gas flow was varied between 0.1 L/min (blue), 0.3 L/min (red) and 0.5 L/min (black). On the OT2 system the delivery of gas flow was changed from radial orientation (green) to axial orientation (purple).

For OT1, droplets between 3-7 μm were trapped and held at 80 % RH with a gas flow rate of 0.1 L/min (blue squares), 0.3 L/min (red squares) and 0.5 L/min (black squares). Gas flow rates above 0.3 L/min clearly had an impact on the trapping efficiency of OT1 as droplets are displaced from the centre of the trap. This can be seen during the experiment and is illustrated in Figure 2.20 apparent from the distortion in reflected laser light from the droplet. Brightfield images taken on OT1 illustrate the effect of a high gas flow rate: the left-hand image is a droplet stable in the trap with a 0.3 L/min gas flow rate, whereas the right-hand image the droplet is pushed towards the edge of the trap by the 0.5 L/min gas flow rate. The gas flow is introduced in the horizontal plane from the left-hand side of the image. Although much of the gas is introduced through a shower head arrangement, the

high gas flow rate introduces an uneven distribution of gas flow within the showerhead configuration.

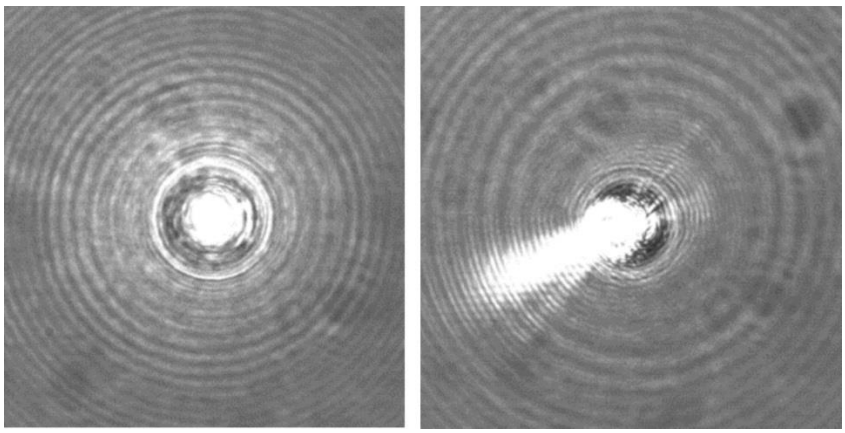

Figure 2.20: Left, a droplet in the trap with a 0.3 L/min gas flow. Right, a droplet in the trap with a 0.5 L/min gas flow.

For OT2, an exploration of the dependence of trapping stability on particle size was conducted. However, instead of focussing on the gas flow rate dependence, the dependence on gas flow orientation at a constant flow rate of 0.3 L/min was examined. The directionality of the gas flow inlet was changed from radial (in the horizontal plane, as for OT1) to axial (directed vertically from above the trapped droplet), see Figure 2.11.

Firstly, a comparison of the trapping efficiencies of OT1 and OT2 indicates that both systems can levitate droplets with similar laser powers and are, therefore, equally stable traps. Further, no difference in trapping efficiency was observed between flow orientations. The delivery tube in the horizontal plane is larger in diameter 1/4 in., than in the axial position, 1/8 in. Despite the resulting increase in gas flow velocity, which occurs due to the same gas flow rate passed through a narrower bore tube and the closer proximity to the trapped droplet, the greater strength of the trap in the axial direction[87] leads to no discernible difference in the trapping efficiency of OT2 at this stage. The distance between the axial inlet and the trap is 5 mm whereas the distance between the radial inlet and the trap is ~25 mm. The closer the gas or aerosol inlet is towards the trap the higher the rate of RH equilibration or accretion efficiency. Therefore, it is an important design constraint to investigate the ability of a trapped droplet to remain stable with higher velocity or proximity of aerosol or gas flow.

It is possible to calculate the axial trapping efficiency, Q, of an optical trap if the minimum trapping power, P, is known using Equation 2.14 and balancing it with the gravitational force experienced by the particle, F.[86] In Equation 2.14, the speed of light is denoted by c

(ms^{-1}) and the refractive index of the surrounding medium, denoted by n_m, is air which has a value approximate to 1.

$$Q = \frac{radiation\ force\ exerted\ on\ the\ particle}{radiation\ force\ of\ the\ incident\ beam} \qquad \text{Equation 2.14}$$

$$Q = \frac{F}{n_m\left(\frac{P}{c}\right)} \qquad \text{Equation 2.15}$$

In Equation 2.15 the gravitational force experienced by the particle, F, can be calculated using Equation 2.16 where r denotes the particle radius,ρ, denotes the particle density and g denotes the gravitational acceleration. The particle density used in this calculation was predicted by the E-AIM model[88] with a value of 1.17055 g cm^{-3} for a sodium chloride droplet with a water activity of 0.8.

$$F = \frac{4}{3}\pi r^3 \rho g \qquad \text{Equation 2.16}$$

The trapping efficiency of each trap under the different experimental conditions has been calculated. For OT1 the mean axial trapping efficiency recorded from 26 experiments was 0.2 ± 0.06; for OT2 the mean axial trapping efficiency calculated from 20 experiments was 0.17 ± 0.06. When compared to literature values, both traps have a high efficiency in the axial orientation (OT1 is superior to OT2). However, the axial trapping efficiency is droplet composition specific and has not been performed on aqueous sodium chloride droplets before now.

2.8.1. Changing the Axial Flow Rate

While droplets have a relatively high tolerance to exposure to gas flows from a single direction, the combination of two gas flow orientations acts to destabilise a droplet. In order to determine the suitability of the axial inlet for this project, the gas flow stability of axial inlet AOT experiments was probed using humidified wet and dry nitrogen gas flow. Firstly, experiments similar to those in section 2.8 were performed to assess the maximum axial flow rate a droplet could withstand before falling from the trap. A sodium chloride droplet with a water activity of 0.8 was trapped using OT2 and held with no axial flow and 0.3 L/min of N_2 radially at 80 % RH to equilibrate. The axial flow rate was increased from 0 in increments of 0.05 L/min every 60 seconds. The axial flow rate at which the droplet was forced from the trap was recorded and is shown in Figure 2.21**:** The dependence of the maximum axial flow rate the droplet can sustain on radius is shown. The axial flow rate was

increased by 0.05 L/min every minute (blue squares) the dependence of the radius on the maximum axial flow rate the droplet can sustain is shown.

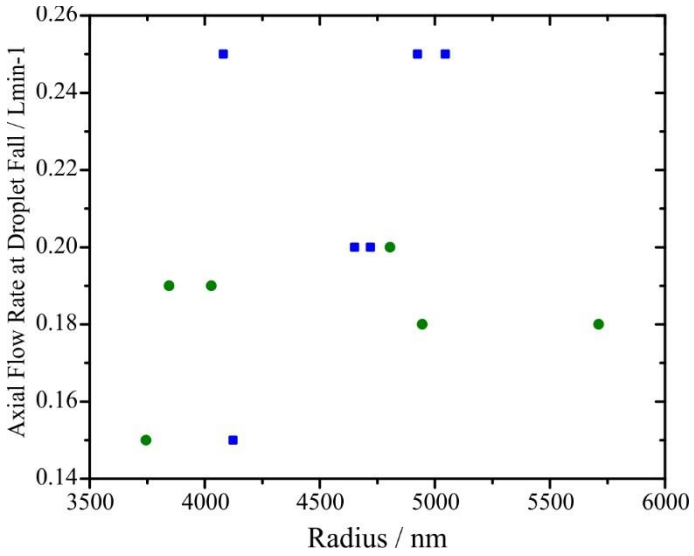

Figure 2.21: The dependence of the maximum axial flow rate the droplet can sustain on radius is shown. The axial flow rate was increased by 0.05 L/min every minute (blue squares) and by 0.01 L/min every minute (green circles).

The maximum axial flow rate range was found to be between 0.15 – 0.25 L/min. This range was more precisely defined by performing the same experiment but using a finer change in axial flow rate increase. The axial flow rate at which a droplet was displaced from the trap is shown in Figure 2.21; the axial flow rate was increased from 0.15 L/min by 0.01 L/min every minute. The average maximum flow rate was found to be 0.18 L/min. Thus, the maximum operating axial flow rate for experiments was established as 0.17 L/min. Using this flow rate in the axial orientation and 0.3 L/min in the radial orientation, a second

trapping stability experiment was performed in which the laser power was decreased, shown in Figure 2.22.

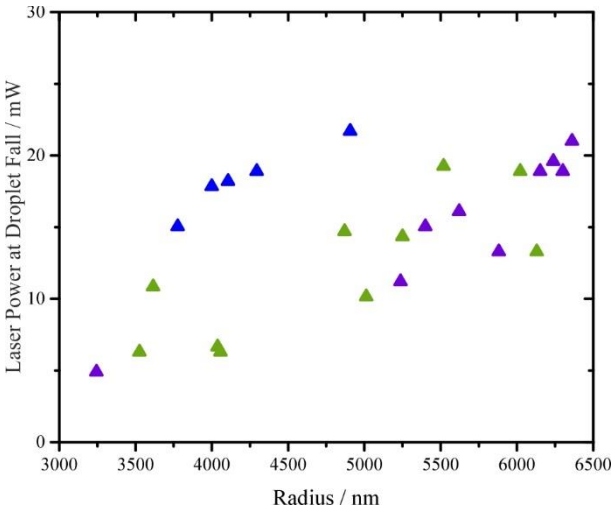

Figure 2.22: A graph of the minimum trapping power in mW against the radius in nm on OT2. The green triangles represent droplets exposed to 0.3 L/min of radial gas flow. The purple triangles represent droplets exposed to 0.3 L/min of axial gas flow. The blue triangles represent droplets exposed to a radial and axial mixed gas flow.

The blue triangles, representing the droplets exposed to axial and radial gas flow, exhibited a higher minimum trapping power than the rest of the data points. This indicated that the droplets exposed to a multi-directional gas flow rate were less stable than those exposed to a gas flow from one direction. The minimum trapping laser powers presented for multi-directional gas flow on OT2 are lower than the minimum trapping power presented for OT1 in section 2.8. Therefore, droplets exposed to a multi-directional gas flow on OT2 can still be considered stable when compared to droplets trapped with OT1.

The relationship between trapping stability and relative mixing ratio of axial and radial gas flow rate was investigated by decreasing the laser power, shown in Figure 2.23. There was no systematic impact on droplet stability observed when varying the relative mixing ratio of radial and axial gas flow, using either a bubbler or a boat. Although the mixing of two

gas flows increased turbulence a droplet would experience within the trapping cell, this is not reliant upon the ratio between the two gas flows.

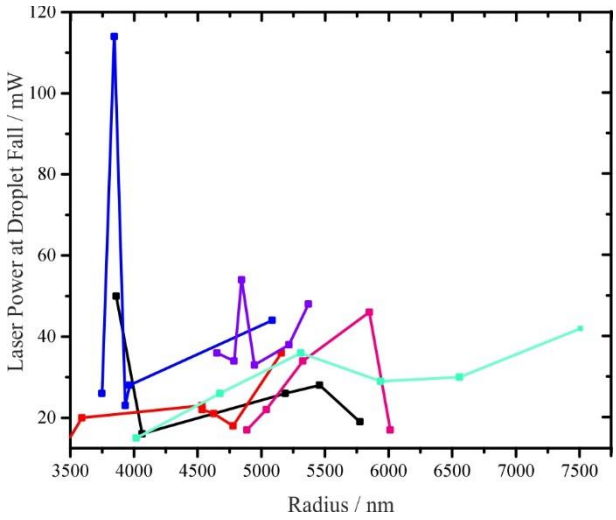

Figure 2.23: A graph showing the relationship between minimum trapping power and droplet radius for varied ratio of radial and axial gas flow rates using either a bubbler or a boat on OT2. The following ratios are all radial : axial- black line, 300:0; red line 275:25; blue line 250:50; pink line 225:75; teal line 200:100; purple line 150:150.

2.8.2. Hygroscopic Response with Varying Gas Flow Orientation and Gas Flow Rate

The rate at which a droplet can equilibrate to a change in the surrounding environment must be characterised for the purposes of accretion measurements as this limits the accretion rate. An increase in the RH of the surrounding cell environment will promote absorption of water into the probe droplet to preserve equilibrium between the gas and condensed phases. This condensation of water onto the probe droplet dilutes the concentration of salts and the mass fraction of water increases. This leads to the hygroscopic growth of the particle.[89] A decrease in the RH of the surrounding cell environment will promote evaporation of water out of the probe droplet, increasing the concentration of the droplet and reducing the probe droplet radius. The hygroscopic response behaviour of sodium chloride has been well defined in laboratory experiments.[44,90]

Measurements of the fitted radius over time were taken using a 0.8 water activity droplet captured on OT2. The droplet was equilibrated to 80 % RH under a radial flow of 0.3 L/min. After ~6000 seconds, an axial gas flow which had been directed over two glass boats in series, each containing deionised water (maximum efficiency of 82.4 %) at a flow rate of 0.02 L/min was introduced to the cell. The total wet-to-dry flow rate ratio conducted through the cell was 0.26:0.06 L/min, which changed the RH within the cell to 81 %. This is a change in RH which is barely perceptible in the fitted droplet radius. The axial flow rate was changed to 0.02 L/min dry; this changed the RH within the cell to 75 % and is

seen in the dataset as a decrease in droplet radius of ~ 100 nm. Upon reintroduction of the 0.02 L/min^{-1} wet flow, combining with the 0.02 L/min dry flow, the RH within the cell was changed to 77 % RH, a resulting increase of ~ 50 nm in droplet radius was observed. This process was repeated with 0.04 L/min increments which changed the RH of the cell to 82 %, 71 % and 74 % respectively. The corresponding change in droplet radius can be seen each time in Figure 2.24.

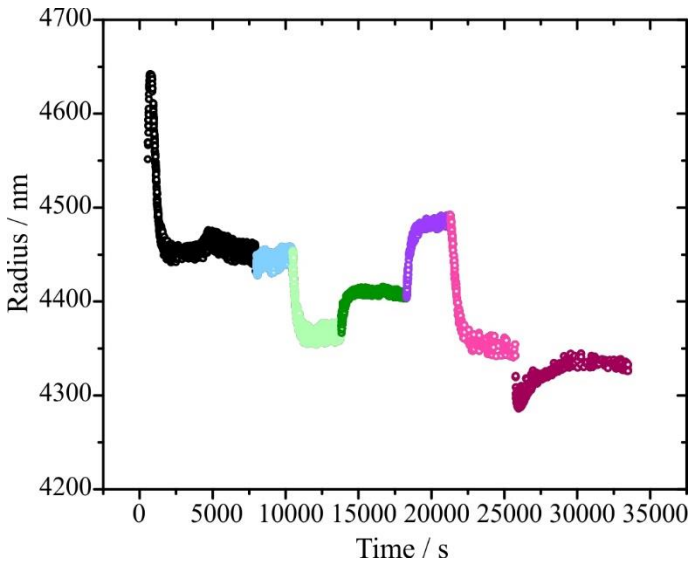

Figure 2.24: A graph showing the fitted radius over time as the gas axial gas flow rate is changed from 0 – 0.04 L/min and the RH is cycled from wet to dry on OT2. The radial flow rate remains at 0.3 L/min. Black section, no axial flow; blue section 0.02 L/min wet; light green section 0.02 L/min dry; dark green section 0.02 L/min wet and dry; purple section 0.04 L/min wet; magenta section 0.04 L/min dry; dark purple section 0.04 L/min wet and dry.

The rate of change in droplet radius can be used to calibrate how quickly a droplet can equilibrate to changes in the environment. Although this is well documented for radial gas flows in aerosol optical tweezers[91] the axial gas flow inlet is not only closer to the droplet but also passes over it with a higher velocity.

2.9. Cell Volume Reductions

Figure 2.18 in section 2.5.3 displayed the 3D printed cell inserts which were designed to reduce the volume of the cell. The inserts were printed to improve accretion measurements by reducing the time taken for a droplet to equilibrate once it is exposed to a new or secondary gas flow, and to increase the accretion efficiency, or uptake of solute due to discrete coalescence events. Before characterising the increase in accretion efficiency, it is

logical to first understand the rate at which a droplet will equilibrate to a change in environmental conditions when the cell volume is reduced.

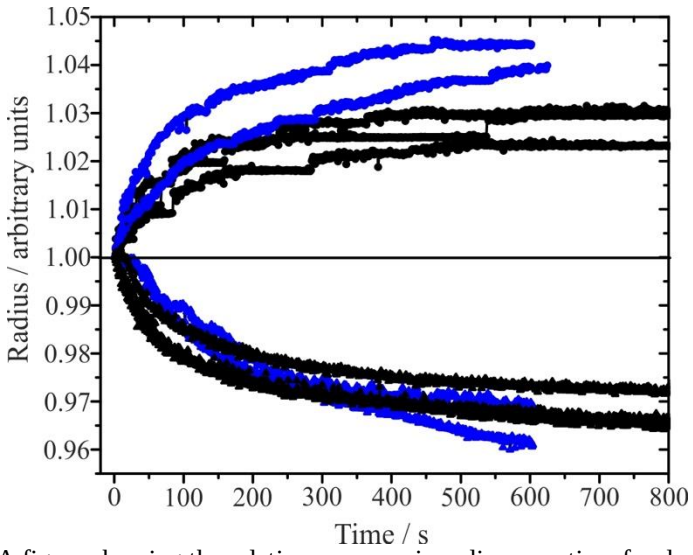

Figure 2.25: A figure showing the relative response in radius over time for droplets in a full volume cell (black data) and a 50 % reduced volume cell (blue data). The top half of the figure shows the increase in radius which occurs when a wet 0.04 L / min flow is introduced axially. The bottom half of the figure shows the decrease in radius which occurs when a dry 0.04 L / min flow is introduced axially. The radial flow rate was 0.1 L / min and held constant throughout all experiments.

Figure 2.25 shows the equilibrating radius over time as an additional flow rate of 0.04 L / min of wet or dry nitrogen was introduced to the cell in the axial orientation. The radial flow rate was held constant at 0.1 L / min and set at 80 % relative humidity. The total RH was increased from 80 % to 86 % when a wet flow was added. The total RH was reduced from 80 % to 57 % when a dry flow was added. In Figure 2.25 the black data represents changes to the probe droplet radius when the surrounding cell volume has not been reduced, and the blue data represents changes to the probe droplet radius when the surrounding cell volume has been reduced by 50 %. There was no obvious variation in the rate of change of the probe droplet radius when the cell volume was reduced. This may be due to the cell not being completely sealed, or perhaps the axial inlet was not situated close enough to the droplet. If the cell volume has little impact on the rate of change of a droplet radius over time, then the accretion rate can be considered a well characterised parameter when a

droplet is trapped within similar cell volumes. However, it is more likely that the cell was not completely sealed, more work is needed in this area.

2.10. CONCLUSIONS

In this chapter a new, research grade, optical tweezers instrument (OT2) was built and customized for the study of accretion into a probe droplet. This instrument possessed additional features, such as the axial inlet, which enabled introduction of gas flow from the axial orientation relative to the probe droplet.

The noise characteristics of this instrument were compared to those of a commercial optical tweezers instrument, OT1. The noise analysis was compared using the deviation from the mean in the wavelength of a WGM. This provided a measurement of how far the data points were positioned from a trendline. The OT2 instrument was found to have inferior noise characteristics to OT1. The source of this additional noise was attributed to instabilities in the laser power, and additional beamsplitter optics were introduced before the trapping cell to improve the laser stability. This was successful and upon repeating the measurement of deviation in the WGM, the noise characteristics of both instruments were found to be comparable. It is recommended that all future Raman based optical tweezer instruments undergo noise analysis to ensure the noise characteristics of each instruments are of a high standard.

A second noise analysis was performed on both instruments using the minimum laser power required to levitate a droplet. The results showed that both systems could levitate droplets with similar levels of laser power. A series of experiments were formed to investigate the influence of gas flow rate and gas flow orientation on trap stability. There was no difference in trap stability when gas was introduced in the axial orientation, despite the higher velocity of gas introduced axially. The enhanced stability of the trap in the axial orientation was thought to be due to the greater trap strength in the axial orientation, providing greater stability to the droplet. However, droplets exposed to a multi directional gas flow were less stable than droplets exposed to a gas flow from one direction. It is thought that the mixing of gas flows inside the cell creates turbulence which destabilises the trapped droplet. It is recommended that the sampling aerosol is introduced from one direction for the detection of CWAs *via* coalescence sampling.

A final investigation was performed to quantify the effect of cell volume on the rate of droplet equilibration. There was no obvious variation in the rate of change of the probe

droplet radius when the cell volume was reduced. It is thought that due to imperfections in the machining of the trapping cell, the cell was not completely sealed, and the volume was effectively infinite. It is concluded that further work is required to understand the rate of equilibration of a trapped droplet.

3. Assessing the Sensitivity of the Aerosol Optical Tweezers

In order to assess the capability of the aerosol optical tweezers (AOT) for the detection of chemical warfare agents (CWAs) in ambient atmospheric conditions, it is imperative that the sensitivity of the system is comprehensively characterised and optimised. Previous work has probed the compound specific limits of detection for several CWAs using the Henry's law constants to determine the degree of partitioning from the gas to particle phase.[92] Other work has also determined the influence of error in the reported whispering gallery mode lineshape on the retrieved droplet size.[81] This chapter furthers the assessment of the noise characteristics of the AOT technique using an Allan variance approach to determine, amongst other things, the minimum resolvable signal and optimal acquisition parameters.

3.1. Introducing the Allan Variance for Analysis of AOT Sensitivity

All physical measurements are vulnerable to the limitations of measurement resolution, which are restricted thermally or by a random fluctuation 'noise' component. Within any signal lies several components: the true signal, Gaussian noise, white noise, 1/f noise, random walk and flicker noise. One of the defining characteristics of white noise is that it averages to zero; this feature is employed in an Allan variance analysis to determine the optimal integration time which maximises the signal-to-noise ratio of a signal. An Allan variance analysis can also indicate which type of noise is most significant in contribution to a signal. It is particularly powerful for assessing the low frequency noise component.

The Allan Variance method was first published by David W. Allan in 1987 and was used as a measure of frequency stability in clocks and oscillators.[93] Allan variance is a statistical analysis in which the integration time period is varied from 1 signal per integral to an entire data set of signals per integral. Typically, a dataset will become more representative of the true value as the time period of averaging is increased, as the white noise components are averaged out of the dataset. When the time period of averaging, τ, becomes too large, the quality of the measurement can begin to degrade. This turning point enables the determination of the optimal averaging time, with the highest signal-to-noise ratio for a

measurement. An Allan variance is calculated using Equation 3.1 where σ_A is the Allan variance of the whole dataset, A_1 and A_2 are subgroups of the dataset which are adjacent to one another in time series and have no dead time in between.

$$\sigma_A^2 = \frac{1}{2}[A_2 - A_1]^2 \qquad \text{Equation 3.1}$$

Equation 3.2 to Equation 3.4 describe the calculation of the variance of the mean Var(A), for a whole dataset in which N is the total number of points in the subgroup, A, and x_i is a dataset where i starts at 1.

$$A_n = \frac{1}{N}\sum_{i=1}^{N} x_i \qquad \text{Equation 3.2}$$

$$\sigma^2 = \frac{1}{N-1}\sum_{i=1}^{N} (x_i - A_n)^2 \qquad \text{Equation 3.3}$$

$$Var(A) = \frac{\sigma^2}{N} \qquad \text{Equation 3.4}$$

N data points are divided into M subgroups as seen in Figure 3.1. Each M subgroup has d elements, for each subset n = 0, 1, 2, 3…, and the number of subgroups is calculated by

M=N/d. The integration time, τ, can be calculated if the sampling period, t_0 is known. In this thesis the sampling period is always 1 second.

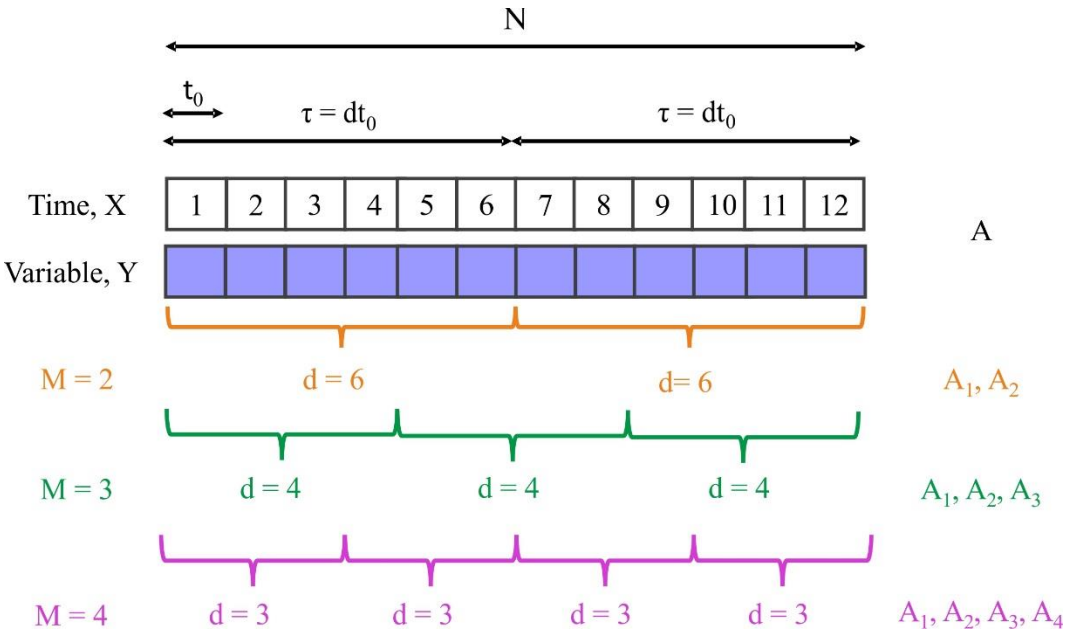

Figure 3.1: A schematic showing the division of a dataset with N values into M subgroups, each subgroup has d elements and a mean value A_n. These values are used to calculate and Allan variance.

More generally, the mean value, A_n, the variance, $(\sigma_A)^2$ and the variance of the mean, $Var(A_n)$ can be deduced for a subgroup using the following equations:

$$A_n = \frac{1}{d}\sum_{l=1}^{d} x_{(n-1)d+l} \qquad \text{Equation 3.5}$$

$$\sigma_n^2 = \frac{1}{d-1}\sum_{l=1}^{d}\left(x_{(n-1)d+l} - A_n\right)^2 \qquad \text{Equation 3.6}$$

$$Var(A_n) = \frac{\sigma_n^2}{d} \qquad \text{Equation 3.7}$$

$$\sigma^2(M, \Delta\tau, \tau) = \frac{1}{M-1}\sum_{n=1}^{M}(A_n - A)^2 \qquad \text{Equation 3.8}$$

As an example, when the dataset is divided into two subgroups, M=2, and d is half of N, the variance of the mean can be expressed as:

$$Var(A, M=2)=\frac{1}{2-1}\sum_{n-1}^{2}(A_n-A)^2 \qquad \text{Equation 3.9}$$

$$Var(A, M=2)=\frac{1}{2}[A_2-A_1]^2=\sigma_A^2=\frac{\sigma^2}{2d} \qquad \text{Equation 3.10}$$

The Allan variance, σ_A^2, corresponds to the variance of the mean which can, in turn, be used to determine the instrument specific limit of detection, an optimal integration time and the experimental conditions which improve the signal to noise ratio.

3.2. A TYPICAL ALLAN VARIANCE ANALYSIS

A typical Allan variance graph is shown in Figure 3.2. Two Allan variance graphs are easily read and compared when displayed as a log-log distribution of the Allan deviation, $\sigma(\tau)$, the square root of the Allan variance. The optimum averaging time is derived from the crossover between two limiting regimes: (1) the improvement in the accuracy in the measured quantity which comes from averaging the measurement over a long period of time; (2) the degradation in the accuracy of the measured quantity that comes from the low frequency noise impacting on the averaged signal over a long period of time. In AOT measurements, the radius changes over the course of an experiment due to factors such as a change in RH and temperature. These are examples of environmental drift and can be seen in an Allan variance plot as low frequency noise leading to a deterioration in the Allan variance at long integration times.

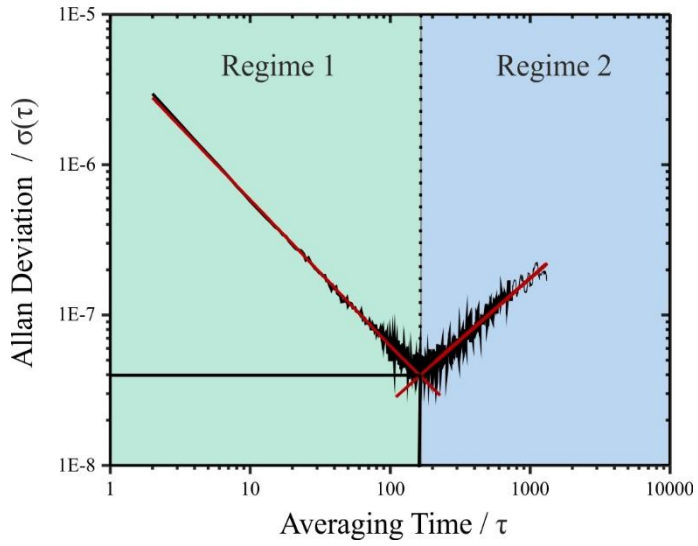

Figure 3.2: A Typical Allan variance graph which shows the improvement in the measured quantity (RI) that occurs when averaging over ~100 s, shown in green by regime 1. This is

followed by the deterioration at longer times due to low frequency drift in environmental conditions, shown in blue by regime 2.

3.2.1. SIMULATED ALLAN VARIANCE

The software used to perform the Allan variance on AOT data was written in LabView 2013 by Dr. Jim Walker. Initial work was undertaken on simulated data sets to explore the different features of the Allan variance and how they qualitatively arise from variations in the time-dependent signal and can be used as signatures of environmental drift in AOT measurements. A random number generator was used to create a simulated dataset with a series of data points evenly distributed in time with values between 5 and 6 to simulate white noise in a dataset. Figure 3.3 shows that an increase in the dataset length can be expected to qualitatively impact the Allan variance when the data is uniformly distributed around a mean value. For both the 8000 second case, Figure 3.3.(a), and 16000 second case, Figure 3.3.(b), the Allan variance does not achieve a minimum point, a consequence of the uniform distribution of data and the absence of a low frequency noise component in the

signal. Increasing the integration time only increases the accuracy of the 'measurement' as shown by the continuous decrease in the Allan deviation.

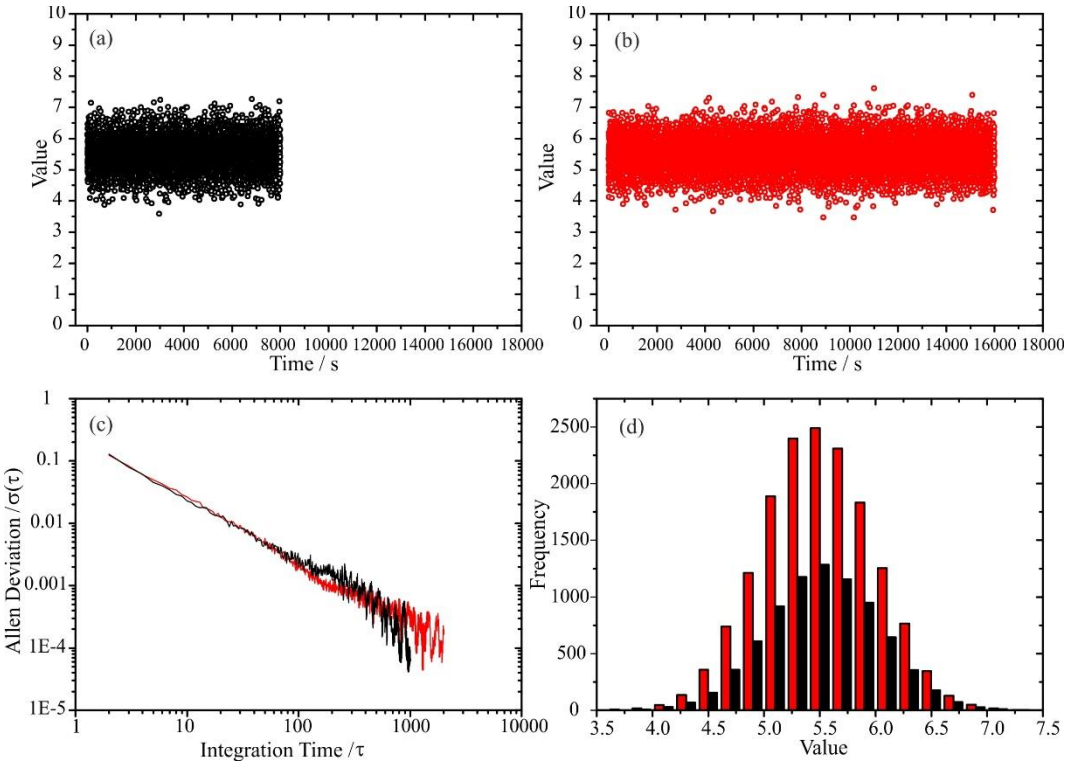

Figure 3.3: (a) Figure showing a simulated dataset with 8000 datapoints. (b) Figure showing a simulated dataset with 16000 datapoints. (c) An Allan deviation of (a) and (b), (d) a graph showing the frequency distribution of the data in panels (a) and (b), a normal distribution.

As a second exploratory test, a positive gradient was applied to the simulated dataset in Figure 3.3. The addition of a systematic variation in the 'measurement' led to a clear minimum in the Allan variance. The larger the gradient applied to the dataset, the lower the optimum averaging time. This also led to an increase in the Allan deviation at the minimum. The applied gradient can be compared to adding a low frequency noise component to the

signal, for example an RH drift or temperature drift over the course of an AOT measurement.

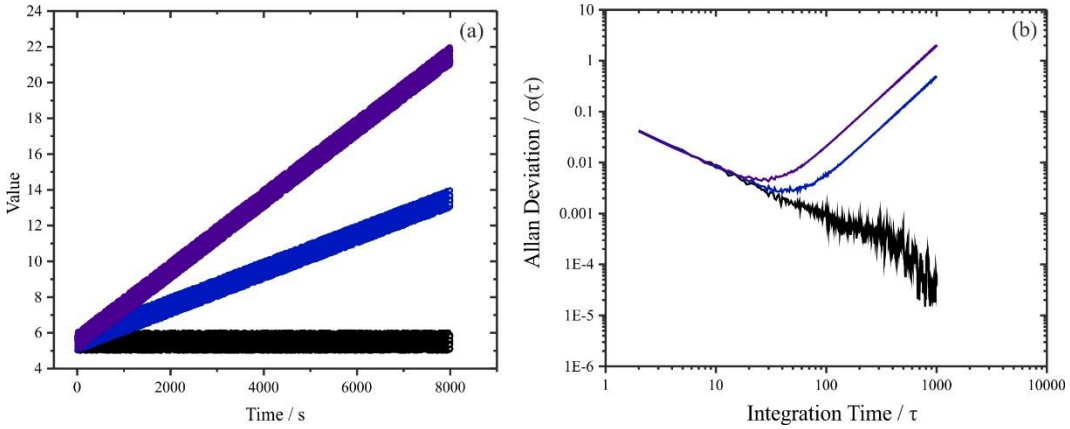

Figure 3.4: a) Graph showing an 8000 second simulated dataset (black), along with two simulated datasets with a positive gradient applied (blue and purple). b) Allan variance of the three different simulated datasets from (a).

When an oscillatory component, a sine wave, was applied to the simulated dataset (shown in Figure 3.5), the Allan variance also reached a minimum point. If the frequency of oscillation is increased, the optimum averaging time decreases, and the Allan deviation increases at the minimum of the Allan variance. This can be compared to adding a white noise component to the signal. As the frequency of the oscillation is increased, the mean value of subsets of the dataset varies more over time, an example would be an oscillation in RH caused by the air conditioning swing setting in the laboratory. These simulations

have shown that the Allan variance software works for the continuous datasets and provides an understanding of the form of an Allan variance analysis.

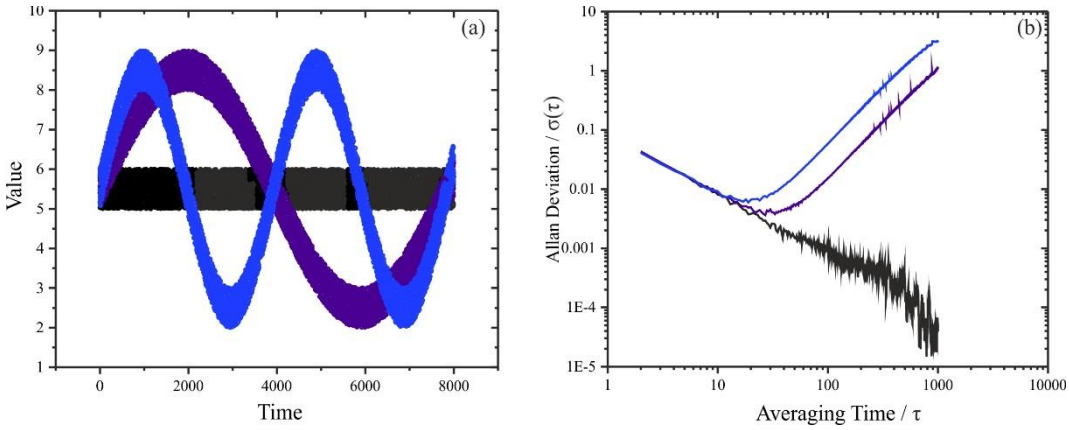

Figure 3.5: a) Graph showing an 8000 second simulated dataset (black) with two different sine waves superimposed (blue and purple). b) Allan variance plots of the three datasets from (a).

3.3. TIME DISCONTINUITIES IN THE DATASET

To provide an Allan variance analysis of a 'live' measurement, the observables (radius, refractive index (RI) and Raman band intensities) must be reported continuously. However, upon undertaking an Allan variance analysis, it became clear that datasets were often not continuous records of radius and RI, a consequence of frame-to-frame variations in the Raman noise leading to uncertainties in resonant mode wavelengths. This became clear as the software was unable to process the data when there were missing data points. The analysis of such a discontinuous data set must be fully understood; only if radius and RI values are estimated during every acquisition step can the detection sensitivity of the optical tweezers approach be fully achieved. The absence of a reported radius/RI value in any time step is a consequence of it falling outside the acceptable error threshold set in the analysis and reporting steps in the LARA software. This can be caused by a fluctuation in the number of resonant modes identified and, thus, analysed by the peak searching algorithm, leading to time discontinuities in the dataset. These are all dependent on the droplet size and RI range chosen for the measurement, one of the reasons that a more detailed noise analysis was required.

In terms of Allan variance, when there are a significant number of gaps in the dataset, shown by the red section of data in Figure 3.6(a), there are no subsets of more than 800 seconds without missing data, 3.3 % of the data points are missing. This clearly limits the

maximum integration time that can be interrogated by the Allan variance approach and must be recognised when drawing conclusions from the analysis. The blue section of data in Figure 3.6(a) has a much better fit because there is a lower proportion of missing data points, 0.5 % of the datapoints, and a minimum in the Allan variance is achieved.

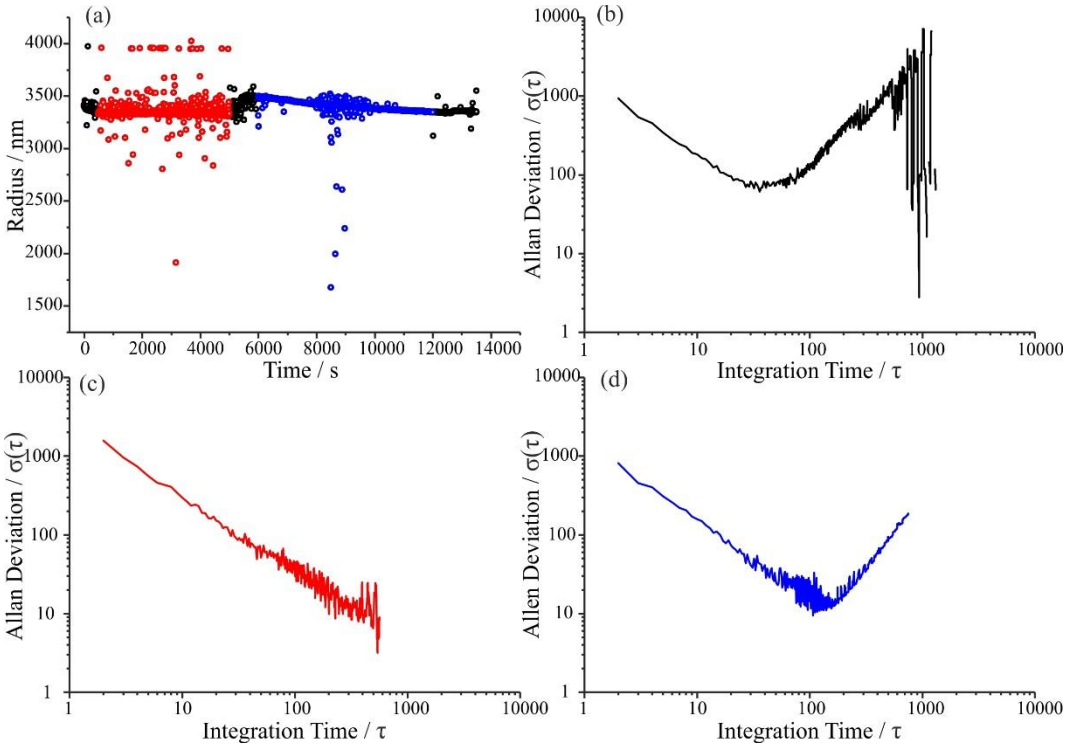

Figure 3.6: (a) A graph of the radius of an aqueous sucrose droplet over time for a period of 14,000 seconds, the full dataset is represented by the black points. The dataset has been divided into different sections constant radius represented by the red points and a decreasing radius represented by the blue points. (b) An Allan variance analysis of the whole dataset. (c) An Allan variance analysis of the red section of data from (a). (d) An Allan variance analysis of the blue section of data.

If for example the fifth data point was not fitted from the Raman spectrum, one method of accounting for the sporadic absence of points from the analysis is to shorten the whole dataset, reporting the Allan variance for an average over a sequence of consecutive measurements rather than integration time. As an example here this approach was applied

to the dataset in Figure 3.7(a) and the difference in the Allan variance is shown by the purple line on the Allan variance analyses in Figure 3.7(b), (c) and (d).

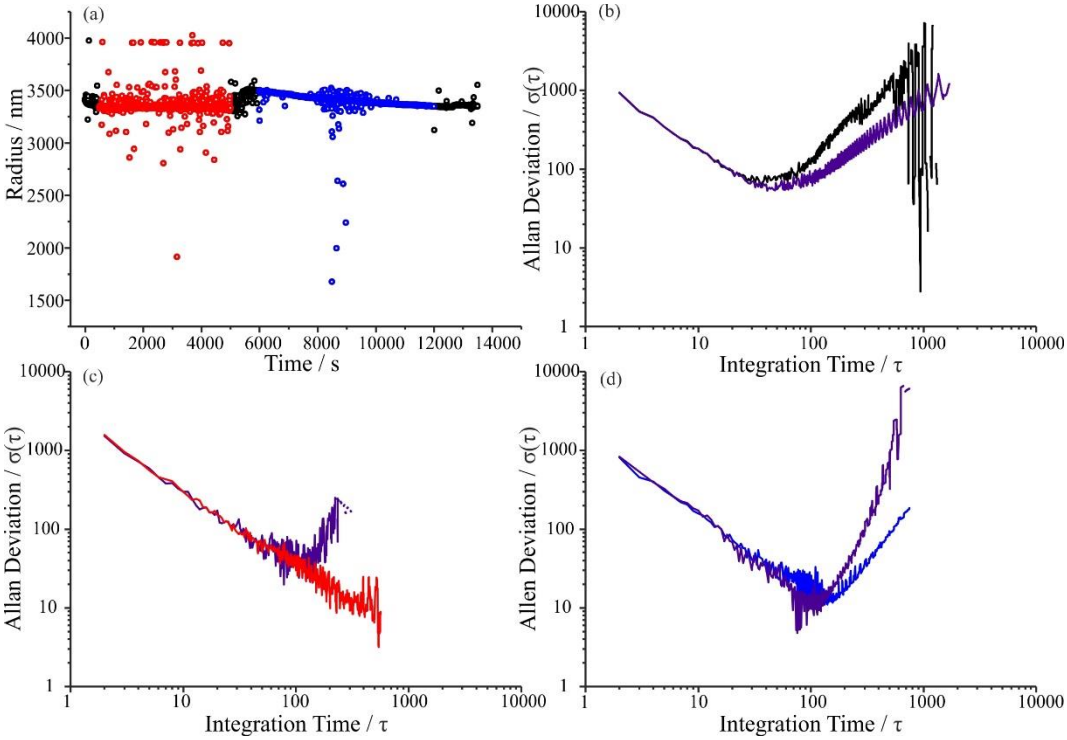

Figure 3.7: Panel (a) shows the dataset from Figure 3.6. Panels (b), (c), and (d) show the Allan variance analyses of the whole dataset (black) and the red and blue sections of data with the gaps in the data included (red, blue and black lines) The purple lines overlaid on panels (b), (c) and (d) show the Allan variance with the gaps in the data removed.

The Allan variance is calculated as a function of averaging over consecutive reported data points rather than integration time. The Allan variance reaches a minimum point when the signal to noise ratio is maximised. However, when the record of data points is not continuous, which is often the case with AOT measurements, the Allan variance cannot be calculated. Any outlying data points, which were erroneously fitted by the LARA software are removed by post processing, which introduces time discontinuities to the dataset. This clearly highlights a challenge associated with undertaking AOT measurements, with specific regard to detection of chemical warfare agents, as the time series data must be optimised without discontinuities. We shall see that this can be achieved by the use of droplets of the appropriate size, which can be deduced by completing a rigorous Allan variance analysis of the measurements of droplets with a wide range of size and RI. This analysis method is only applied when there is a continuous record, with a low percentage, <5 % of data missing. In a case where the fitted radius and RI is not a continuous record of time series data, with more than 5 % of data missing, the dataset will be re-analysed by the software with an in-depth study of the WGM assignments. If no improvement can be made

the data set is discarded. This method removes the user variation in the analysis of noise and enables the use of the Allan variance analysis.

When there is a low percentage of data points missing, for example the 3.3 % of data points missing in the dataset in panel (b) of Figure 3.7, the minimum point of Allan deviation is similar both when the gaps in the dataset are removed (purple line) and when they are left in (black line). This suggests that when there is a low proportion of missing data points the Allan variance analysis is still able to identify the minimum point of Allan deviation at which the environmental drift factors begin to affect the dataset.

3.4. ALLAN VARIANCE ANALYSES AND OPTIMAL INTEGRATION TIME

Figure 3.8 displays the time-dependent variation in radius, Raman intensity ratio, and refractive index for a 4100 nm droplet at ~80 % Relative Humidity (RH). The droplet is composed of sucrose in water at a concentration of 0.7 mol dm^{-3}. The variation in the radius is mirrored in the refractive index and is a function of environmental drift in the relative humidity. Whispering gallery modes passing through one of the spontaneous Raman integration windows (CH or OH) can lead to significant changes in the Raman intensity ratio. These time-periods are not considered in the Allan variance analysis as they provide an additional noise component that can be easily recognised.

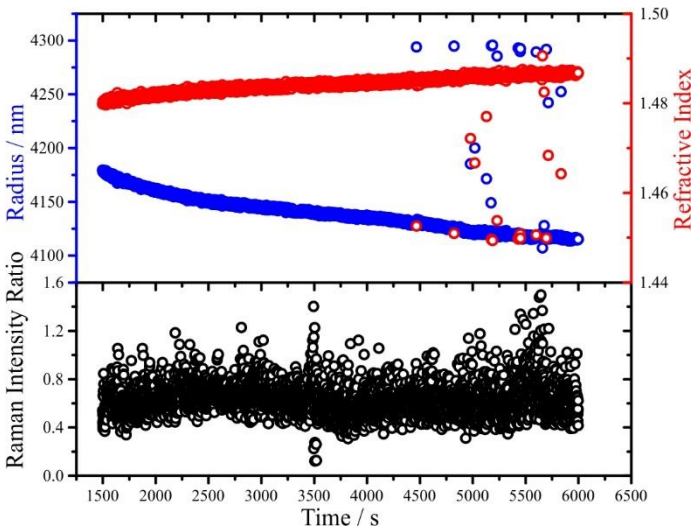

Figure 3.8: The time-dependence in the droplet radius (blue), Raman intensity ratio (black) and refractive index (red) for a 4100 nm droplet at ~80 % RH.

From the Allan variance shown in Figure 3.9, it is evident that the noise in the measurement can be minimised if the integration time is 70 – 80 seconds when analysing droplet radius,

150 – 160 seconds when analysing refractive index and 50 – 60 seconds when analysing Raman intensity ratio. The fitted radius and RI are used as surrogate measurements of environmental drift as conventional probes are unable to give sufficient accuracy. For example, an RH capacitance probe has an error of ± 2% (this can be seen in Figure 3.14).

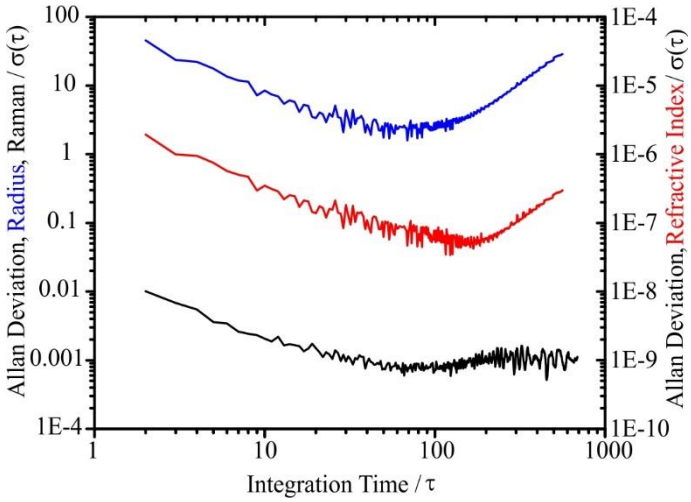

Figure 3.9: Allan variance analysis of the radius (blue), Raman intensity ratio (black) and refractive index (red) for a 4100 nm droplet at 80 % RH.

A series of experiments were conducted at a series of relative humidities (80 %, 65 % and 50 %). The majority of datasets were taken at 80 % relative humidity and will be the focus of much of the discussion. A total of 73 droplets ranging between 3 – 7 μm in radius have been examined, and an Allan variance analysis performed for each. All data sets were acquired with the commercial AOT (OT1) and the radius, RI and dispersion in RI were

fitted offline using the LARA peak search program. A summary of the Allan variance analysis at an RH of 80 % is reported in Table 3.1.

Table 3.1: Optimum averaging time for droplets between 3 – 7 μm at 80 % relative humidity.

Radius / μm	**Optimum Averaging Time, τ, for Radius / s**	**Optimum Averaging Time, τ, for Refractive Index / s**	**Optimum Averaging Time, τ, for Raman Intensity Ratio / s**
3.35	185.7	312.7	83.2
3.45	80.1	97.1	36.6
3.5	175.1	89.7	10.5
3.7	139.3	302.0	36.8
4	80.0	159.9	44.3
4.75	79.9	160.9	48.8
5	194.8	267.2	39.0
5.1	109.3	161.0	23.1
6.1	77.8	208.5	12.3
6.8	241.9	--	23.5
6.8	103.9	180.1	10.0
7	103.8	172.0	6.7

There is a gradual reduction in the optimum averaging time for the Raman intensity ratio as the droplet size increases. Fluctuations in environmental conditions that lead to condensation and evaporation on to or away from the droplet could lead to more apparent fluctuations in the Raman band intensities as the signal improves with larger droplet size. However, these also lead to larger and more obvious fluctuations in size and refractive index on the same timescale. Thus, given that the optimal integration time is shorter for the Raman intensities than for the radius and RI retrievals, it cannot be environmental fluctuations that determine the optimal integration time for the Raman intensity. Much of the noise associated with the Raman band intensity is due to the process of recording spectra and a more detailed discussion of these factors will be addressed later.

The optimal averaging times for radius and RI show no systematic dependence on droplet size and vary significantly from experiment-to-experiment. In effect, the low frequency environmental noise is variable from measurement-to-measurement, sometimes due to a slow upward/downward drift (as in Figure 3.4), sometimes due to a fluctuation or oscillation about a mean (as in Figure 3.5). The timescale for these environmental

fluctuations is usually >1 minute but can be irregular from measurement to measurement. However, the Allan variance consistently decreases for at least the first 70 s.

From these measurements, one can conclude that fluctuations in the droplet size and RI retrieval are necessarily limited by environmental fluctuations at times longer than ~60 s (minimum), independent of droplet size. For droplets of size < 5 μm, the optimal integration time for Raman intensity ratio is ≥ 40 s. Thus, the recommended time-integration is ~ 40 s to optimise the determination of droplet size, RI and Raman intensity ratios with droplets of size 4 – 5 μm. For use in the AOT aerosol detection technique, while the minimum integration time is 1 second, but an integration time of 10 – 20 seconds can improve the signal to noise ratio by an order of magnitude. An increase in integration time up to 40 seconds will be advantageous to the signal to noise ratio. The recommended 40 second integration time frame balances the improvement in sensitivity (improvement in signal-to-noise ratio) that comes from averaging for longer, minimises the impact of unpredictable low-frequency noise, while providing a single time integration window for concurrent measurements of all three quantities.

The minimum Allan deviation values for each of the measured quantities are represented in Table 3.2. A number of conclusions can be drawn from the Allan deviation at the optimal integration time. Given that the Allan deviations for can vary by three orders of magnitude

when varying the integration time, the minimum deviations for measurements of radius and RI are remarkably similar and independent of droplet size (excluding the smallest size).

Table 3.2: The minimum Allan Deviation in radius, refractive index and Raman intensity ratio for droplets between 3 – 7 μm at 80 % relative humidity at the optimum integration time.

Radius / μm	**Minimum Allan Deviation, σ(τ) in Radius**	**Minimum Allan Deviation, σ(τ) in Refractive Index $\times 10^{-7}$**	**Minimum Allan Deviation, σ(τ) in Raman Intensity Ratio $\times 10^{-5}$**
3.35	20.8	20	12
3.45	5.1	2.2	12
3.5	2.5	3.3	19
3.7	1.8	1.2	180
4	1.3	0.4	82
4.75	1.3	0.4	0.5
5	3.6	1.6	30
5.1	2.5	14	0.7
6.1	1.9	0.3	11
6.8	1.3	--	5.7
7a	7.3	1.6	7.4
7b	7.1	1.6	8.8

The minimum Allan deviations presented in Table 3.2 suggest that the size dependence in the accuracy in the radius and RI determinations is modest compare to the more significant introduction of noise to the measurement of each quantity from environmental drift. The Allan deviations for radius and RI track each other very closely which reinforces the conclusion that the radius and RI are equally well determined by the fitting of the WGM mode set.

The Allan deviation for the Raman intensity measurement at the optimal integration time varies considerably more, spanning almost 3 orders of magnitude. This simply reflects the much lower optimal integration times for the Raman measurements reported earlier than the integration times for radius and RI, leading to considerably larger variations from measurement-to-measurement in the improvement in signal-to-noise that is achieved during this limited time integration window. By contrast the size and RI are inherently dependent on wavelength measurements rather than intensity. As previously mentioned,

the noise contributors for Raman band intensity are specific to the spectrographic processes of recording spectra and are discussed later.

3.5. RECOMMENDATIONS

Based on these observations it is recommended that any possible gain in accuracy in radius and RI determination with increase in size, *i.e.* any reduction in the noise associated with these quantities, is completely secondary to the primary source of noise in the measurement that can be attributed to environmental drift. Therefore, it is considered preferable to use smaller droplets rather than larger droplets as a sampling volume to detect chemical warfare agents in an environment. It is recommended that the very smallest droplet sizes are avoided due to the significant decrease in the number of WGMs appearing in the Raman spectrum and their increasing breadth, which will limit the accuracy of the radius and RI determinations; this is apparent from the minimum Allan deviations in Table 3.2. Therefore, the ideal compromise between these small and large size limits is droplet radii in the range of 4 – 5 μm. Figure 3.10 shows the calculated number of coalescing particles required to change the radius (by 2, 3 or 5 nm) and refractive index (by 0.0005, 0.0007, or

0.0009) as a function of the diameter of the coalescing particles. This is calculated with a probe droplet of aqueous sodium chloride at a water activity of 0.8.

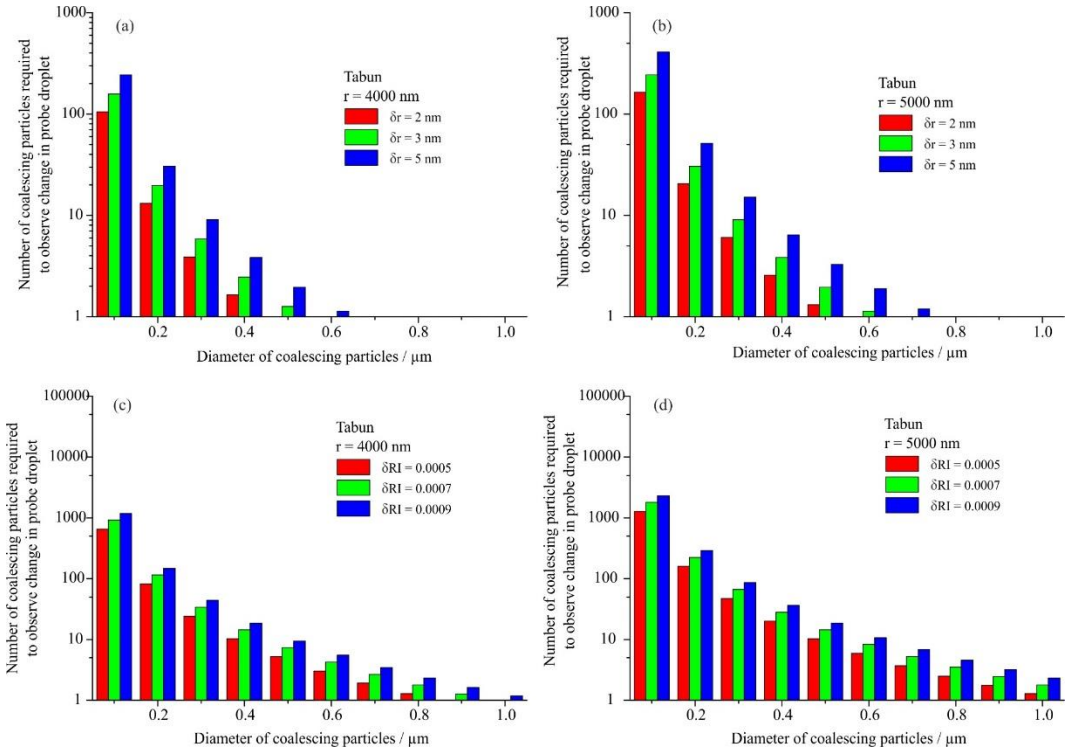

Figure 3.10: Four graphs showing the number of coalescing particles required to observe a change in a 4000 nm probe droplet (a) and a 5000 nm probe droplet (b) radius by 2, 3 and 5 nm (red, green, blue) respectively. These values are displayed as a function of the diameter of the coalescing particles and are specific to the CWA Tabun. Panels (c) and (d) show the number of coalescing particles required to change a 4000/5000 nm probe droplet refractive index by 0.0005, 0.0007 and 0.0009 (red, green, blue) as a function of the diameter of the coalescing particles.

The coalescing droplets are assumed to be pure liquid Tabun as the change in growth factor with water activity is not available for many CWAs. It is also assumed that the coalescing Tabun does not change the density of the probe droplet. The same calculation has been performed for sarin, soman, cyclosarin, nitrogen mustard, sulphur mustard, VX, and lewisite and can be found in Appendix II.

3.6. THE LARA FITTING PROCESS

An assessment of the LARA fitting software was necessary to quantify the limitations which were made apparent by the Allan variance analysis. The LARA fitting software allows the live retrieval of droplet size and RI as a sampling measurement proceeds. It was established in section 3.4 that the optimal integration time should be of the order ~40 seconds to minimise the influence of environmental drift. The improvement in noise over

a period of 40 s (or longer) for retrieving the radius and RI suggests a considerably longer period of averaging is preferred, provided environmental drift can be minimised throughout the measurement. Indeed, in a previous report[56] an averaging time of 200 seconds was recommended based on standard deviations in droplet size and RI. This is consistent with the Allan variance deviations from section 3.4. It was recommended by Haddrell *et al.* that a period of averaging of 200 s gave standard deviations in the fitted size, n-RI and composition of ±1.0 nm, 0.0003 and 0.01 nm respectively.[94] We now consider an analysis method that relies on the raw observable, line centre of WGM's, rather than the inferred radius and RI to explore if improvements to sensitivity can be achieved.

The change in peak wavelength of a whispering gallery mode (WGM), $\delta\lambda$, from a reference wavelength λ can be used as a surrogate measure for the change in radius, δr, for a droplet from a reference radius a through Equation 3.11:

$$\frac{\delta\lambda}{\lambda} = \frac{\delta r}{r} \qquad \text{Equation 3.11}$$

Indeed, it is the wavelength shifts of the entire mode set that lead to the retrieved change in droplet radius from a full fitting of the Raman spectrum. A spectral shift in peak position of ~5 nm for a droplet of 3700 nm radius arises from a change in radius of ~28 nm. Although the trend in the wavelength of one resonant WGM is obvious, as seen in Figure 3.11(d), the change in size retrieved from fitting all WGMs while simultaneously retrieving RI and dispersion in RI is less apparent (c). The retrieval of radius has an uncertainty of

±2.2 nm, within the tolerance expected for fitting the WGM fingerprint,[81] equivalent to an uncertainty in the wavelength of a single mode of ~0.39 nm.

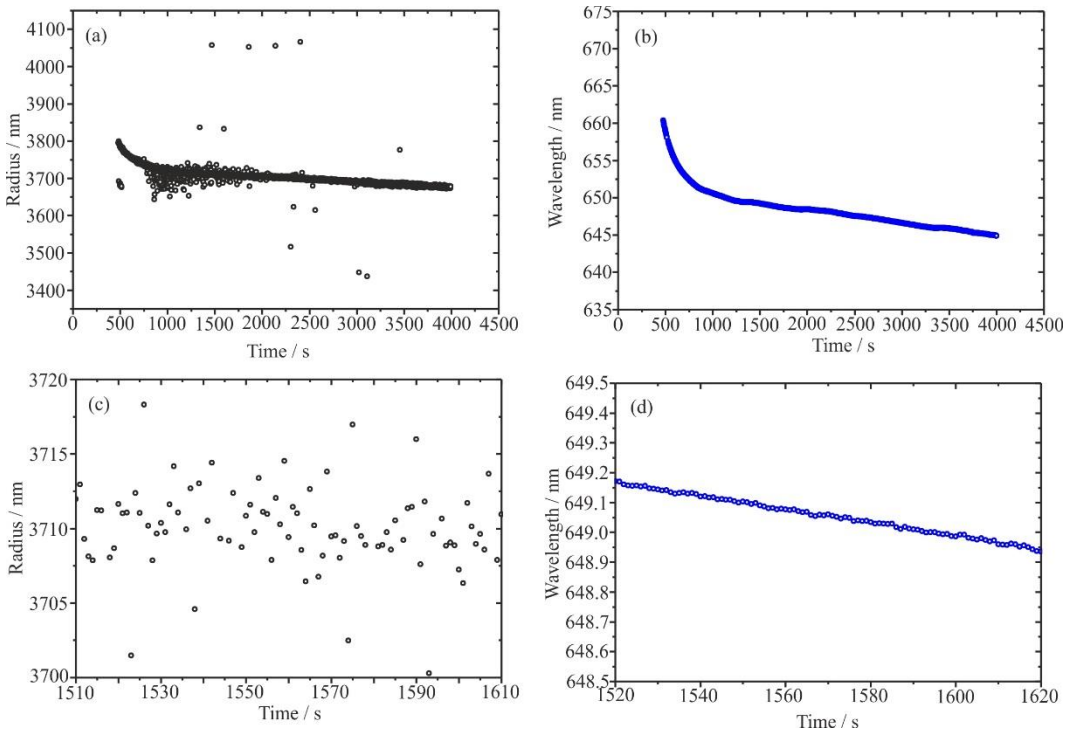

Figure 3.11: (a) Fitted radius over ~4000 s (b) Wavelength of the transverse electric first order (TE1) WGM over ~4000 s (c), (d) Fitted radius and WGM wavelength (respectively) from (a) and (b) over 100 s.

The measurement in Figure 3.12 illustrates how the Allan variance profile and the noise characteristics of the measurement can be dominated by the uncertainty in the fitting over a 100 s period. The seeming deterioration in the precision of the measurement when fitting the mode set compared to the clarity when examining one WGM arises from a multitude of factors. Uncertainty in the determination of the wavelength at the peak maximum of any one WGM from frame-to-frame of the measurement is particularly significant for modes in the wings of the Raman band where the signal-to-noise ratio may be low.[82] Some variation in the actual modes identified in the peak search may occur from frame-to-frame due to the low signal-to-noise associated with some modes. This can lead to a variation in the number and identity of modes fitted from frame-to-frame. The combination of these two factors can lead to variations in the assignments of the modes from frame-to-frame and consequently becomes 'noise' in the fitting of size and RI. However, it must also be recognised that the shift in wavelength of one WGM is not just a consequence of varying size but is also dependent on the change in RI, a fact that is not obvious from the approximate relation shown in Equation 3.11. The fitting errors for a set of trial solutions

(radius, RI, dispersion in RI) may be very similar with slight change in radius offset by an opposing change in RI. When all of these factors are accounted for, the resulting error landscape has many local minima and poor discrimination between these minima. The impact of the factors that contribute to the deterioration of the radius fit are highlighted in Figure 3.12.

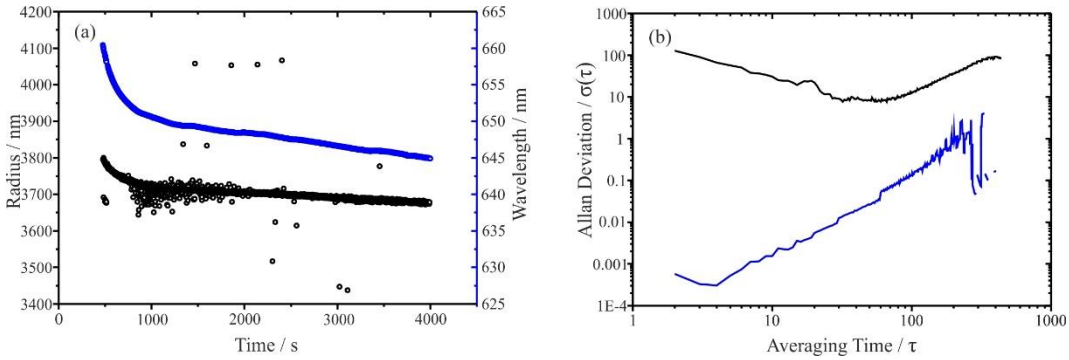

Figure 3.12: (a) Radius fitting (black) for a dataset over ~4000 s, left hand axis. Wavelength of the TE1 WGM (blue) for the same dataset over ~4000 s, right hand axis. (b) Allan variance analysis of the fitted radius (black) and TE1 Mode (blue).

A direct comparison of the data presented in Figure 3.11 with panel Figure 3.12(b) shows the corresponding Allan variance analysis. Very rapidly the Allan deviation in the wavelength measurement achieves a very low minimum in ~4 s of integration. Beyond this, the slow drift in size due to very small variations in environmental drift begins to degrade the measurement, reflecting how precise the actual measurement of wavelength is. Conversely, the noise incurred in fitting the mode set to get radius leads to significant noise and the spectra must be averaged for approaching 100 s before the accuracy in the size has improved sufficiently that the low frequency environmental drift in the measurement begins to dominate.

An exploration of possible metrics was necessary to improve sensitivity to change in droplet size and RI for the application this thesis is focussed on where simultaneously accurate measurements are required for very short time responses. This involves the calculations of two metrics from the WGM mode set, wavelength as a surrogate for the shift in droplet radius, and mode offset as a surrogate for shift in RI. For the RI the change in the relative position of the WGMs of different polarisation (transverse electric, TE, and transverse magnetic, TM) is a surrogate for shift in droplet RI.[60] The mode offset is the

spectral shift between relative wavelengths of three TE and TM modes as illustrated by Figure 3.13 and defined by Equation 3.12.

$$\text{Mode Offset} = \Delta\lambda 1 - \Delta\lambda 2 \qquad \text{Equation 3.12}$$

The objective here is to determine if the use of these surrogate measurements of size and RI are more appropriate than live fitting for the application of on-line CWA detection.

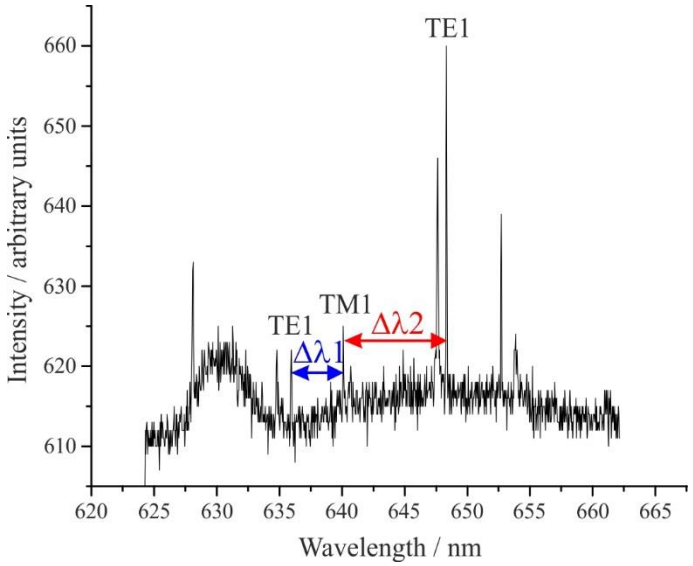

Figure 3.13: Visual depiction of the mode offset calculated from a typical Raman spectrum.

Figure 3.14 compares the accuracies of the droplet size, RI and dispersion determinations with the accuracies of the WGM wavelength and offset determinations. The clearest trend appears in the wavelength of a single WGM (b), consistent with previous discussions. Indeed, the change in wavelength of ~0.4 nm corresponds to a change in size (Equation 3.12) of 2.9 nm estimated with a precision of ± 0.39 nm from noise on the reported wavelength of 645 nm over a 10 second period, due to slow drift in environmental conditions. Note that the measurement of relative humidity (see Figure 3.14(f)) by the probe is far too inaccurate to perceive the drift that drives this change in size. Only the final significant shift in wavelength (surrogate for a change in size) leads to a perceptible change in the mode offset (d) which is concurrently observed for the retrieved RI. The retrieval of droplet radius (a) is less precise than the wavelength for the reasons described above. This

dispersion (fitted dependence of RI on wavelength) introduces an additional degree of flexibility to the fit.

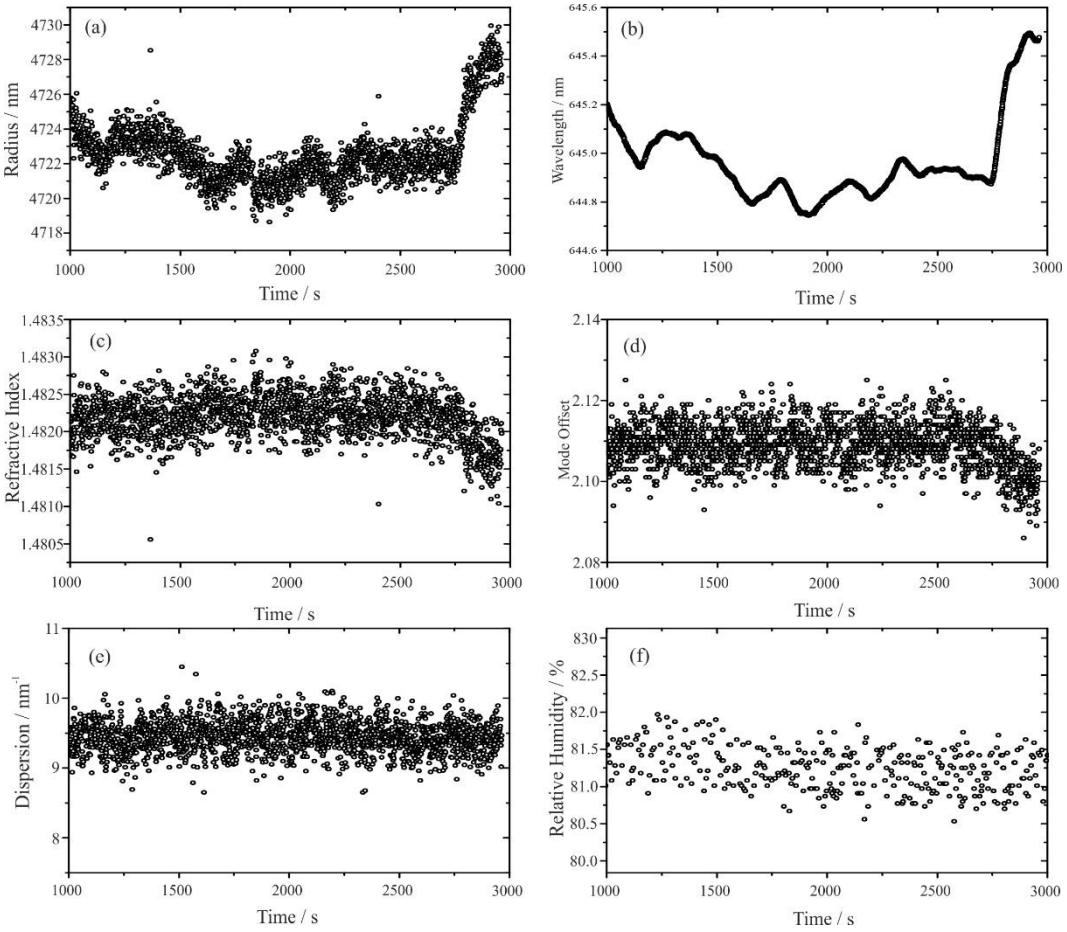

Figure 3.14: (a) Fitted radius over time. (b) TE1 wavelength over time. (c) Refractive index over time. (d) Mode offset over time. (e) Dispersion in RI over time. (f) Relative humidity over time.

Figure 3.15 compares the accuracy of the surrogate measurements (wavelength and mode offset) with the final retrieved RI and size. While it is clear that there is a correlation between wavelength and radius (Figure 3.15(d)), the change in mode offset with wavelength (b), signifying the expected change in RI with radius, is significantly less clear. This is entirely consistent with the smaller sensitivity of RI to variation in environmental conditions, such as evaporation or condensation, than radius. While the noise in radius is ~4 nm or 0.08 %, the change in RI associated with this change in size is only ~0.001 or 0.06 %. In fact, contrary to the only barely perceptible change in mode offset with wavelength, the RI does show a clear trend with radius. This indicates that although the fitting process does introduce noise to the retrieval of radius, the fitted radius and RI retrieved from an entire mode set (>4 modes) remain more sensitive to changes in droplet

size and composition than the simpler measurements of WGM wavelength and mode offset, which are based on only 1 and 3 modal wavelengths, respectively.

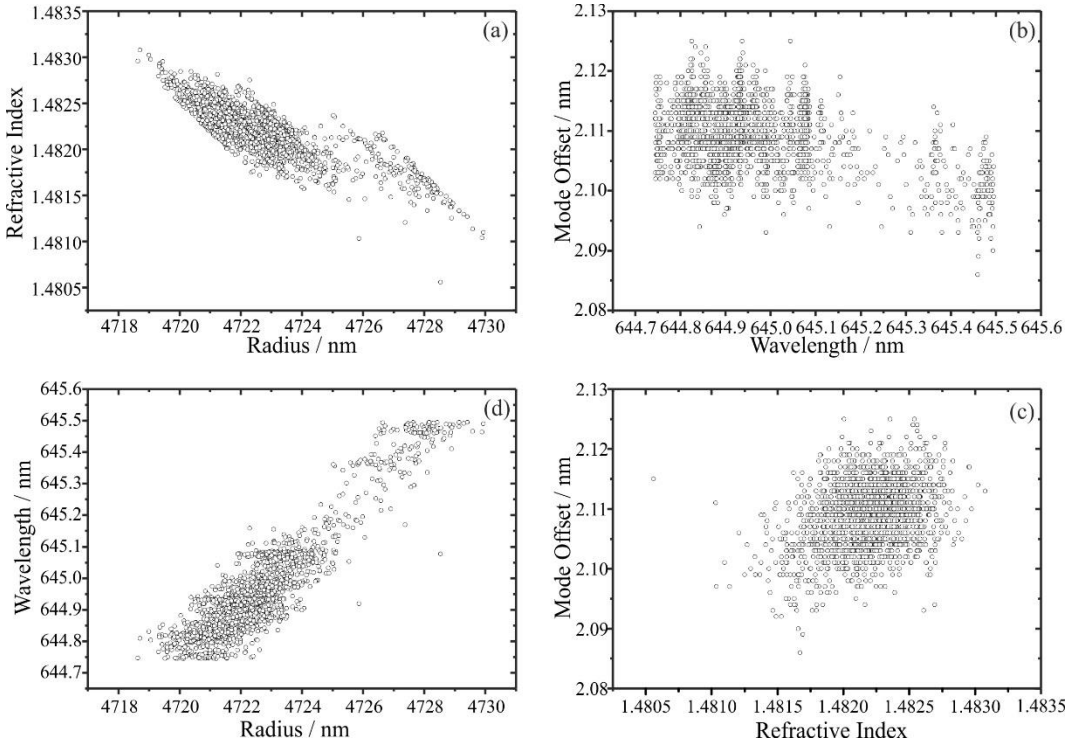

Figure 3.15: (a) Graph of the refractive index against radius. (b) Graph of the mode offset against the TE1 wavelength. (c) Graph of the TE1 wavelength against radius. (d) Graph of the mode offset against refractive index.

In a final assessment of the noise associated with the retrieval of radius and RI two limiting cases were explored from one dataset. In Figure 3.16 a droplet is considered which is

changing rapidly in size due to environmental drift over a period of 150 s, from here on referred to as the *steep case* in RH variation.

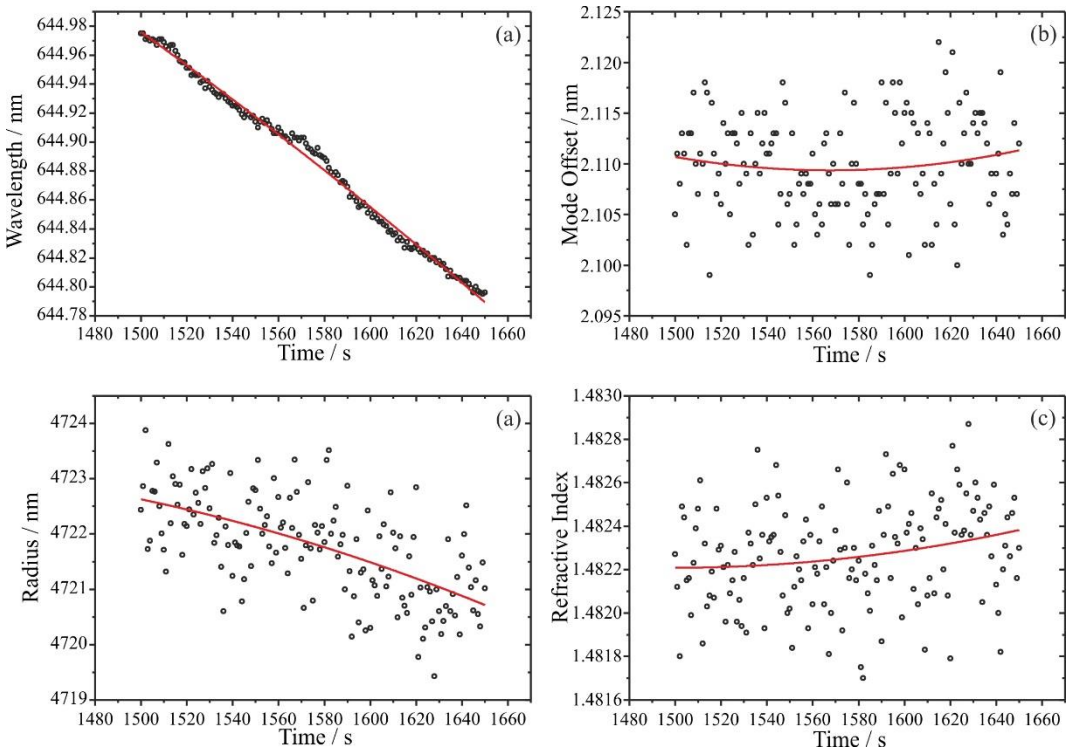

Figure 3.16: (a) A graph of the TE1 mode wavelength decreasing over 150 seconds (black dots) and a polynomial fit (red line), (b) mode offset, (c) radius, (d) refractive index.

In Figure 3.17 the same droplet is considered over a further period of 150 s but when the environmental conditions were relatively stable, from here on referred to as the *flat case*.

In both cases, the noise is considered around a mean polynomial fitted trend line for all observables.

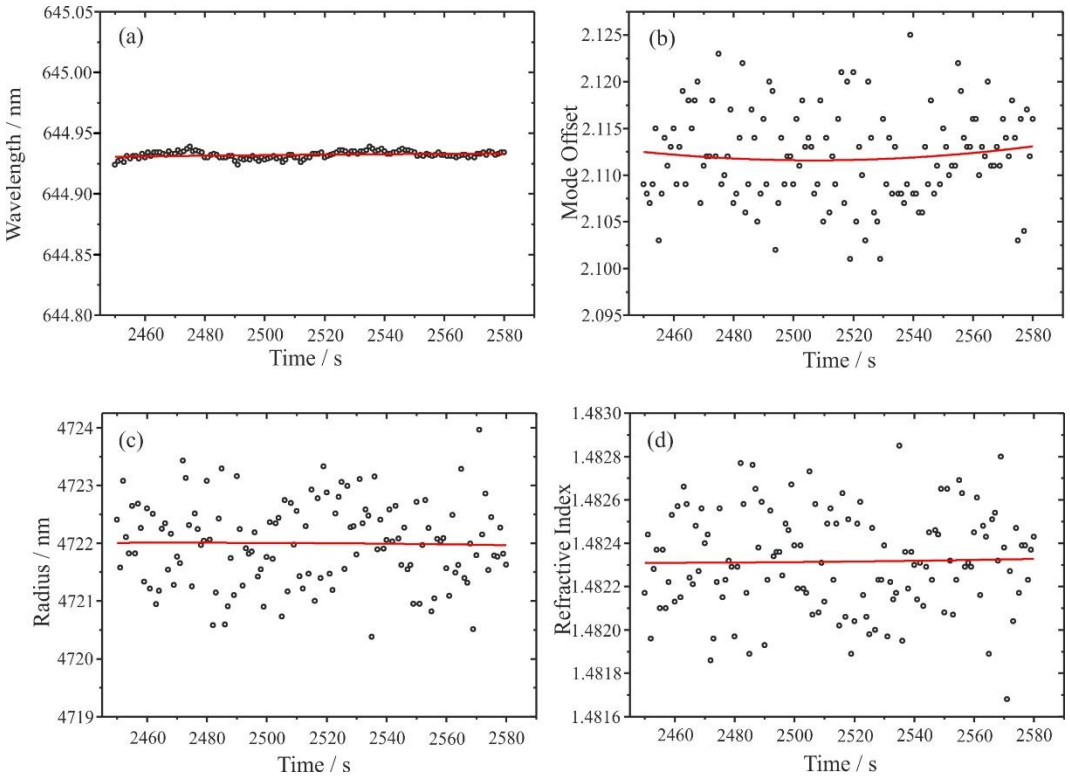

Figure 3.17: (a) A graph of the TE1 mode wavelength oscillating over 150 seconds (black dots) and a polynomial fit (red line), (b) mode offset, (c) radius, (d) refractive index.

As previously discussed, although the wavelength measurement of one WGM is extremely precise, the level of associated change in RI is rather imprecisely quantified by the mode offset. The retrievals of radius and RI are rather similarly imprecise. The standard deviations about the fit lines for each quantity relative to the actual value of the quantity (e.g. σ_λ/λ) are reported in Table 3.3.

Table 3.3: Normalised residual means about a polynomial fit for parameters radius, RI, mode offset and wavelength in two different case studies, steep and flat.

Parameter	Steep Case	Flat Case
Wavelength	5.39E-06	3.51E-06
Mode Offset	1.84E-03	1.89E-03
Radius	1.21E-04	1.22E-04
Refractive Index	1.24E-04	1.25E-04

For both cases, the wavelength is precisely determined, and the mode offset is much less well determined. Significantly, once the full mode set is fitted and radius and RI retrieved, the level of precision achieved for both inferred quantities is comparable and intermediate

between wavelength and mode offset. This reinforces the conclusion that performing the fitting of the WGM mode set remains the most appropriate methodology to assess the changes in composition of a sampling droplet.

3.7. SPECTROGRAPHIC NOISE

The measurement of light intensity scattered by the probe droplet is recorded as a voltage using a charge coupled device (CCD). The recorded voltage can be easily analysed by computer processing. However, there is an inherent level of noise in the output from a CCD. The noise in the measurement is due to the uncertainty in photon counting and the process of converting light intensity to an electrical output. There are two sources of noise which arise from the use of a CCD, they are classified as temporal and spatial.[95] Spatial noise is the result of discrepancies across the pixels in the CCD chip. Nonuniformity across the pixels can be removed using a computer algorithm which applies a flatfield correction to the signal. The Raman spectrograph and CCD used in this work utilises a flatfield correction, therefore the spatial noise can be disregarded.

This work focuses primarily on the temporal noise. Temporal noise is made up of the shot, readout and dark noises. These types of noise are all consequences of the way charge moves through a system and of the process of amplifying the output from the CCD. The shot noise, n_S, is the random noise due to stray photons arriving on the CCD chip. The noise which is due to the changes in dark current produced in the CCD is known as the dark noise, n_D. The dark noise is dependent on the CCD temperature (- 75 °C) and integration time (1-100 s). The noise which occurs under conditions of complete darkness is known as the readout noise, n_R, in other words it is the baseline noise of the CCD without exposure to light. The readout noise is instrument specific, determined by the manufacturer, and is not affected by the level of the signal.

This section addresses each of the three types of temporal noise, calculates values of noise present in a Raman spectrum. The number of electrons which reached the CCD, N_e, was calculated using Equation 3.13 where K is the gain constant and describes the number of electrons per analogue to digital conversion (ADC) unit.

$$N_e = (output\ intensity - DC\ offset) \times bin \times K \qquad \text{Equation 3.13}$$

The CCD used (Pixis 256 E) had a DC offset of 611 intensity counts, and the bin (number of pixels binned vertically) was 226. This means that the CCD is modelled as a 1-dimensional detector of 1024 columns of pixels. The gain constant, K, is 3 e^-/count. It can be seen in Figure 3.18 that the recorded number of output intensity counts at the baseline

was 630 ADU, which corresponds to a N_e of approximately 14080 e^-. The recorded number of output intensity counts at a peak of sucrose was 725 ADU which corresponds to a N_e of approximately 87040 e^-.

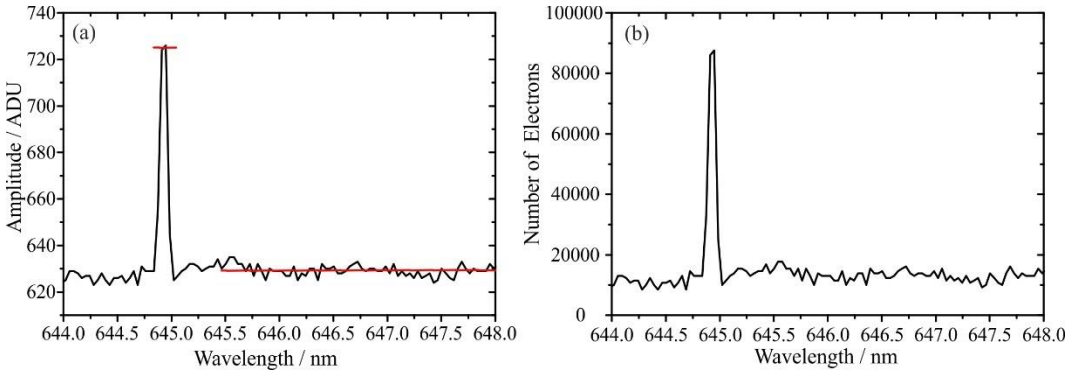

Figure 3.18: A figure showing the amplitude of the TE1 peak of a 0.8 aW sucrose droplet held at 80 % RH. The amplitude in figure (a) is shown in analogue digital unit (ADU), and the same peak is shown as number of electrons in figure (b).

Now that the number of electrons in the signal has been defined, the signal to noise ratio can be calculated. The S/N ratio can be calculated using Equation 3.14, in which σ_S is the root mean squared (RMS) of the shot noise, σ_D, is the RMS of the dark noise and σ_R is the RMS of the readout noise.

$$\frac{S}{N} = \frac{S}{\sqrt{\sigma_s^2 + \sigma_D^2 + \sigma_R^2}} \qquad \text{Equation 3.14}$$

The RMS of the dark noise was taken from the Princeton Instruments S/N calculator,[96] was 0.003 e^-/pixel/s at a temperature of – 75 ˚C. The dark current was 0.768 e^-column when the exposure time was 1 second, over 256 pixels binned per 1 data pixel. The root mean square of the electrons from readout noise in the system is 6 e^-. The noise contribution from the

shot noise is calculated using an assumption of Poisson statistics of electrical charge generation using Equation 3.15. In Equation 3.15 n_s is the number of electrons in the signal.

$$\sigma_s = \sqrt{\langle n_s \rangle} \qquad \text{Equation 3.15}$$

The values of noise of each different type have been summarised in Table 3.4.

Table 3.4: A table of the RMS values of noise for the PIXIS 265E CCD.

Noise Type	**RMS / e^-**
Dark Noise	0.768
Readout Noise	6
Shot Noise at Baseline	295
Shot noise at Peak	119

The total value of noise can be calculated using Equation 3.16.The total value of noise at the baseline is approximately 119 e^-, and at the total noise at peak is approximately 295 e^-. For the CCD used 1 ADC unit of 265 pixels corresponds to 768 e^-. For both the baseline, and peak case, the total value of noise is lower than the electrons required to create an ADU. This means that the digital signal generated using the LARA Processing software, presents the most substantial contribution to the noise in the signal for an exposure time of 1 second and a CCD temperature of -75 ˚C.

$$\sigma_i = \sqrt{\sigma_D^2 + \sigma_R^2 + \sigma_s^2} \qquad \text{Equation 3.16}$$

If the detection limit is S/N = 4.1 the number of electrons which are detected by the CCD must exceed 4.1 ADC units (2304 e^-). This number of electrons is equivalent to 2.6 % of the signal of a 1M solution of sucrose. The lowest concentration of sucrose which could be

detected with a spectrographic signal to noise ratio of 4.1 would have a molarity of 0.026 M if the digital fitting introduced no contribution to noise.

An experiment was conducted in which a series of sodium nitrate droplets were trapped using OT1. The sodium nitrate droplets had molarities of 3.5 M, 5.9 M, and 8.2 M. Figure 3.19 shows the Raman spectrum recorded with an integration time of 1 frame per second.

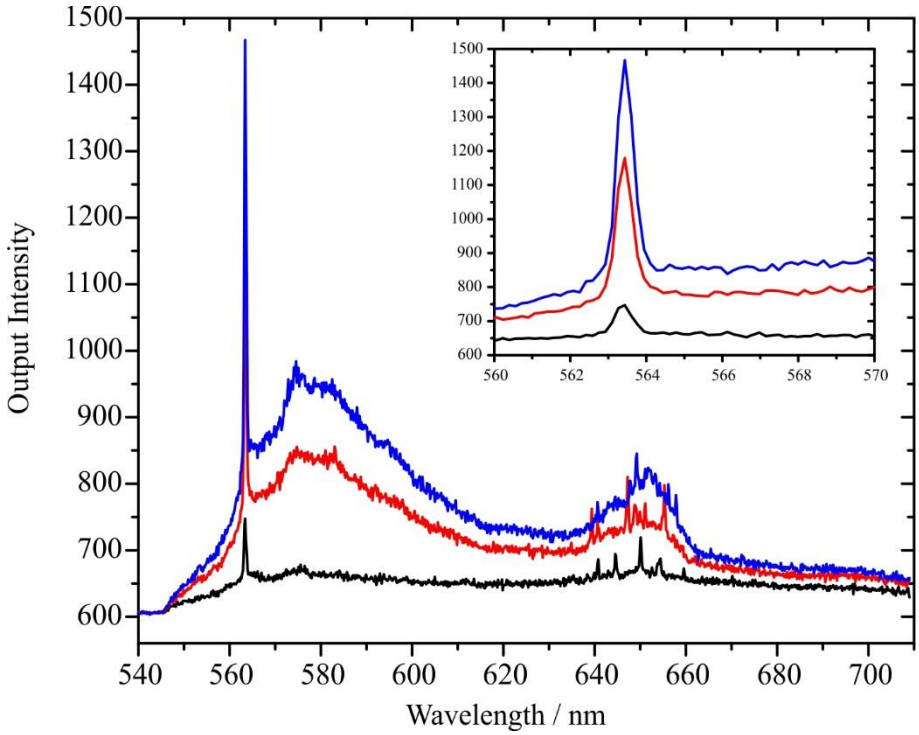

Figure 3.19: A graph showing the Raman spectrum of three sodium nitrate droplets with a molarity of: 3.5M black line, 5.9 M red line, 8.2M blue line.

It is evident that as the concentration of the droplet is increased the peak intensity increased from 746 to 1177 to 1465 intensity counts for the 3.5M, 5.9M and 8.2M concentration droplets respectively.

The integration time was increased from 1 to 10 to 100 seconds for each of the concentrations of sodium nitrate droplets, the results for the 5.9M case are shown in Figure

3.20. The peak intensity increases as integration time increases, similarly the signal to noise ratio increases as the signal becomes stronger in relation to the background noise.

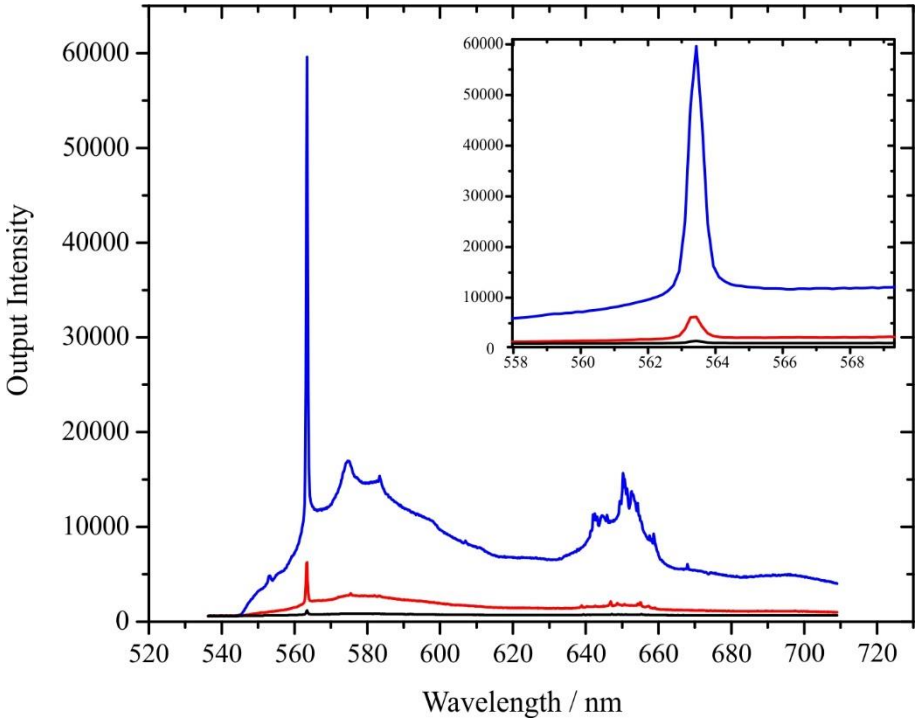

Figure 3.20: A graph showing the Raman spectrum of one sodium nitrate droplets with a molarity of 5.9 M red line. The black line has an integration time of 1 frame per second, red line: 10 fps; blue line: 100 fps.

The full results are summarised in Table 3.5. It can be seen that the signal to noise ratio is highest for the 5.9M sodium nitrate droplet with an integration time of 100 seconds per frame.

Table 3.5: A table showing the variation in peak and baseline intensity, and the signal to noise ratio with integration time and droplet molarity.

Molarity	Integration Time / s	Peak Intensity	Baseline Intensity	Peak to Baseline Ratio
3.5	1	746	659	1.13
3.5	10	2008	1316	1.53
3.5	100	31344	30611	1.02
5.9	1	1177	784	1.50
5.9	10	6251	2287	2.73
5.9	100	59622	11933	4.99
8.2	1	1465	861	1.70
8.2	10	9852	1992	4.95
8.2	100	1594	890	1.79

Although the inherent spectrographic noise is not the main source of noise in the data fitted, or recorded from an optical tweezer experiment, it is still significant to understand. Increasing the integration time of the system will result in an increase in the shot and dark noise contributions, but the total readout noise will reduce as the signal is only 'read out' one time. This can be seen as when the integration time was increased the signal to noise ratio increased. However, at a longer period of integration the contributions from the shot and dark noise will dominate the signal and begin to degrade the signal to noise ratio.

3.8. IDEAL PROBE DROPLET SIZE

For an assessment of the noise characteristics of the AOT it is important to understand the impact of droplet size on spectral features. The AOT can used to trap droplets between 3 –

7 μm in radius, Figure 3.21 shows a comparison of the Raman spectra for droplets of varying size.

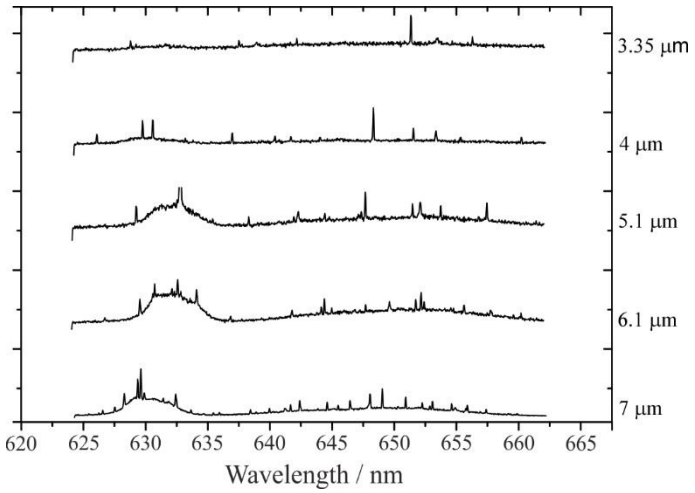

Figure 3.21: Typical spectra from aqueous sucrose droplets spanning the radius range 3.35 to 7 μm. The increasing number of modes and reduced mode spacing is indicative of the increasing size, as is the increase in the C-H and O-H Raman band intensities.

Previous work[97] has suggested that working with smaller sample droplets is ideal for improving the sensitivity of the coalescence sampling with the same amount of accreted mass leading to a larger fractional change in size and RI when the sample droplet is smaller. Counter to this, it must also be considered that the determination of size and RI is, in principle, more accurate for larger droplets. The Raman spectra of larger droplets have more modes of a higher peak intensity to fit with a narrower linewidth, consistent with a sensitivity that would improve with increasing size. Therefore, the ideal probe droplet size for detection of CWA must be a compromise between two conversely limiting factors, the relative advantages in reduction in noise which comes from fitting larger droplets with enhanced spectral features, and the desire to detect lower concentrations of CWA by using a smaller probe droplet.

Table of the mass of CWA required to give specified change in particle RI at 80% RH / g (Taken from DSTL Deliverable report)

Change in Probe Droplet Radius / nm	**Mass of CWA Required to Change Probe droplet with an Initial Radius of 4000 nm / g**	**Mass of CWA Required to Change Probe droplet with an Initial Radius of 5000 nm / g**
2	4.71×10^{-13}	7.36×10^{-13}
3	7.07×10^{-13}	1.1×10^{-12}
5	1.18×10^{-12}	1.84×10^{-12}

Based on the Allan variance analysis it is recommended that the idea probe droplet size is between 4 and 5 micrometres in radius. This droplet size range balances two limiting

factors to CWA detection. The lower limit on CWA detection is the poor signal achieved with very small droplets, the fewer WGMs of a lower intensity introduce a large noise component to the fitted radius and RI. The upper limit to CWA detection is the volume of sample required to make a significant change to the probe droplet properties increases as the probe droplet size increases. Put differently the larger the probe droplet, the higher concentrations of CWA need to be added for detection. Based on these factors a probe droplet radius range between 4 – 5 micrometres is recommended for CWA detection.

3.8.1. DEMONSTRATING THE INFLUENCE OF INTEGRATION TIME

It was concluded that a time integration of ~40 seconds is optimal from the Allan variance analysis, and that droplet sizes of 4 – 5 μm should be used to detect CWAs. Figure 3.22 illustrates the clear improvement in the signal-to-noise ratio that is achieved as the integration time increases, leading to more well-defined WGM lineshapes and improved spontaneous Raman band intensities.

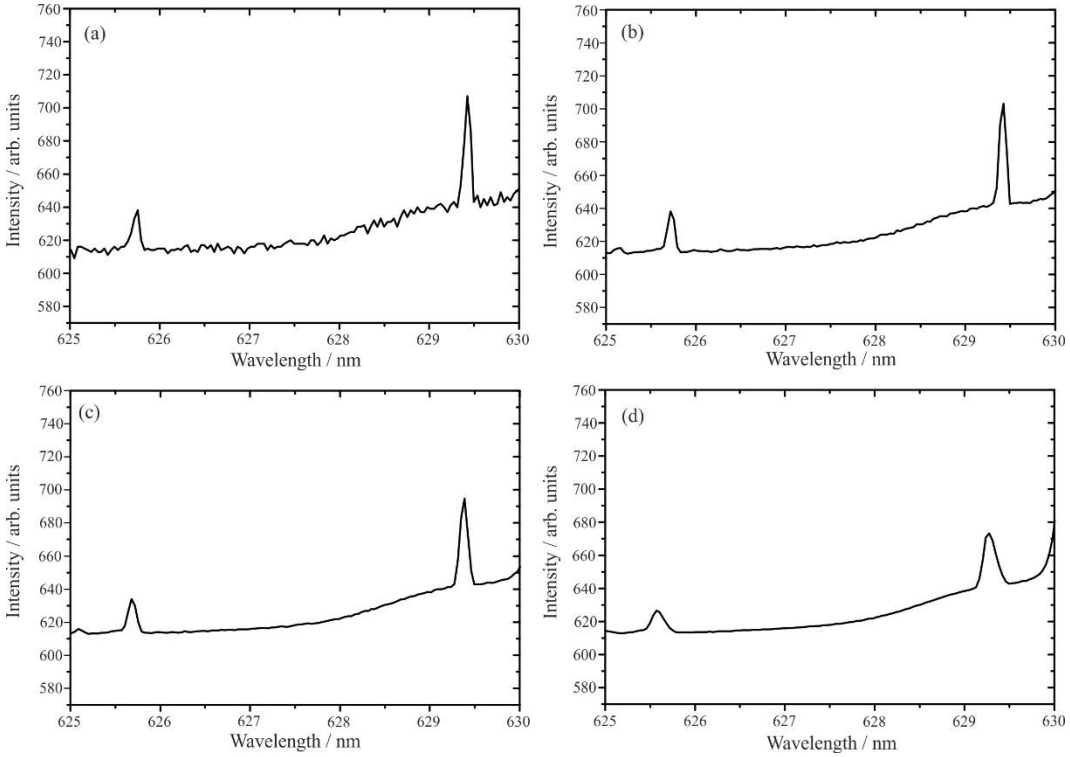

Figure 3.22: Raman spectra between 625 – 630 nm that have been averaged for (a) 1 second, (b) 5 seconds, (c) 20 seconds, (d) 40 seconds.

However, in Figure 3.23 it is shown that as the integration time increases, the drift in environmental conditions leads to shifts in the WGM wavelengths that are manifested as a

broadening of the WGM lineshape, leading to a deterioration in the accuracy with which the radius and RI can be determined.

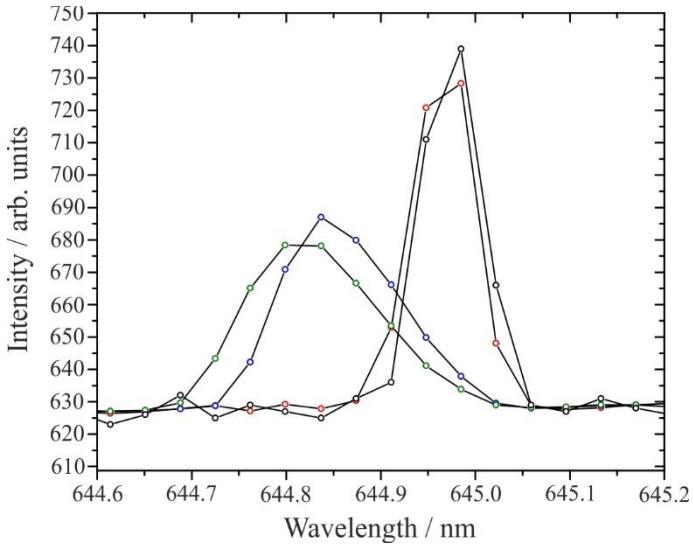

Figure 3.23: Raman spectra of a single whispering gallery mode between 644 – 645 nm. 2 nm that have been averaged for periods of 1 second (black), 20 seconds (red), 300 seconds (blue), 400 seconds (green).

3.9. CONCLUSIONS

An Allan variance approach is a powerful tool for assessing the noise characteristics of a dataset. However, the noise characteristics of AOT datasets are the result of a series of processes, each introducing a new component of noise. For such a complex technique the main sources of noise have been identified and characterised. It is beneficial to identify which processes have a significant impact on a dataset. First is the stability of the environmental conditions surrounding a trapped droplet; when these conditions change a low frequency noise component is added to the dataset. Low frequency noise components were resolvable after at least 70 seconds of data acquisition and are due to changes in the surrounding RH and temperature. In order to perform accurate measurements of CWA uptake it is vital to stabilise the environment surrounding the droplet as much as possible, finely controlling RH and temperature. This can be done by optimizing the cell and gas delivery systems.

The second component which will affect the noise in a dataset is the process of recording spectra. The recording of voltage from photons landing on the CCD is subject to temporal noises, (shot, readout and dark noises). These noise components make up a few hundred electrons per Raman signal and do not present a significant amount of noise in the spectra. It is favourable to record spectra over several seconds to reduce the noise introduced during

the analogue to digital conversion process. It is suggested that the integration time of 40 seconds determined by the Allan variance is achieved by increasing the exposure time per spectrum.

The third is the method through which the radius and refractive index are retrieved. An investigation into the possible metrics for retrieving droplet size and RI was considered. The current method of determining droplet size and RI is the use of the LARA fitting program. It was found that although the wavelength of the WGM was a good proxy for droplet size, the mode offset was insufficient as a proxy for reporting the refractive index. It is recommended that the LARA software is the most effective method of determining droplet radius and refractive index.

The detailed noise analysis has determined that the ideal probe droplet size is between 4 to 5 μm and the optimal integration time for the radius and RI is ~40 seconds. This process can be easily replicated on other AOT instruments and can be used to directly compare the noise performance of an instrument.

4. Accretion

4.1. Introduction to Accretion

Accretion is defined as the growth or increase of a boundary layer by the gradual accumulation of additional layers of matter. In this project, accretion is defined as a series of discrete coalescence events between an ensemble of fine mode aerosol and a coarse mode probe droplet. In the experiments described in this chapter, accretion occurs through the process of passing a plume of aerosol over a trapped picolitre droplet. From this point, the trapped droplet will be referred to as the droplet and the plume of aerosol will be referred to as the aerosol.

4.2. Experimental Setup

There are several factors which must be controlled when the aerosol is passed through an aerosol optical tweezers (AOT) trapping cell: the relative humidity (RH) of all components (the gas phase, cell environment and aerosol); the water activity, a_w, of the droplet and aerosol; the gas flow rate; the aerosol flow rate; and the mass concentration of aerosol particles in the gas flow. The nature of passing aerosol through a closed system presents a set of unique challenges, and some potential solutions were explored throughout this chapter. For example, valves and delivery pipes became blocked due to a build-up of salts from the deposition of aerosol particles.

The experimental setup of the optical tweezers experiment has already been described in Chapter 2 Figure 2.9. This chapter deals only with alterations to the gas flow lines. Figure 4.6 displays a diagram of the first gas and aerosol experimental layout used. Throughout this chapter, the layout of the system was modified and optimised, utilizing different optical tweezers (OT1, OT2), cell inlet orientations (axial, radial), flow rate control techniques and aerosol ensemble measurement instruments. Each design shed new light on the complex problems that must be addressed when sampling aerosol *via* coalescence with an optically

trapped droplet. In the following sections, key features of the accretion experiments will be discussed individually.

4.2.1. THE ATOMIZER: A SOURCE OF AEROSOL

The atomizer used in this experiment was the TSI model constant output atomizer. There are two configurations which can be used to deliver solution to the atomizer, recirculation and non-recirculation mode. In recirculation mode, the atomizer draws solution and expels excess solution into the same vessel. The concentration of the excess solution may not be equal to the initial concentration, this can introduce a drift in the concentration of the atomized aerosol over time. Used in non-recirculation mode, there is no drift in atomized aerosol concentration over time. Figure 4.1 shows a diagram of the process of atomization and a diagram of non-recirculation mode.

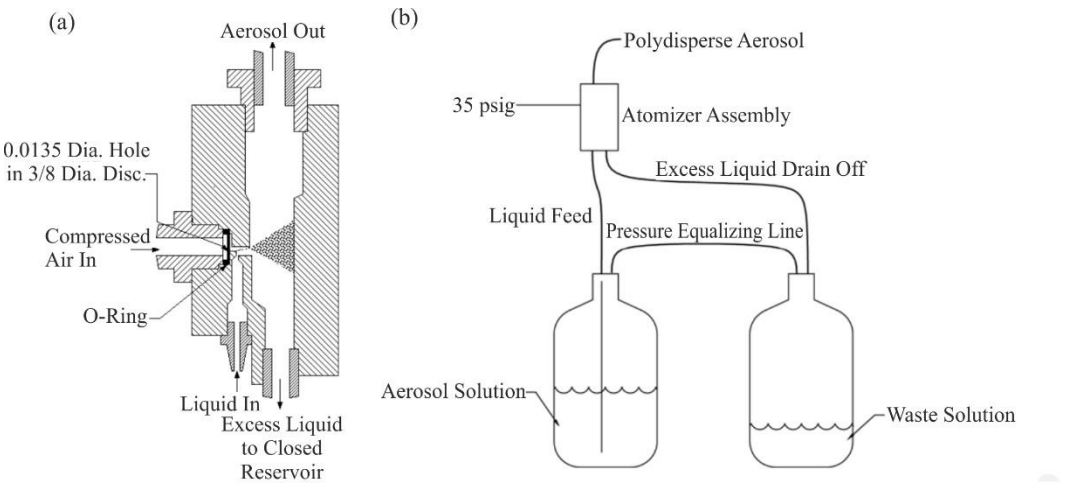

Figure 4.1: A schematic of the operation of an atomizer. (a) a diagram of the atomizer assembly block (b) Atomizer configured in the non-recirculation mode with an extra bottle. Adapted from TSI Atomizer Manual.

The inlet pressure of the gas flow supplying the atomizer directly influences the flow rate of the atomized aerosol. At the initial stages of measurement there was not an available mass flow controller with an operating capacity of > 2 L / min to regulate the atomizer flow rate. The output size distribution of the atomizer was recorded and is presented in **Figure**

4.2. Panels (a) and (b) show the size distribution of the atomizer. The atomizer was loaded with a 0.8 water activity solution of sodium chloride.

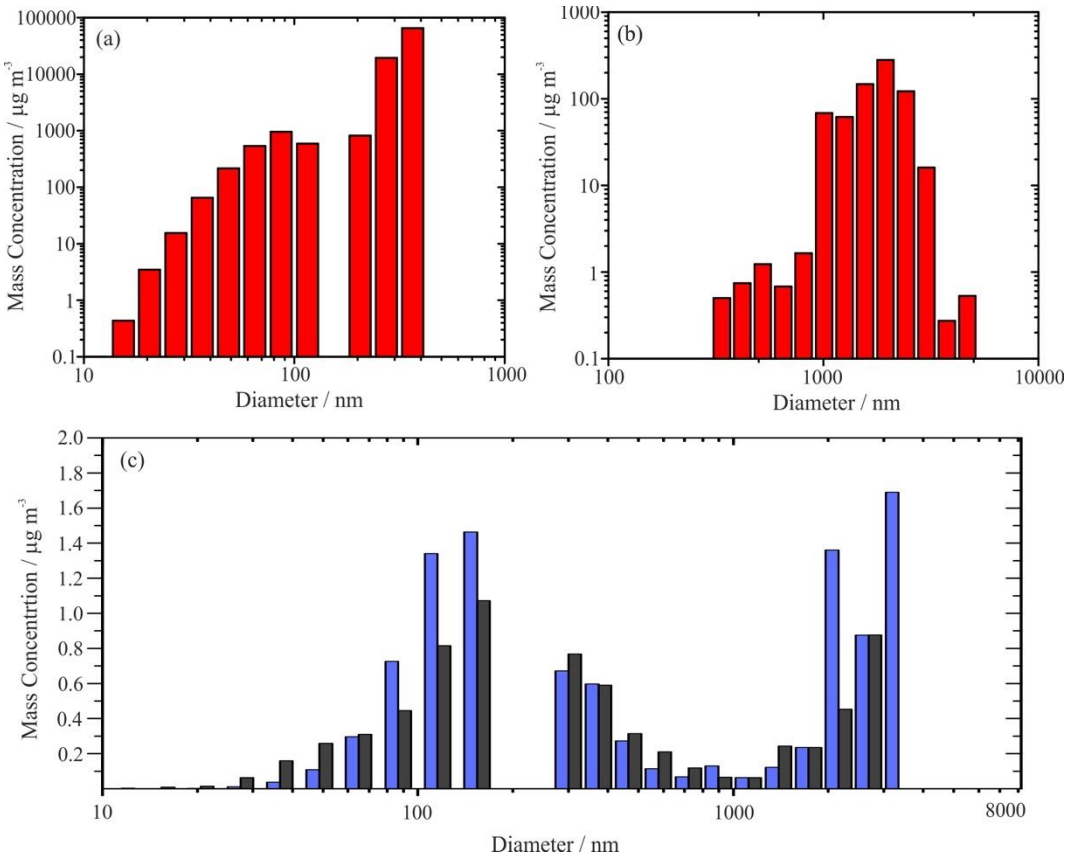

Figure 4.2: (a) Mass concentration against diameter taken on the Nanoscan, from 0 to 300 nm. (b) Mass concentration against diameter taken on the OPS in the region of 300 nm to 5000 nm. In the atomizer was a 0.8 water activity, aqueous sodium chloride solution. (c) An example of the mass concentrations of aerosol in the lab during the working day, blue bars, and after the working day (5:30 pm), grey bars. This data was taken on both the OPS and NanoScan and combined using the Aerosol Instrument Manager software.

Panel (c) of Figure 4.2 shows the background concentrations of aerosol in the laboratory during the working day (blue bars) and after 5 pm (grey bars). The mass concentration of aerosol is much lower in the laboratory than the output from the atomizer. The mass concentration of aerosol after the working day is lower in the laboratory as experiments have ceased. Panel (c) of Figure 4.2 is also included to demonstrate that it is possible to combine the data from the optical particle sizer (OPS) and the NanoScan for a complete representation of aerosol size distribution.

4.2.2. MASS FLOW CONTROL

The flow of gas was controlled using a series of digital and analogue mass flow controllers (MFCs) (Bronkhorst). The flow of aerosol was controlled using positive pressure delivered

through MFCs and needle valves. It is not possible to directly pass aerosol through an MFC, and this presented a significant challenge to the design of the accretion system.

4.3. PARTICLE SIZING AND COUNTING

Two instruments, an optical particle sizer (OPS) (TSI Model 3330) and a NanoScan scanning mobility particle sizer (SMPS) (TSI Model 3190) were used in this experiment to record particle size distribution, number concentration and mass concentration of aerosol. The OPS has a size range of 0.3 – 10 μm with a size resolution of < 5 % at 0.5 μm. The OPS can sample aerosol particles up to a maximum number concentration of 3000 particles / cm^3.[98] The NanoScan can sample particles from 10 nm – 300 nm, with maximum concentrations up to 1,000,000 particles / cm^3.[99]

4.3.1. OPTICAL PARTICLE SIZER (OPS)

A schematic of the internal operation of the OPS is shown in Figure 4.3. The OPS pump draws the aerosol sample in at a rate of 1 L/min. From here, it is passed through a laser beam, the scattered light is reflected by an elliptical mirror towards a photodetector. The sample is then collected in a gravimetric filter, with opportunities for further offline sample analysis. From the collection of single particle light scattering, the photodetector records the intensity of light. The recorded light intensity is then used to determine the particle size, placing it within one of the size bins. The cumulative measurements of light intensity, as a proxy for particle size, yields a size distribution of an aerosol ensemble over a set period of time. In off-line analysis, using the Aerosol Instrument Manager software, the OPS data can be converted to mass, number, volume and surface area distributions of an aerosol ensemble. The OPS can detect particles with diameters between 0.3 – 10 μm. The OPS can only detect particles with sufficiently large optical cross sections, which therefore scatter

enough light, in order to collect sufficient light intensity for a measurement. The lower limit of this size range, 0.3 μm, was found to be too large for this work.

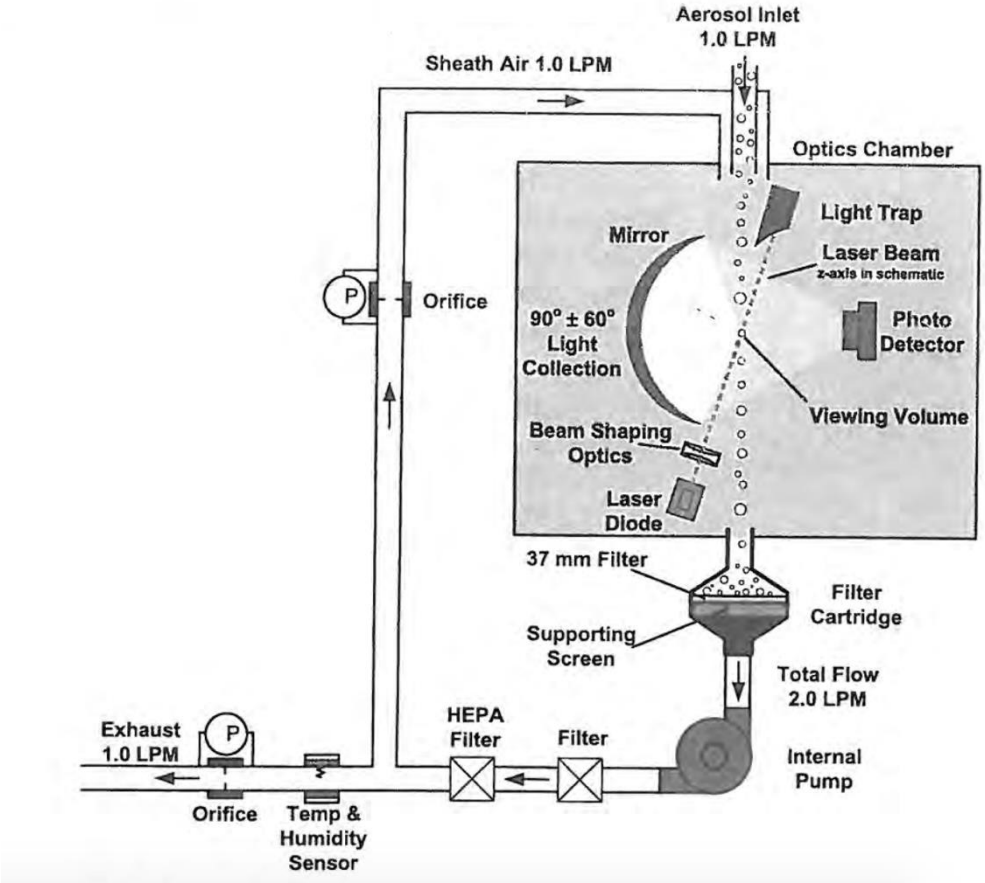

Figure 4.3: A schematic of the optical particle sizer. Taken from TSI.[98]

When more than 3000 particles pass through the laser beam per minute the pulses of scattered light recorded by the photo detector start to overlap one another, and the system becomes saturated. Above this concentration limit the instrument is unable to record the mass, number and surface area concentration.

4.3.2. NANOSCAN SCANNING PARTICLE MOBILITY SPECTROMETER (SMPS)

The NanoScan instrument is comprised of a radial differential mobility analyser (DMA) and a condensation particle counter (CPC). A schematic of the internal operation is shown in Figure 4.4. First the particles are passed through a cyclone. The cyclone removes larger particles that can hinder instrument performance by clogging the system. Larger particles can have multiple charges. Multiple charges per particle can lead to particles with different diameters exhibiting the same electrical mobility, thus degrading instrument resolution.

Next, the particles are charged when exposed to an ion source which imparts the particles with a charge.

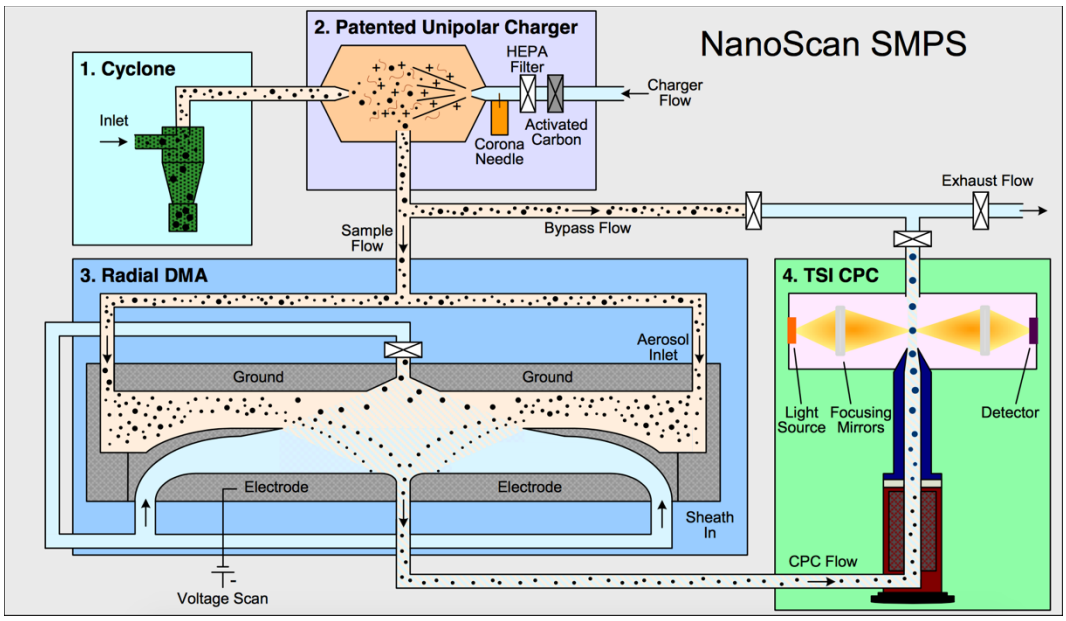

Figure 4.4: A schematic of the NanoScan. Taken from TSI.[99]

The charged particles are then passed through a radial DMA, which categorises particles according to their mobility in an electrical field, $F_{electric}$. Electrical mobility, Z_p, is defined by Equation 4.4 and quantifies the ability of a particle suspended within a gas medium to traverse an electric field.[100] The particle also experiences drag from the gas flow, $F_{viscous\ drag}$, this is derived from Stokes law. When the force of the electrical field is balanced against the oppositional drag force, the electrical mobility of the particle can be calculated. In Equation 4.1, n_p is the number of charges per particle, e, is the elementary unit of charge,

E is the electric field strength, μ is the viscosity of the gas, D_p is the particle diameter, C is the Cunningham slip correction and ν is the velocity of the particle.

$$F_{electric} = n_p e\, E \quad \text{Equation 4.1}$$

$$F_{viscous\ drag} = \frac{3\pi\mu D_p \nu}{C} \quad \text{Equation 4.2}$$

$$F_{electric} = F_{viscous\ drag} \quad \text{Equation 4.3}$$

$$Z_p = \frac{\nu}{E} = \frac{n_p e C}{3\pi\mu D_p} \quad \text{Equation 4.4}$$

The NanoScan was operated using the scan mode, where the particle size distribution is measured by ramping the voltage of the electrode quickly (increased over 45 seconds, decreased for the remaining 15 seconds) to record all mobility diameters. In the initial 45 second period the CPC continually measures particle concentration, in the last 15 seconds no particle concentration data is recorded.

The CPC is situated downstream of the DMA. A CPC works in a similar fashion to an optical particle sizer in that it uses a laser and a photodetector to record the number of particles passed through a laser beam. However, at small particle size ranges (<300 nm) an OPS is unreliable in particle sizing and counting. A CPC exposes the aerosol to isopropyl alcohol (IPA) vapour, which condenses onto the particles, growing the particle size to a detectable level. Larger particles scatter more light and are easier to detect in an optical particle detector.

Both the OPS and the NanoScan were used in this work. It was concluded that the NanoScan, with access to the lower size ranges and a higher maximum concentration was more applicable to the lab-based accretion measurements performed in this chapter.

4.3.3. CALCULATING DRY MASS OF A PARTICLE

The dry mass of the probe droplet is equal to the mass of the solute in the probe droplet, in this case NaCl. Similarly, the wet mass of the particle is thought of as the mass of the solute and solvent. The dry mass was calculated using the radius, refractive index, and dispersion in the refractive index which were fitted using the LARA analysis program. First the volume, V, of the droplet is calculated (Equation 4.5). Then the refractive index at 589 nm

is calculated, RI_{des}, using the RI collected at 650 nm, RI_{coll}, and the two dispersion terms D1 and D2 (Equation 4.6).

$$V = \left(\frac{4}{3}\right) \times \pi \times r^3 \quad \text{Equation 4.5}$$

$$RI_{des} = RI_{coll} + D1 \times \left(\frac{1}{\lambda_{des}} - \frac{1}{\lambda_{coll}}\right) + D2 \times \left(\frac{1}{\lambda_{des}} - \frac{1}{\lambda_{coll}}\right)^2 \quad \text{Equation 4.6}$$

Next the mass fraction of solute (MFS) is estimated from the density and refractive index at 589 nm. The refractive index of a droplet changes as it becomes a more concentrated solution, either through accretion of mass or evaporation of water.[101] The variation in RI with MFS can be accounted for by the application of the molar refraction mixing rule.[102] The molar refraction mixing rule has been validated as the most accurate mixing rule for inorganic and organic aqueous systems.[103] The refractive index of a droplet of pure water is 1.333, the refractive index of a droplet of pure sodium chloride is assumed to be the melt refractive index of bulk phase sodium chloride, 1.5729.[88,104] The E-AIM model III was used to generate a parameterisation for the RI, MFS and density of a particle, shown in **Figure 4.5**. The MFS of the particle is then assigned from the fitted RI of the particle at 589 nm. Then the density of the particle is assigned from the associated value of MFS.

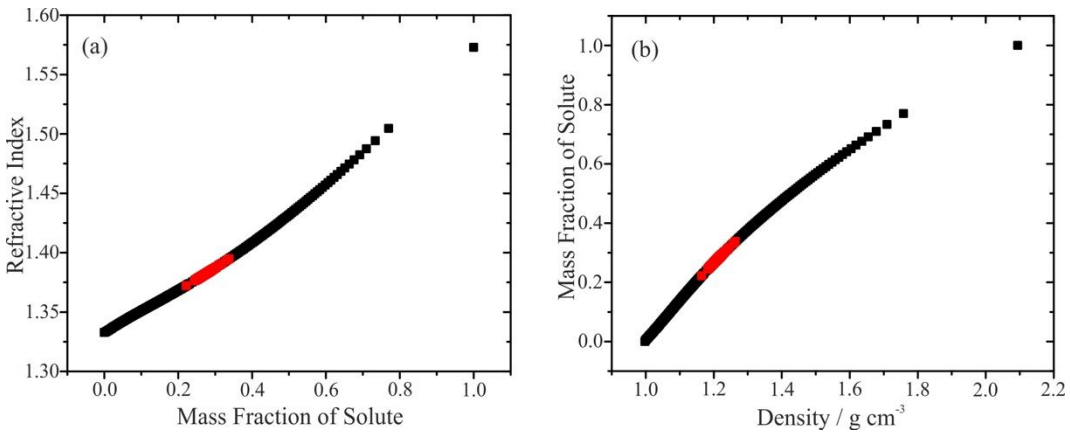

Figure 4.5: (a) A graph of the refractive index of a particle recorded at 589 nm against the MFS. (b) A graph of the MFS of a particle against the density in μg cm^{-3}. The black dots represent the values predicted by the E-AIM model, the red dots represent a sample dataset of a 0.8 a_W aqueous sodium chloride droplet, exposed to an ensemble of 0.8 a_W sodium chloride aerosol.

The particle volume is multiplied by the assigned density to determine the droplet mass (Equation 4.7). The droplet mass is multiplied by the water activity for the solvent mass (Equation 4.8) and the MFS to estimate the solute mass (Equation 4.9). The solute mass is

presented as the dry mass in picograms. A 4.5 μm droplet of 0.8 a_w NaCl (*i.e.* at ~ 80 % RH) has a typical mass of solute of ~100 pg.

$$m = \rho V \quad \text{Equation 4.7}$$

$$m_{solvent} = m \times a_w \quad \text{Equation 4.8}$$

$$m_{solute} = m \times MFS \quad \text{Equation 4.9}$$

4.4. ACCRETION MEASUREMENTS ON OT1

The first measurements of accretion were performed on the OT1 system to enable comparison of the performance of both systems. However, OT1 is a modular unit and altering the gas flow inlet to the cell was more difficult, the experiments were eventually moved to OT2.

To conduct accretion measurements on both of the OT1 and OT2 systems it was first necessary to understand how an aqueous probe droplet, exposed only to atomized aerosol, would react. Specifically, whether the probe droplet radius would remain constant in the absence of MFC controlled humidified wet and dry nitrogen. Experiments were performed to investigate this. The next experiments undertaken were crude measurements of accretion, performed with a bubble valve regulating the flow rate of aerosol into the cell. The final experiments on OT1 investigated integrating the delivery of aerosol and humidity-controlled nitrogen before the cell.

4.4.1. STABILITY IN RELATIVE HUMIDITY

The system of gas flowing into the trapping cell was modified to investigate the stability in relative humidity experienced by a trapped droplet. In addition to humidified nitrogen (blue line in Figure 4.6) a gas supply line which passes through a constant output atomizer (TSI 3076) was added. The atomized aerosol was then removed by a HEPA filter, and the gas flow rate was controlled using a needle valve with a purge to remove excess pressure. This is represented by the green line in Figure 4.6. The objective of this experiment was to

examine the stability of the relative humidity in the trapping cell and the sensitivity of the probe droplet to changes in gas flow in the absence of aerosol mass.

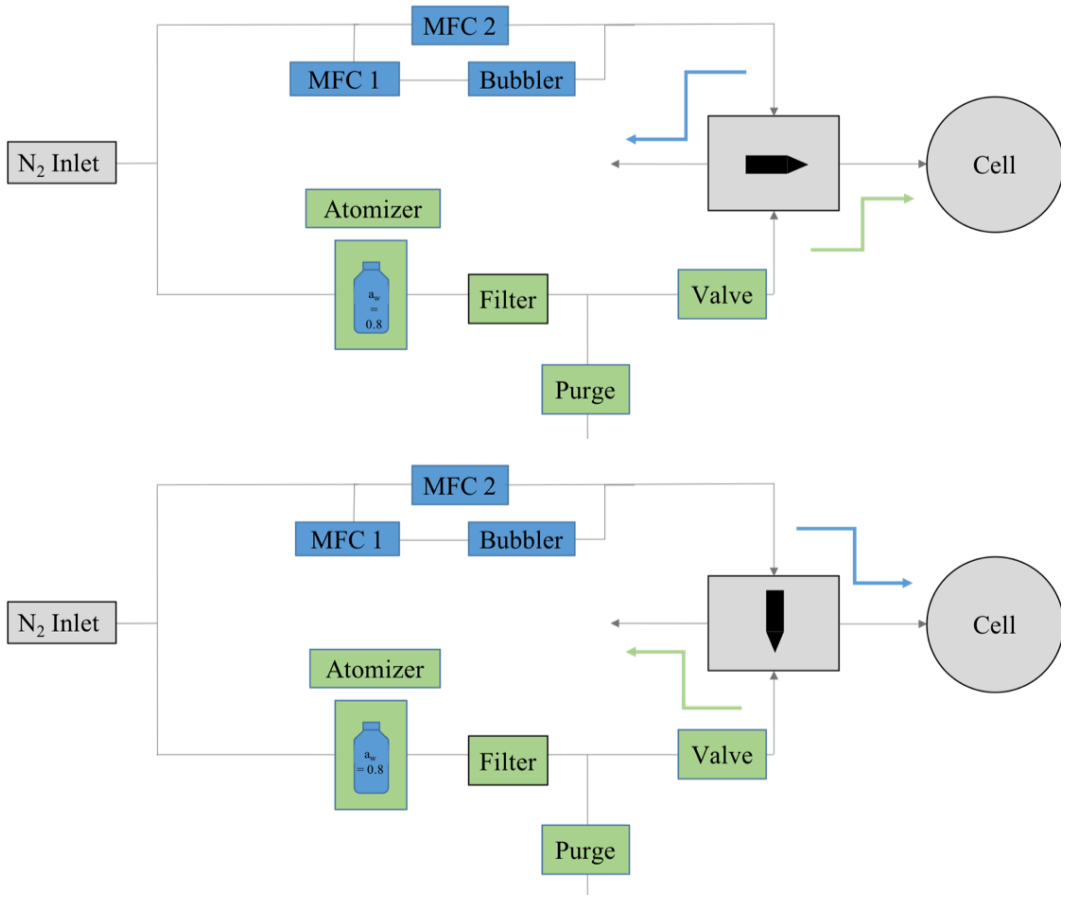

Figure 4.6: A diagram of the RH control system (blue) and aerosol generation system (green) leading to the cell with a switch to alter the flow which was directed into the cell. MFC stands for mass flow controller.

Numerous stability tests were performed and analysed, and one example is shown below, illustrating the repeated switching between flows. An aqueous sodium chloride droplet with a water activity of 0.8 was trapped using the OT1 system, the relative humidity was set to 80 % and the droplet was left to equilibrate under a humidified nitrogen gas flow. The atomizer was loaded with the same solution of aqueous sodium chloride ($a_w = 0.8$). The gas supply was switched from humidified nitrogen (blue) to humidified nitrogen supplied by

the atomized sodium chloride aerosol flow (green) at 2500 s, with the expectation that the RH should maintain a steady value.

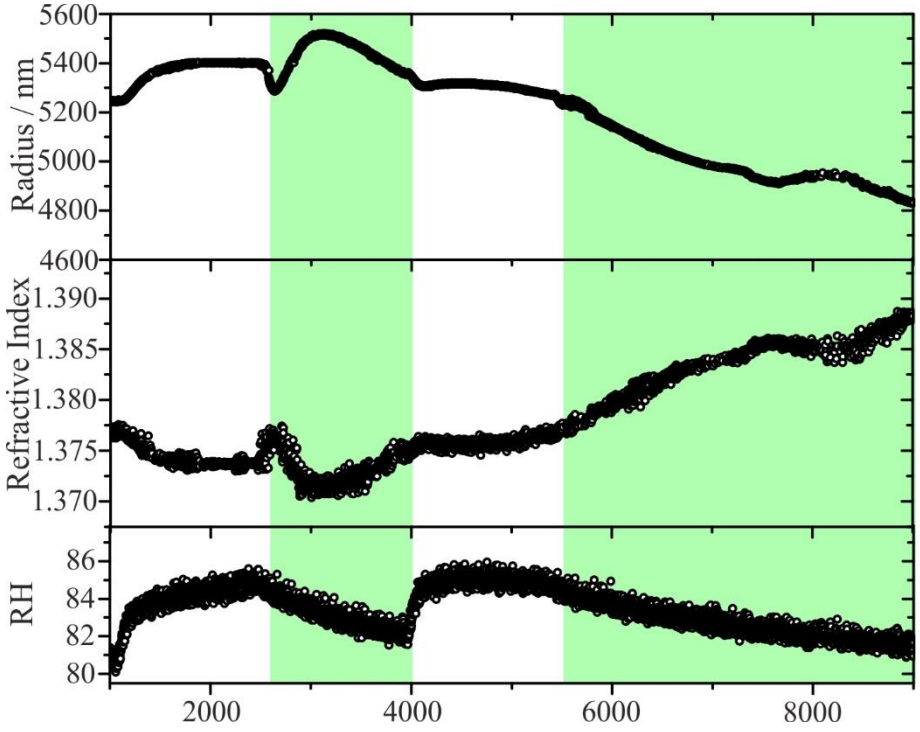

Figure 4.7: Three graphs showing the droplet radius (a) RI (b) and RH (c) evolve over time as the gas flow inlet source is changed from wet / dry nitrogen (blue) to atomized aerosol (green).

The radius of the droplet decreased during the process of the switch, which took approximately 100 seconds. Following this a slight drift in humidity led to an increase in size and reduction in RI. Overall, steady periods of size could be achieved when the humidified gas flow originates from the bubbler system (indicated by the time periods without green). However, during periods when the humidified supply was from the atomiser (green periods), a steady declined occurred over time arising from the time dependent concentration of solute remaining in the atomiser that can typically occur. This is apparent during the repeated periods when the trapping cell RH is controlled by the flow from the atomiser. In this data set, the RI varies from 1.372 to ~1.390, equivalent to a variation of ~6 % RH in the trapping cell (see **Figure 4.7**). When the RH flow was supplied by the bubbler, the RH was steady at ~81 %, inferred from a RI of 1.375, a little lower than the value measured by the capacitance probe (also shown in **Figure 4.7**).

Figure 4.8 shows the variation in refractive index of the trapped droplet with radius. The droplet ranged from 5500 – 4750 nm in radius and 1.395 – 1.37 in refractive index. This

single track in variation in RI with radius is indicative of a droplet responding purely to changes in RH.

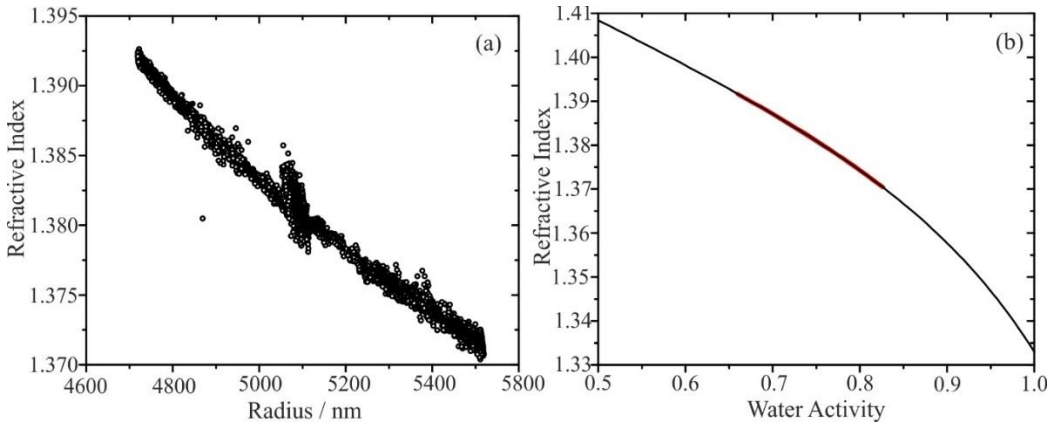

Figure 4.8: (a) A graph of the radius against RI. (b) A graph of the refractive index of sodium chloride against water activity. The red section indicates where the recorded refractive index from Figure 4.7 falls along a modelled curve.

The trends observed here are consistent with other similar experiments. Although the stability is high when controlling the RH from the bubbler, the stability is inferior when using the atomiser due to a time-dependent variation in the atomiser solution. This gradual change in the concentration of the solution was due to the set-up of the atomizer in recirculation mode, in which the atomizer draws solution, and dumps waste solution in the same vessel. These results indicated that, primarily, the sampling aerosol flow from the atomizer should be set up in non-recirculation mode. These results also suggest that the sampling aerosol flow (from the atomiser or from ambient air) should be introduced into

the trapping cell as a minor component of a more continuous flow designed to regulate the RH and minimise noise in the sampling droplet size and RI.

4.4.2. ACCRETION ON OT1 – REMOVING THE FILTER

Figure 4.9 shows the experimental design for the following experiments. The HEPA filter was removed from the gas flow line, allowing aerosol to pass through the cell and coalescence events with the trapped droplet to occur.

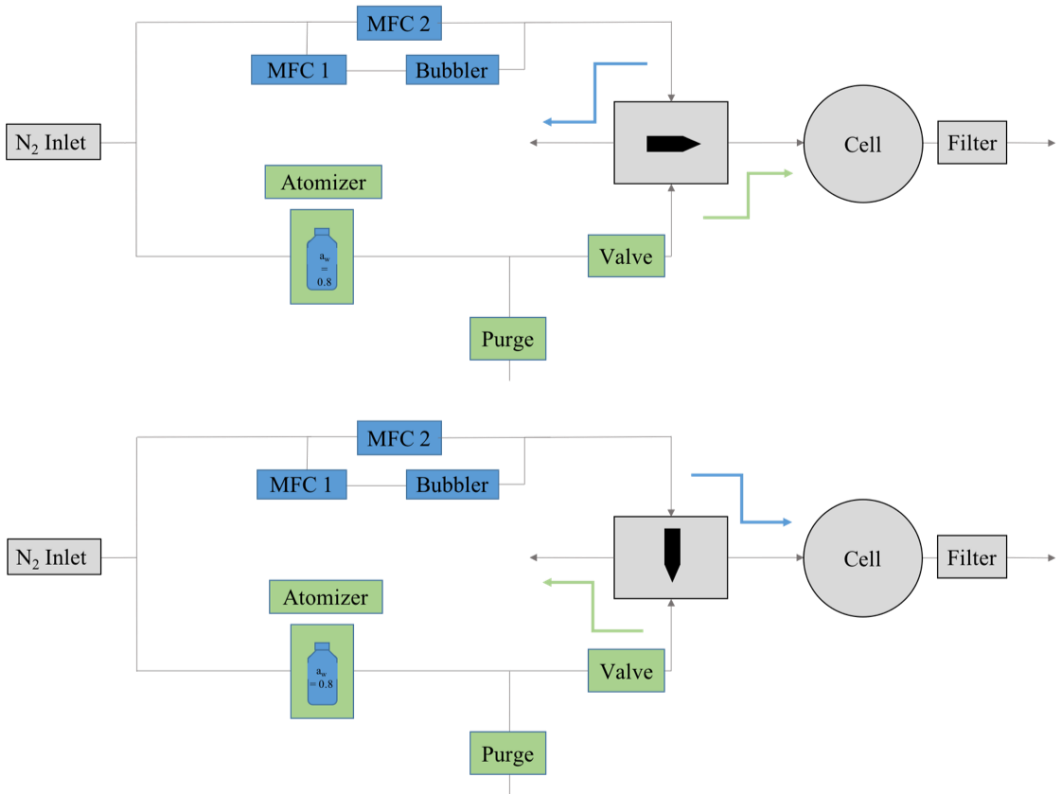

Figure 4.9: Experimental design of the accretion measurement with the filter removed on OT1.

A probe droplet of aqueous NaCl with a 0.8 water activity was trapped and equilibrated for an hour. The gas flow was switched from humidified wet/dry nitrogen to aerosol generated by an atomizer, in non-recirculation mode, with a solution of aqueous NaCl solution with a 0.8 water activity. The atomized aerosol was directed through the cell, resulting in the

probe droplet accreting mass. After a set period of time, the gas flow was switched back to wet/dry humidified nitrogen (Figure 4.10).

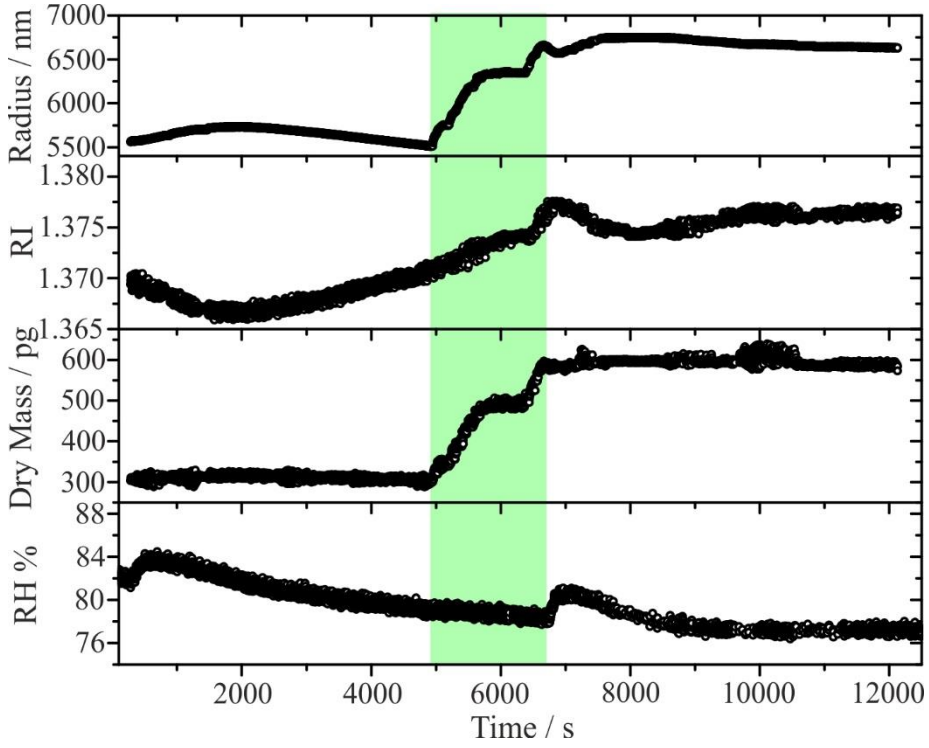

Figure 4.10: Four graphs showing an accretion measurement on OT1. From the top in descending order, radius, refractive index, dry mass and relative humidity over time. A droplet is stabilised under relative humidity gas flow (white background) until ~4900 seconds, at which point the gas flow is switched to atomized aerosol (green background) for ~2000 seconds, the droplet is then re-stabilised under relative humidity-controlled gas flow for ~6000 seconds.

The radius of the droplet increased from 5500 nm to 6500 nm as the droplet was exposed to the atomized aerosol. The switch took approximately 100 seconds at ~4900 seconds. The relative humidity decreased to ~78 % throughout the accretion period. The RI increased from 1.370 to 1.377. The 0.8 a_W atomized solution and probe droplet became slightly more concentrated as equilibration to the lower RH occurred. The surrounding RH increased to 80 % once the gas flow was switched back to RH control at ~6800 seconds, leading to a decrease in RI.

The calculated dry solute mass is shown in the third panel of Figure 4.10 and shows an increase in dry mass of ~300 pg over 2000 seconds of exposure to the atomized aerosol. As expected the dry mass is constant when the droplet is exposed to the humidified gas

flow, and any changes to radius and RI during these periods is solely due to low frequency instabilities in the relative humidity.

Figure 4.11 reports the refractive index of the trapped droplet against radius, and the refractive index against the water activity. The droplet ranged from 5500 – 6800 nm in radius and 1.395 – 1.37 in refractive index. This dual track in variation in RI with radius is indicative of a droplet responding to changes in the mass fraction of solute.

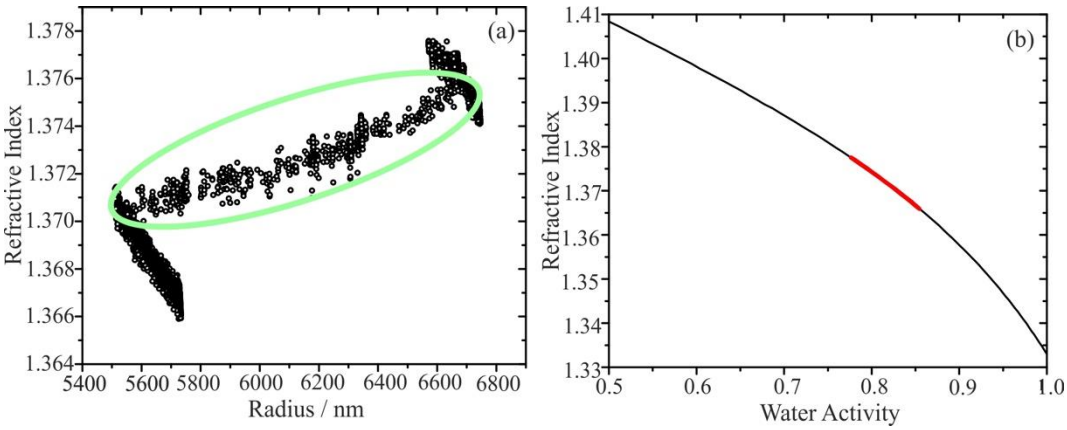

Figure 4.11: (a) shows a graph of refractive index against radius for the experiment shown in Figure 4.10. The data within the green oval indicates the period of accretion. (b) shows a graph of refractive index against radius for the same experiment, shown by the red dots along a modelled curve (black line).

The trends observed here are consistent with other accretion experiments. The stability in RH was somewhat stable when using the atomiser in non-recirculation mode due to the absence of a time-dependent variation in the atomiser solution. However, the sharp increase in RH when the flow was switched to humidified nitrogen suggests that the gas flow should be introduced into the trapping cell as a minor component of a more continuous flow. An integration of aerosol and RH control will regulate the RH and minimise noise in the sampling droplet size and RI.

Figure 4.12 displays five periods of accretion, normalised with respect to both time and radius for comparison. The flow rate of atomized aerosol was controlled using a bubble valve and purge system. In these five experiments the flow rate of atomized aerosol was between 0.01 and 0.04 L/min. Due to the high error on the bubble valve, the propensity of the atomizer and valve to block when using a high weight percent solution and the perturbation to the gas flow going into the atomizer the gas flow rate is presented with a high error of at least ± 0.1 L/min. An example of this is the red dataset shown in **Figure**

4.12 at 250 seconds, the atomizer became blocked and the airflow had to be adjusted to clear the blockage.

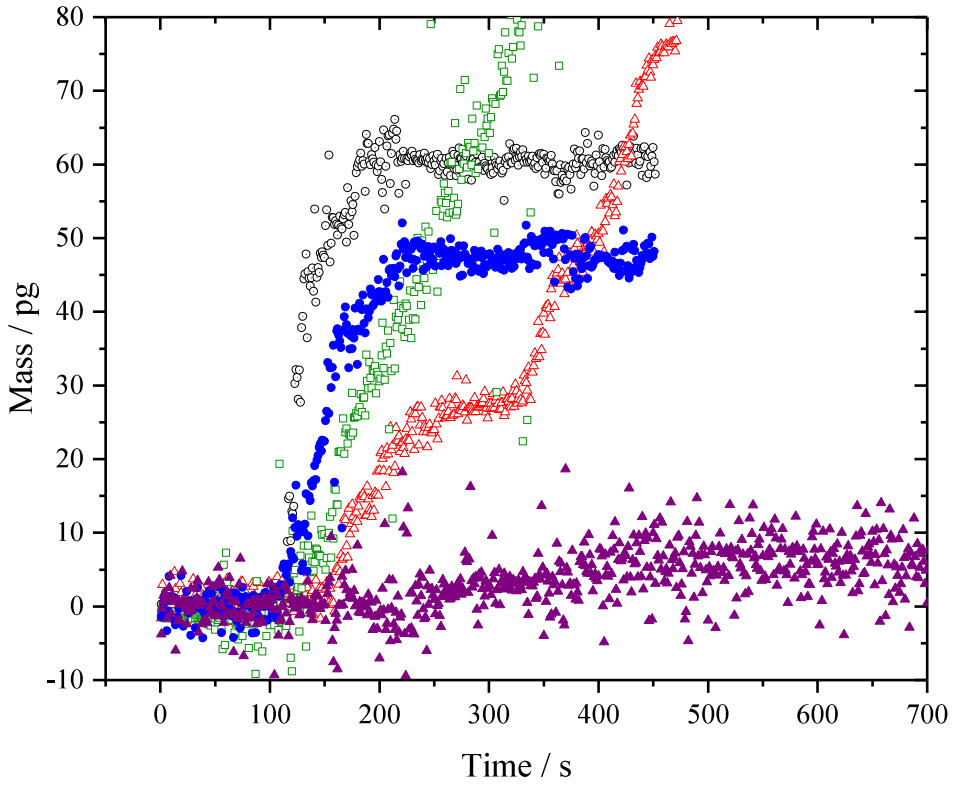

Figure 4.12: A graph showing 5 different accretion measurements each with a different gas flow rate. For accretion rates of 0.03 and 0.04 L/min (blue and black respectively), the atomized airflow was switched off at a time ~200 seconds. Purple data, 0.01 L/min; red data 0.02-0.03 L/min; black data, 0.03 L/min; green data, 0.03 L/min; blue data, 0.04 L/min.

Although the size distribution and number concentrations of the atomized aerosol were not determined for this set of measurements (undertaken prior to the purchase of the NanoScan instrument) the mass flux accreted by the sampling droplet is between 1×10^{-3} and 0.2 pg s^{-1}. The period of accretion varied between 70 – 2000 seconds and the dry mass accreted was between 6 – 300 pg. In previous work the mass flux accreted by sampling droplets was in the range of 1×10^{-5} to 0.1 pg s^{-1}.[2] This increase in mass flux accretion can be attributed to the high weight percent solution used in the atomizer in this work. Broadly, a systematic variation in accretion rate with aerosol flow rate is observed, as seen in Table 4.1. This is

because as more particles pass through the optical trap per second, there is an increased change for more accretion events to occur.

Table 4.1: A table showing the accretion rate for each accretion dataset shown in Figure 4.12.

Dataset	Accretion Rate / pg s^{-1}
Black (300 sccm)	0.29902
Red (300 – 200 sccm)	0.08563
Green (300 sccm)	0.2111
Blue (400 sccm)	0.21675
Purple (100 sccm)	0.00791

4.4.3. INTEGRATING THE RELATIVE HUMIDITY AND AEROSOL DELIVERY SYSTEMS

The delivery of aerosol was integrated into the RH control system and MFC's were placed before a Tedlar bag (Adtech) which introduced a 40 L mixing volume for supplying aerosol. Also passed into the bag was the aerosol generated from the sodium chloride solution (a_w = 0.8). This bag provided a buffering volume which prevented the droplet being knocked from the trap by fluctuations in the gas flow rate. The bag had a purge to remove excess air flow and prevent the bag from bursting. The gas flow rate through the

cell was controlled using a low flow metering valve positioned after the cell acting to regulate the aerosol flow.

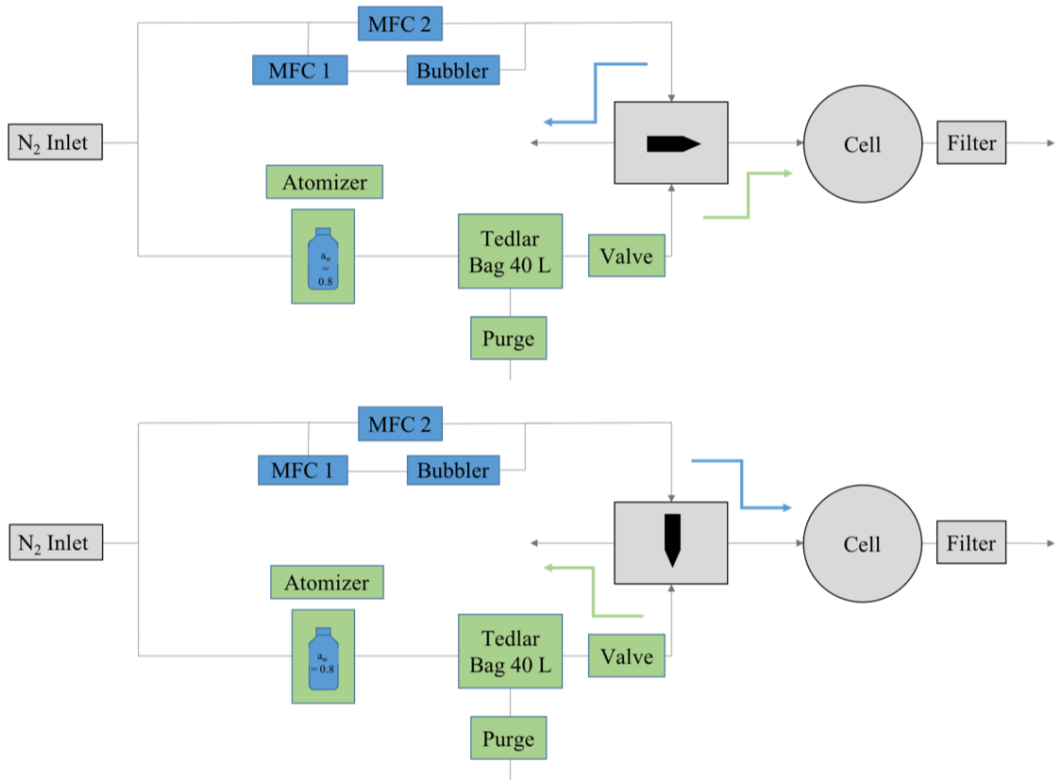

Figure 4.13: A schematic of the final experimental setup on OT1.

An OPS was positioned after the valve and drew from a conical flask which was unsealed. This buffer volume was introduced as the mass concentration of aerosol which was passed through the cell was above 3000 particles cm^{-3}, the saturation limit above which the OPS

could not record mass concentration or size distribution. **Figure 4.14** shows an example of an accretion measurement taken using the experimental setup in Figure 4.13.

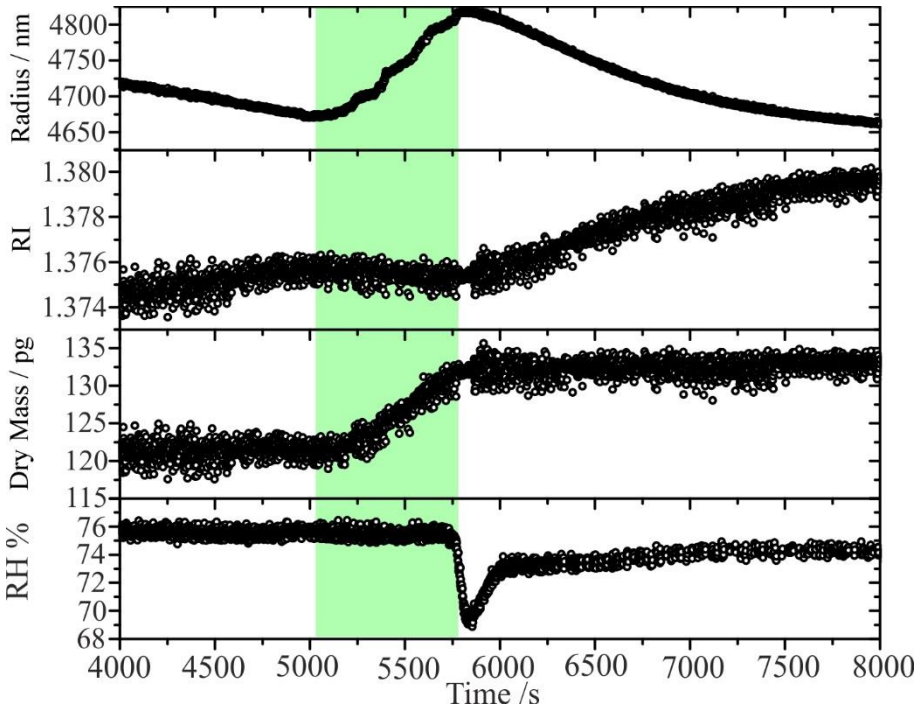

Figure 4.14: Four graphs from an experiment using a 0.8 a_w sodium chloride droplet, radius, RI, dry mass and RH over 4000 seconds during which a 670 second accretion (green shading) took place.

The radius of the droplet increased from 4675 nm to 4825 nm as the droplet was exposed to the atomized aerosol. The switch took approximately 100 seconds at ~5025 seconds. The relative humidity stayed at ~76 % throughout the accretion period. The RI decreased slightly from 1.376 to 1.375. The RH sharply decreased and then increased again to 73 % after the period of accretion. The calculated dry mass is shown in the third panel and shows an increase in dry mass of ~12 pg over 670 seconds of exposure to the atomized aerosol. The accretion rate was 0.0179 pg s^{-1}. The dry mass remains constant when the droplet is

exposed solely to the humidified gas flow and has therefore successfully stabilised the droplet.

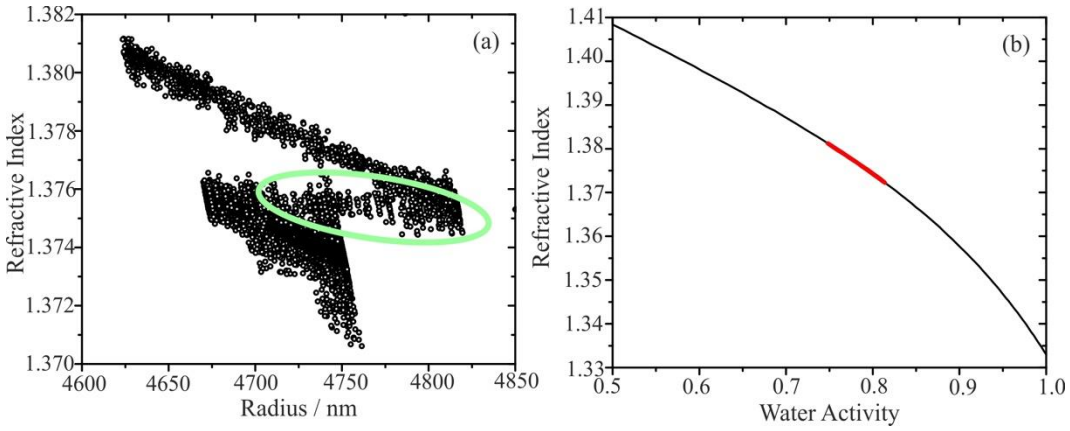

Figure 4.15: (a) a graph of refractive index against radius for the data in Figure 4.14. The data within the green oval indicates the period of accretion. (b) A graph of the refractive index against water activity, black lines – model, red data experimental data.

Figure 4.15 shows the refractive index of the trapped droplet against radius, and the refractive index against the water activity. The droplet ranged from 4625 – 4825 nm in radius and 1.371 – 1.382 in refractive index. The dual track in variation in RI with radius is indicative of a droplet responding to changes in the mass fraction of solute.

The trends observed here are consistent with other accretion experiments. The stability in RH was somewhat similar to the experiments without use of the 40 L mixing volume. There was a significantly lower rate of accretion observed when the mixing volume was added. This may have been due to additional deposition loss occurring due to an increase in the total volume of the gas flow system, or a slight loss of gas flow pressure, decreasing the flow rate. It is not possible to define the point at which the bag has become ‘full’ and the pressure of the introductory flow is not uniform from experiment to experiment.

Figure 4.16 (a) shows a mean mass concentration of the ensemble flow as a function of size distribution. The mean mass concentration was calculated over 670 samples. The samples were recorded at a rate of 1 sample per second. **Figure 4.16** (b) shows the period of accretion with a linear fitting. The linear fit showed an accretion rate of 0.01627 pg s^{-1}.

Figure 4.16 also shows the total mass concentration of ensemble flow recorded by the OPS during the accretion period.

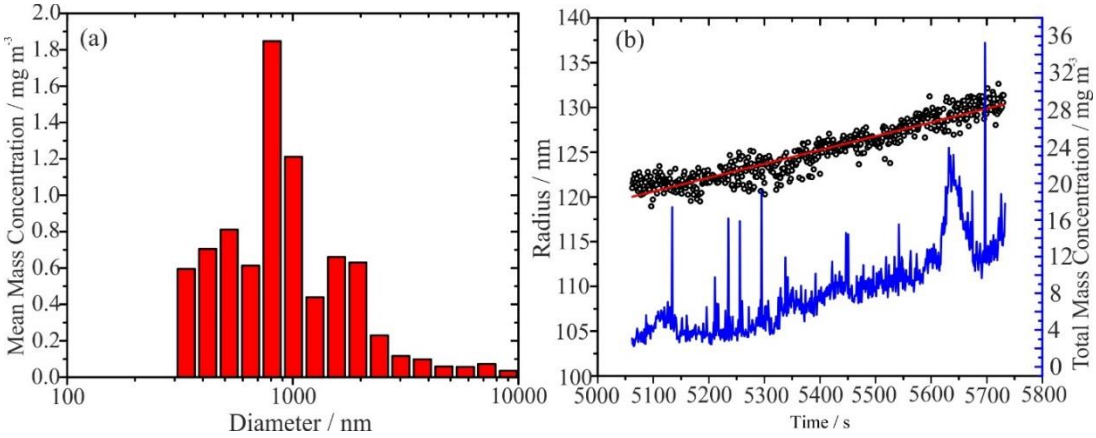

Figure 4.16: (a) A graph of the mean mass concentration of aerosol passing through the cell during the 670 seconds of accretion. The data were recorded at a rate of one sample per second. (b) A graph showing the period of accretion (black dots) with a linear fitting (red line), against time. In blue is the total mass concentration of aerosol passing through the cell.

The total mass concentration gradually increased throughout the accretion period. This may be due to an incremental build-up of aerosol saturating the system. However, there is significant noise associated with the measurements. This is due to the fact that this was not a closed system. The trapping cell outlet and the OPS inlet were both situated in an open conical flask. This was to prevent damage to the OPS pump, which draws at a rate of 1 L/min. The pump can be easily broken when the system is closed and there is insufficient gas available to draw. The maximum gas flow out of the trapping cell was 0.5 L/min, assuming the cell was completely sealed. Consequentially, there is a significant noise component in the OPS measurements of mass concentration as lab-air is likely also to have been sampled.

One solution to this problem is the introduction of a secondary mixing volume (Tedlar bag) and an additional gas flow after the trapping cell. This will be explored over the course of a series of measurements on OT2.

4.5. ACCRETION MEASUREMENTS ON OT2

The accretion measurements on OT2 employed an experimental design that integrated the delivery of aerosol and RH control. The accretion system on OT2 included an OPS/NanoScan instrument to record mass and number concentrations of aerosol. The

experiments in this chapter look at the effects of lower mass concentrations of aerosol on accretion rate.

4.5.1. EXPERIMENTAL SETUP

The accretion measurements were performed on OT2 and the first setup is shown in **Figure 4.17**. In this experiment design, five MFC's were incorporated (Bronkhorst digital and analogue). Two 0.3 L / min MFC's provided accurate gas flow for the RH control system. A 30 L / min MFC was used to regulate the flow rate of gas through the atomizer and was set at 3.5 L / min. A 10 L / min MFC and a water bubbler were used to ensure proper humidification of the aerosol line. This additional nitrogen was used to change the mass concentration of the aerosol which was directed through the cell.

The final MFC used was calibrated for an argon flow, at a maximum flow rate of 5 L/min. This experiment needed nitrogen to be used in the MFC calibrated for argon. This required a gas correction factor (gas correction factor 1.39)[105] to calculated the flow rate of nitrogen through the MFC. The argon MFC supplied a dilution flow of humidified nitrogen to bag 2. This was done to ensure sufficient gas flow for the OPS/NanoScan pump. The dilution flow rate for bag 2 was set at 1.4 L / min of nitrogen. This additional flow rate is accounted for in the final calculation of post cell mass concentration. The aerosol flow rate was controlled using a needle valve before the cell. The aerosol could be introduced to the cell in either the axial or radial orientation.

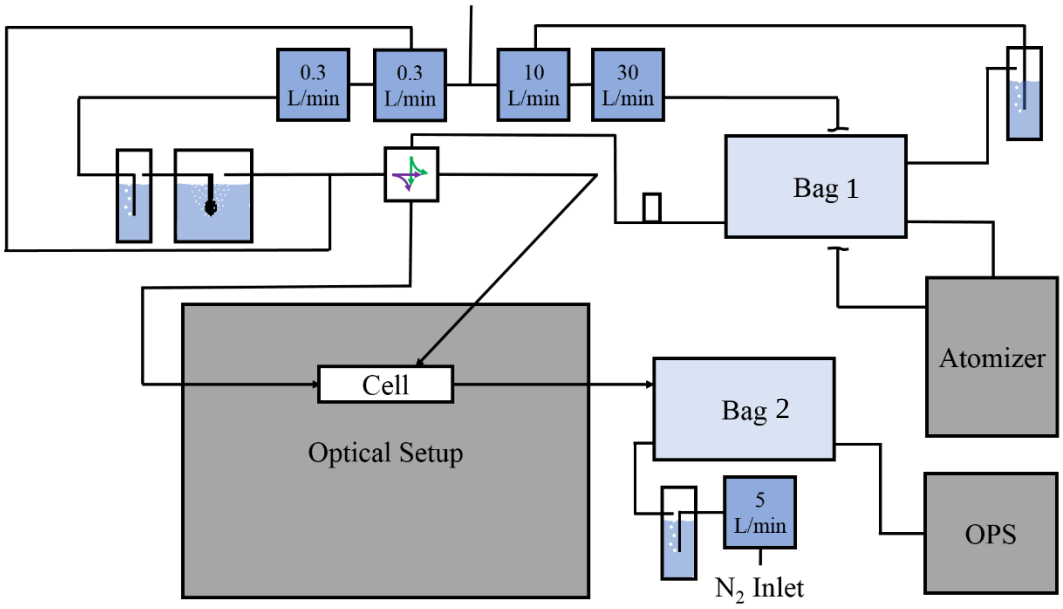

Figure 4.17: A schematic of the accretion system on OT2, with a switch designed to combine the delivery of aerosol and RH control. The switch can pass aerosol and RH control gas flow through

the cell in either the axial or the radial orientation. A secondary buffering volume bag has been added after the cell to improve the collection efficiency of the particle counting and sizing.

A second Tedlar bag was used to provide a buffering volume (40 L) for the OPS sampling. The exhaust from the trapping cell and a humidified gas flow from a 5 L / min Argon MFC (Bronkhorst, analogue, N_2:Ar conversion ratio 1:1.4) supplied flow to the bag. The humidified gas flow was incorporated to dilute the mass concentration of aerosol from the exhaust to prevent the OPS from saturating. There was a time delay of ~1 minute at the point that aerosol was passed into the cell before the OPS/NanoScan recorded atomized aerosol.

4.5.2. GAS FLOW SYSTEM CALIBRATION

The needle valve containing the flow of aerosol into the optical trapping cell was calibrated for each of the dilution flow rates to be tested, the results can be seen in Figure 4.18. The undulation of the needle valve calibration is a result of a misalignment of the threading, although this was not thought to undermine the effectiveness of the needle valve as the calibration was repeated > 9 times and all of the results were in good agreement.

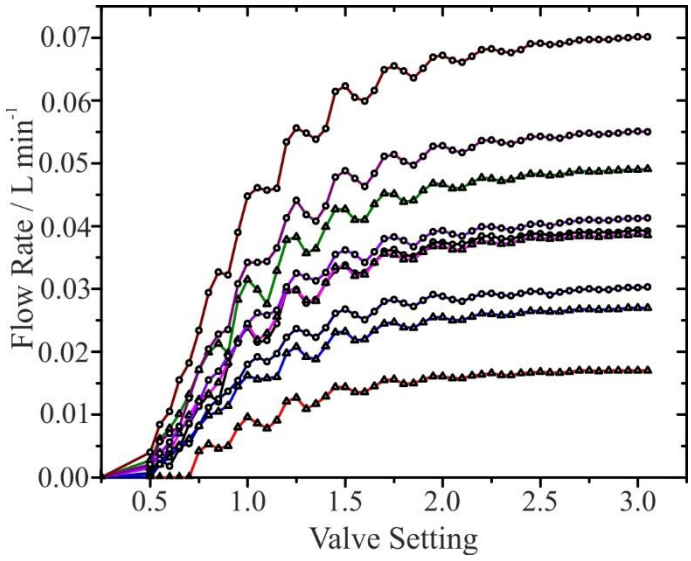

Figure 4.18: A graph showing the flow rate of gas passed through the needle valve against the Vernier scale setting. Circles: 3.5 L/min atomizer flow, triangles: 2 L/min atomizer flow. Black line, navy line, circle, 0 L/min dilution; lilac line, circles, 1 L/min dilution; purple line, circles, 2 L/min dilution; brown line, circles, 3 L/min dilution; red line, triangles, 0 L/min dilution; blue line, triangles, 1 L/min dilution; pink line, triangles, 2 L/min dilution; green line, triangles, 3 L/min dilution.

The atomizer was tested at a rate of 3.5 L / min and 2.0 L / min. However, at the lower flow rate the atomizer had a tendency to block when supplied with a high concentration solution.

The use of a high concentration solution of aqueous sodium chloride was necessary for these experiments. A solution at 0.8 a_w of sodium chloride was chosen as it is a very well-defined, and benchmarked system, widely studied in the field of aerosol research. In all of the accretion measurements performed, the probe droplet had a water activity of 0.8, and was held at 80 % relative humidity. When the RH inside the cell was reduced to <65 %, sodium chloride deposited on the coverslip can crystallise and ruin the experiment. Thus, it is crucial to maintain a high relative humidity to perform experiments at this water activity. The lowest water activity accessible in the bulk phase is ~0.75 due to the bulk solubility limit of sodium chloride at room temperature (357 g/L).[106] It was necessary to match the water activity of the probe droplet and the atomizer solution to avoid complications from RH variation at this early stage of instrument benchmarking. Upon accreting an atomized solution of a higher water activity, that is a less concentrated solution, a probe droplet would be in a state of constant re-equilibration with the surrounding environment. This would add an additional component to account for when analysing the changes to droplet radius and RI.

4.5.3. A Study of The Mass Concentration of Aerosol and the Effects on The Accretion Rate

The experiment shown in Figure 4.19 shows two periods of accretion (green periods). In all periods of accretion, the flow rate of aerosol into the cell was 0.004 L/min. During the first period of accretion, aerosol was introduced in the radial orientation at 3800 seconds. During the second period of accretion, aerosol was introduced in the axial orientation at 8200 seconds. Fist, the droplet was stabilised under a 0.01 L / min flow rate of 80 % relative humidity in the radial orientation. The initial probe droplet size was 4500 nm. During the first accretion period the radius increased to 4800 nm. Approximately 100 seconds after the first accretion period ended the gas flow orientation was switched from radial to axial. At this point the radius of the probe droplet increased by ~600 nm. This was due to a gradual increase in the cell RH when the wet:dry nitrogen was introduced in the axial orientation. At 8200 seconds, 0.025 L / min of aerosol was introduced in the axial orientation. The

droplet radius and dry mass quickly increased. The accretion period was cut short as the droplet fell from the trap after 7 minutes.

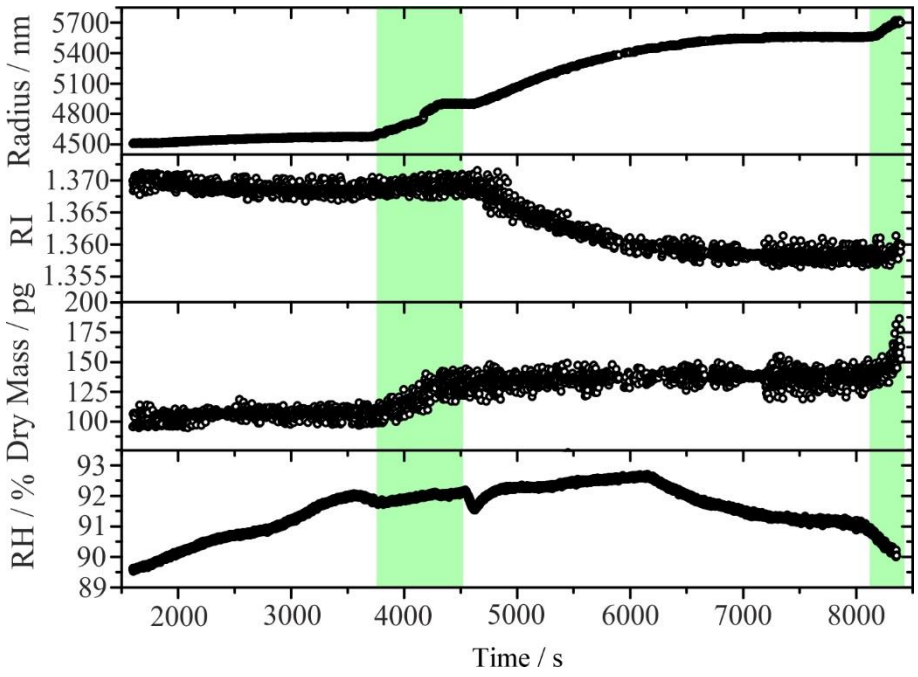

Figure 4.19: Four graphs showing, in descending order radius, RI, dry mass and RH over time for the 0 L / min dilution accretion experiment on OT2. The green sections represent periods of accretion, the first period of accretion was in the radial orientation, the second period of accretion was in the axial orientation.

As discussed in section 2.8, the axial orientation inlet is closer in proximity to the probe droplet and the narrower bore tube (1/8 in.) supplies the same gas flow rate with a higher velocity. The refractive index of the probe droplet stayed constant throughout the accretion periods, which was to be expected as any changes to the droplet water activity would reflect changes in the cell RH not due to changes in the probe droplet resulting from accretion. The calculated dry mass increased during the accretion periods and displays constant values in between periods of accretion, as no coalescence events were occurring. When aerosol was introduced in the radial orientation a total of 23.6 pg of mass was added to the ~100 pg droplet at a rate of 0.047 pg s^{-1}. When aerosol was introduced in the axial orientation a total of 44.6 pg was added to the ~125 pg droplet at a rate of 0.118 pg s^{-1}. The higher

accretion rate in the axial orientation suggests that it is preferable to situate an aerosol inlet in the axial orientation. More work is needed to support this conclusion.

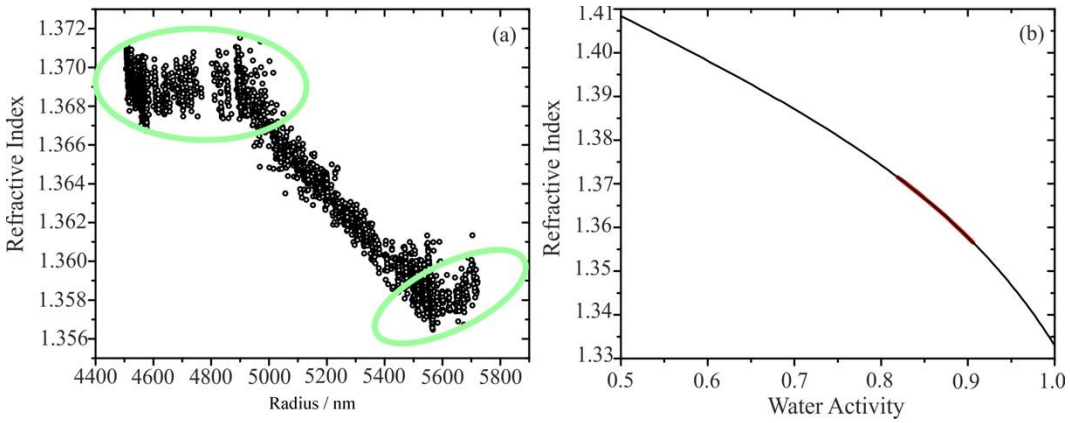

Figure 4.20: (a) a graph of refractive index against radius for the data in Figure 4.19. The data within the green ovals indicates the two periods of accretion. (b) A graph of the refractive index against water activity, black lines – model, red data experimental data.

Figure 4.20 shows the refractive index of the trapped droplet against radius, and the refractive index against the water activity. The droplet ranged from 4500– 5700 nm in radius and 1.356 – 1.371 in refractive index. The dual track in variation in RI with radius is indicative of a droplet responding to changes in the mass fraction of solute.

The trends observed here are consistent with other accretion experiments. It is possible to see two 'flat' sections of data, one at a lower radius, higher RI, indicating the first period of accretion in the radial orientation and a second 'flat' section at a higher radius, lower RI, indicating the second accretion period in the axial orientation. The central section with a negative gradient is representative of the ~3000 second period of equilibration in relative humidity between the two periods of accretion.

4.5.4. MASS CONCENTRATION RECORDED BY THE NANOSCAN

The black data in panel (a) in **Figure 4.21** displays the total mass concentration recorded by the NanoScan from bag 2 throughout the accretion experiment. The two periods of green indicate the two accretion periods. The average mass concentration during the first period of accretion was 359.12 μg m^{-3}. The mean total mass concentration during the second accretion period was 0.11 μg m^{-3}. The black data in panel (b) of **Figure 4.21** shows the geometric mean diameter recorded by the NanoScan from bag 2 throughout the accretion measurement. The mean diameter of the aerosol particles in bag 2 ranged from 100 to 250 nm throughout the experiment. The total mass concentration in bag 2 decreases throughout

an experiment because of the 1.4 L/min dilution flow added to the bag, which acts to dilute the concentration of aerosol in the bag over time.

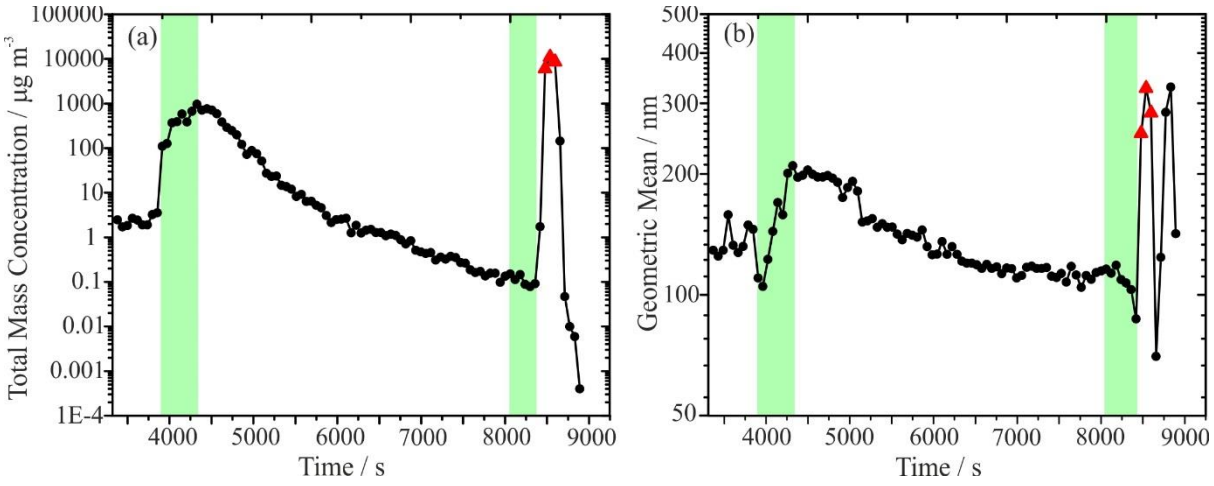

Figure 4.21: Two graphs of the total mass concentration (a), and the geometric mean (b) against time for the experiment displayed in Figure 4.19. The data was recorded using the NanoScan from bag 2, black dots, and bag 1, red triangles. Again, the green sections represent periods of accretion in the radial and axial orientation.

The red triangles on panels (a) and (b) of **Figure 4.21** represent the total mass concentration and geometric mean diameter respectively in bag 1 immediately after the accretion measurement. This is used to estimate the deposition loss throughout the experiment. The total mass concentration is significantly higher in bag 1, ~ 10000 μg m^{-3}, than in bag 2, ~ 0.1-1000 μg m^{-3} or < 1 μg m^{-3} immediately prior to sampling from bag 1. The total mass concentration is only recorded for a couple of samples before the saturation limit of the instrument is reached and the readings decrease before no sample is recorded at all. The geometric mean diameter of the particles in bag 1 was 250-300 nm, the particles were significantly larger in bag 1 than bag 2. It is logical that the total mass concentration would be higher in bag 1 than bag 2, as aerosol is lost through deposition through the flow system. It is also logical that the geometric mean diameter is higher in bag 1 than bag 2 as the larger, coarse mode particles are more likely to be lost by impaction through the flow system.

Table 4.2 shows the accretion experiments on OT2 categorised by the dilution flow rate supplied to bag 1, and the orientation of aerosol delivery to the cell. For each experiment the accretion rate is presented in units of pg s^{-1}, this is sometimes referred to as mass flux.

The mass accreted is the difference between the dry mass of the droplet before and after the period of accretion and is presented in picograms.

Table 4.2: A table of a series of accretion experiments on OT2. The experiments had a dilution flow of between 0 and 20 L / min and the aerosol was introduced in the axial and the radial orientation.

Dilution Flow Rate (bag 1) / Lmin^{-1}	**Aerosol Inlet Orientation**	**Accretion Rate / pg s^{-1}**	**Mass Accreted / pg**
0	Radial	0.047	23.6
0	Axial	0.118	44.6
2	Radial	4.2×10^{-4}	4.3
2	Axial	6.8×10^{-4}	2
3.5	Radial	8.3×10^{-4}	1.9
3.5	Axial	8.3×10^{-4}	1.1
7	Radial	-2.9×10^{-4}	-0.1
7	Axial	1.7×10^{-4}	1.3
20	Radial	-4.5×10^{-4}	-1.7
20	Axial	-5.0×10^{-4}	-0.5

The accretion rate of the 0L/min dilution experiment was comparable to the accretion rate on OT2 with a Tedlar bag in the aerosol line, (0.0179 pg s^{-1}). The accretion rate in the axial orientation tended to be higher than in the radial orientation, leading to the conclusion that it may be preferable to introduce aerosol axially due to the greater trap strength in this orientation. It is possible that the optical forces of the expanding trap above the droplet act upon the ensemble flow of aerosol to direct it towards the probe droplet, thereby improving the accretion rate and increasing the mass flux into the probe droplet. The accretion rates shown here are comparable to those shown in the first exploratory study into this technique, in which the highest reported mass flux was 0.128 pg s^{-1}, and the lowest reported mass flux was 0.068 pg s^{-1}.[54]

Although the accretion experiments with a high dilution component, >7 L/min, displayed positive and negative rates of accretion, this is more likely to be a consequence of the uncertainties in the calculation of the probe droplet dry mass. The high dilution flow rate experiments also presented difficulties with handling a large flow rate: the Tedlar bags frequently punctured and needed replacing or repairing. It is recommended that the mixing volume is reduced, perhaps to 10 L, and made from a more robust material such as glass or plastic. It would also be advantageous if the mixing volume could be taken apart and

cleaned in between experiments to prevent build-up of deposited salts on the internal chamber walls. This would make it easier to investigate the accretion of a variety of salts.

Figure 4.22 shows four graphs. Panels (a) and (b) show the total mass concentration over time for the radially and axially introduced aerosol accretion experiments. Each of the dilution factors is represented by a different colour square. Panels (c) and (d) show the geometric mean diameter over time for the radially and axially introduced aerosol accretion experiments.

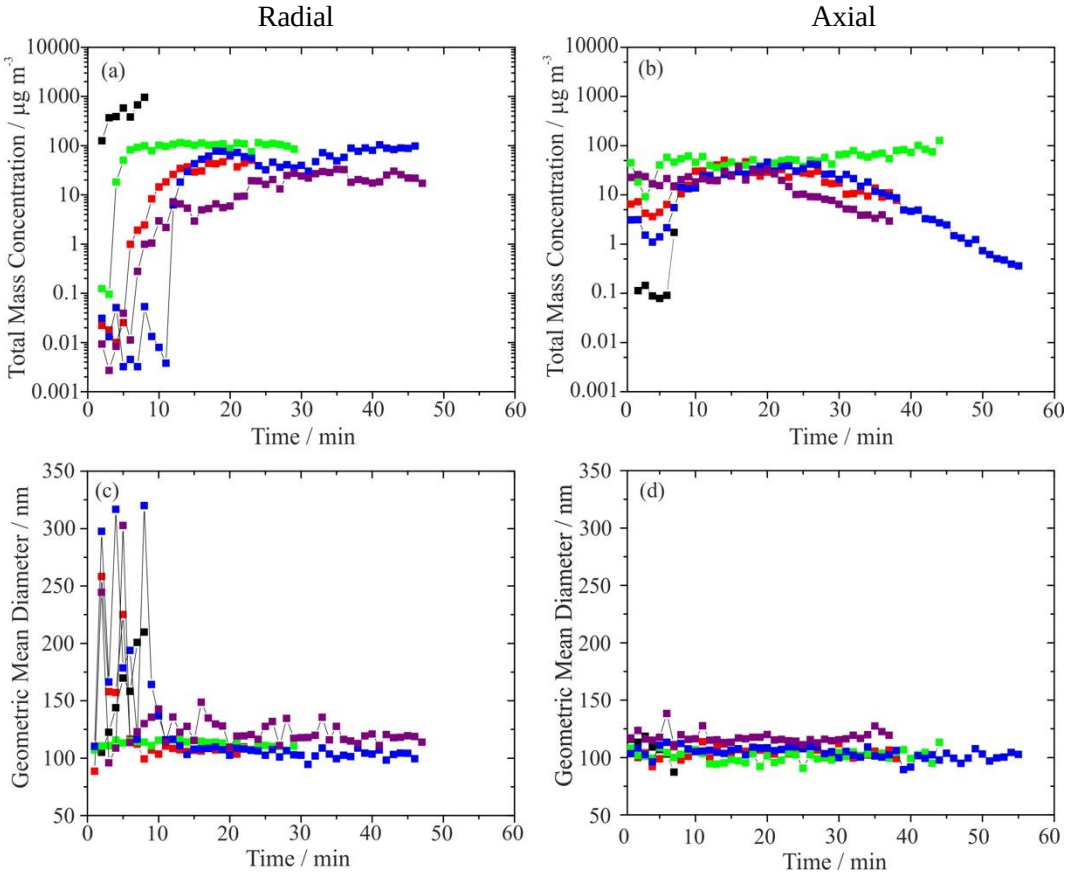

Figure 4.22: Panel (a) shows a graph of total mass concentration over time for the accretion experiments shown in Table 4.2 in the radial orientation, panel (b) axial orientation. Panels (c) and (d) show the geometric mean diameter over time for the same accretion measurements in the radial and axial orientation respectively. Black squares, 0 L/min dilution; red squares, 2 L/min; blue squares, 3.5 L/min; green squares, 7 L/min; purple squares, 20 L/min.

For the experiments in which aerosol was introduced in the radial orientation (left hand side of Figure 4.22), there is a broadly systematic variation in the total mass concentration achieved in bag 2 with dilution factor. As a larger volume of humidified nitrogen (20 L/min) is added to bag 1, the aerosol constitutes a lower proportion of the flow which is

directed into the trapping cell. Consequently, the NanoScan should record a lower mass concentration of aerosol for experiments with a larger dilution flow rate.

The total mass concentration inside bag 2 was generally lower for accretion periods in which the aerosol was introduced in the axial orientation (right hand side of Figure 4.22). This may have been due to the flow system becoming more blocked with salt over the course of an experiment. The flow rate of aerosol into the cell was 0.004 L/min for all experiments, but the narrower bore tube in the axial orientation limited the amount of aerosol which could enter the cell. There was no obvious trend in total mass concentration with the variation in mass loading controlled by the dilution of the aerosol flow when introduced in the axial orientation.

The geometric mean diameter in the radial orientation displayed a significant variation in first ~10 minutes. This may have been due to a stabilisation period required for the constant output atomizer to generate a uniform size distribution over time. This variation in geometric mean diameter may also have been the result of a 'period of mixing' in both bags 1 and 2. Once stabilised in the radial orientation accretion measurements, the mean geometric diameter tended to ~100 nm for all experiments in both the axial and radial orientation. This is in agreement with the previously reported accretion experiments by Haddrell *et al*.[2]

4.6. DEPOSITION LOSS IN THE SYSTEM

The amount of aerosol which had been 'lost' and the way that the size distribution of aerosol changed as it passed through the gas flow system and through the cell was investigated from the measured mass concentrations and size distributions recorded by the OPS. Aerosol deposits on the walls of pipes or the bag over time, either through contact with the container wall or through sedimentation. This affects the size distribution as larger particles tend to deposit more than smaller particles. To achieve this the mass concentration and size distribution of aerosol was recorded in bag 1 and bag 2 using the NanoScan. The total amount of deposition throughout the system is presented in Table 4.3 for the

experiments in Table 4.2. The ratio of the mean total mass concentrations in bag 1 and bag 2 are presented as a transmission efficiency of aerosol through the system.

Table 4.3: A table showing the total mass concentration recorded in both bag 1 and bag 2 during the accretion measurements.

Dilution Flow Rate to Bag 1 / L min^{-1}	**Mean Total Mass Concentration, Bag 2 / µg m^{-3}**	**Mean Total Mass Concentration, Bag 1 / µg m^{-3}**	**Transmission Efficiency**
0	920	10931	0.084
2	60	1154	0.052
3.5	112	1013	0.110
7	85	7484	0.011
20	33	3277	0.010

The deposition rates between in Table 4.3 are high, transmission efficiencies are low, and this in part due to the use of non-conductive tubing. Non-conductive tubing enhances the rate of particle loss due to the build-up of electrostatic charge within the pipe increasing the deposition rate. The large volume of the Tedlar bags also increases the deposition rate as there is a larger surface area on which the particles can deposit. The Tedlar bags are non-conductive and this enhances the build-up of electrostatic charge, increasing the deposition rate.

4.7. CONCLUSIONS

The experiments in this chapter sought to determine the challenges of measuring the accretion of aerosol into a trapped probe droplet. A body of accretion measurements have been performed on both a commercial, OT1 system and the research grade OT2 system. When compared to accretion measurements performed before this thesis, the results are comparable, and the experimental setup was more refined. A method for calculating the dry mass of a trapped probe droplet has been presented and was subsequently used to determine the rate of accretion of sample into the probe droplet. The accretion rates reported in this chapter were between 1.7×10^{-4} to 0.2 pg s^{-1}.

The accretion delivery system was rigorously tested, to enhance the rate of mass flux into the probe droplet. It was concluded that the atomizer was most efficient when set up in non-recirculation mode, and that the aerosol should be introduced as a minor component of a continuous gas flow with relative humidity control.

The setup on OT included two buffering volumes, Tedlar bags, before and after the trapping cell to introduce a dilution component. This dilution flow introduced the ability to change

the mass concentration of aerosol directed into the cell. It was shown that a higher mass concentration of aerosol passed through the cell would increase the rate of accretion into the probe droplet. The trapping cell on OT2 also had a secondary aerosol and gas flow inlet which was situated in the axial orientation relative to the probe droplet. Experiments in which the aerosol was introduced in the axial orientation showed higher rates of accretion which suggested that the expanding optical trap above the droplet enhanced the rate of accretion. It is hypothesised that the optical forces act on the aerosol, directing it towards the probe droplet.

5. Conclusions

In chapter 2, a second research-based system, OT2 was constructed and rigorously benchmarked against the commercial system, OT1. The OT2 instrument was built to examine the most effective experimental setup to examine the sampling of ambient aerosol using an AOT. The characterisation of OT1 and OT2 can be used as a baseline for comparison of future instruments. It was important to perform this comparison of baseline performance to understand the capabilities of the optical tweezers instrument with regard to detection of CWAs.

In addition to the features of OT1, a custom-built cell was designed which possessed the additional functionality of a 1/8 inch inlet in the axial orientation. This enabled the introduction of a gas flow directed vertically from above the trapped droplet. The axial oriented gas flow inlet was found to be desirable for the case of detection of CWAs *via* coalescence sampling. This was due to the enhanced trap stability in the axial orientation and the closer proximity of the axial inlet to the probe droplet, relative to the radial inlet. However, there were some issues encountered with probe droplet stability when gas flow was introduced in the axial orientation. Several variations of gas flow system were compared for the highest level of humidification and for the lowest levels of turbulence caused to the trapped droplet. Given the higher velocity of gas introduced in the axial direction, a water boat was used to humidify the gas flow. Although the water boat was found to humidify the gas flow less than a traditional bubbler, it was found to decrease the level of turbulence imparted to the trapped droplet. To counteract the lower humidification a bubbler with high level of humidification was selected for introduction of gas flow in the radial orientation. The full analysis of gas flow introduction was used in the determination of the ideal orientation of aerosol delivery for enhanced rates of accretion, and therefore sampling of CWA. The following chapters investigated delivery of aerosol in the axial and radial orientations.

A direct comparison of the two instruments was performed using the deviation from the mean in the wavelength of a whispering gallery mode (WGM). The deviation from the mean in the wavelength of a WGM provided a measure of how far data points were positioned from the mean trendline. This value provided a proxy for the value of ‘noise’

data points relative to the true signal, allowing the noise characteristics of two instruments to be compared. Results showed that the noise characteristics of OT1 were superior to OT2, OT1 had fewer data points deviating less far from the mean value, meaning that the data points were closer together and had a greater signal to noise ratio. The cause of the inferior noise characteristics of OT2 were found to be due to instabilities in the laser power. The value of residual, or deviation from the mean for the wavelength of the WGM was reduced from 6.29×10^{-5} to 1.25×10^{-5}, after the introduction of beamsplitter optics improved the laser stability. The reduction in the deviation from the mean of the WGM wavelength, improved the signal to noise ratio of OT2. The lower value of residual deviation from the mean on OT2 was similar to the mean residual value of OT1, which meant that the stability and noise characteristics of both instruments was comparable. Not only did this analysis identify an otherwise undetectable issue with the performance of OT2, but it also allowed direct comparison of both OT2 systems. It is recommended that all future Raman based optical tweezer instruments undergo noise analysis to ensure the noise characteristics are up to the same standard.

A second comparison of OT1 and OT2 was performed using the minimum trapping laser power required to levitate a series of trapped droplets. The results showed that both systems could levitate droplets with similar laser powers. This established and ensured that both instruments were able to generate equally stable optical traps. Further investigations were performed to establish the impact of gas flow rate, and gas inlet orientation on a trapped droplet. Increasing the gas flow rate decreased the stability of the droplets in the trap. However, there was no difference in trapping efficiency observed upon changing the gas inlet orientation. This is thought to be because of the increased strength of the trap in the axial orientation, allowing the droplet to withstand exposure to gas with a higher velocity. The minimum laser trapping power was converted into an axial trapping efficiency. The axial trapping efficiency for both systems were not significantly different, the trapping efficiency was 0.2 ± 0.06 for OT1 and 0.17 ± 0.06 for OT2. Both OT1 and OT2 have high efficiency in the axial orientation when compared to the literature,[107,108] and when compared to each other OT1 is marginally superior.

The minimum trapping laser power results indicated that droplets exposed to a multi-directional gas flow rate were less stable than the droplets exposed to a gas flow from one direction. This was thought to be the result of the mixing of two gas flows inside the trapping cell causing turbulence, which destabilised the trapped droplet. The results showed that this turbulence was not decreased by changing the mixing ratio of the two gas flows.

The impact of this finding is that, where possible, gas and aerosol should both be introduced from the one direction for the detection of CWAs *via* coalescence sampling.

An investigation into the rate of equilibration of a trapped droplet was performed as it limits the accretion rate of solute into the trapped droplet. There was no obvious variation in the rate of change of the probe droplet radius when the cell volume was reduced. The hypothesis was that when the volume of the cell is smaller, less aerosol or gas flow is required to fill the volume of the cell, and therefore more aerosol or gas flow could be accreted into, or change the radius of the probe droplet, increasing the rate of change of the droplet. The results implied that the cell volume had no effect on the rate of change of the trapped droplet and that the accretion measurement could be performed in any volume of chamber. However, it is more likely that the cell was not completely sealed, and the volume of the cell was not fixed, the volume of the cell was effectively infinite as there was a leak. It is also a possibility that the axial inlet was not situated close enough to the droplet to cause localised changes to the RH inside the cell. It is concluded that further work needs to be done to understand the rate of equilibration of a trapped droplet using a refined experimental set-up.

Throughout chapter 3 further rigorous testing of both systems, OT1 and OT2, was performed. This testing was completed to compare the noise characteristics of all future instruments. The two instruments were shown to be comparable in their noise characteristics and set a baseline for the noise characteristics of future instruments, with specific regard to an instrument designed for detection of CWAs. Further to this, an assessment of the feasibility of introducing gas in the axial orientation was conducted. It is concluded that the introduction of gas with a higher velocity in the axial orientation does not reduce the stability of a levitated droplet. However, the introduction of two gas flows in different orientations was shown to reduce the stability of a levitated droplet. These conclusions should be considered when determining design features of an instrument used to detect CWAs.

In chapter 3, a piece of software was written, which could perform an Allan variance analysis. The software was tested with a sample dataset, which had been manipulated to introduce different types of noise. The software was then applied to data which was taken from 73 droplets using OT1. The droplets had radii between 3 and 7 micrometres. The datasets which could be used for an Allan variance analysis were selected based on the number of missing data points, if the number of missing data points was < 5 % of the dataset, it was possible to fit an Allan variance analysis. Using the Allan variance analysis,

it is recommended that the ideal probe droplet size is between 4-5 micrometres in radius and that the optimal averaging time is on the order of 40 seconds. These conditions will aim to reduce noise in the datasets acquired for detection of CWA and therefore increase the sensitivity threshold for detection. Therefore it is recommended the number of droplets required to coalesce with a probe droplet of 4 – 5 micrometres to show a reasonable change in either droplet radius or RI was calculated for 7 CWAs.

A set of experiments was performed to investigate which of the retrieved droplet parameters should be used to obtain the highest level of instrument sensitivity. In this case, the wavelength of the TE1 whispering gallery mode was explored as a possible metric for droplet radius and the mode offset was explored as a possible metric for RI. This was done to understand whether the surrogate measurements of radius and RI were more appropriate than the current live fitting for the detection of CWAs. It was found that although the wavelength of a WGM is much more precise than the fitted radius, the mode offset is very imprecise as a surrogate for RI. Performing the fitting of the full WGM mode set using the LARA software is the most appropriate methodology to assess the change in composition of a sampling droplet.

In conclusion, the experiments in chapter 4 have addressed the challenges associated with measuring the accretion of aerosol into a trapped probe droplet. Several accretion measurements have been successfully performed on both the OT1 and OT2 systems. Through the calculation of the dry mass of the probe droplet, it was possible to determine the rate of mass flux into the probe droplet, giving a rate of accretion. Accretion rates ranged between 1.7×10^{-4} to 0.2 pg s^{-1}, these accretion rates are comparable to those presented in work prior to this thesis, meaning that the detection of CWAs is possible using the AOT technique.[54] At the highest accretion rate a 4 micrometre probe droplet would require exposure to ~ 2 droplets of pure Tabun with a radius = 0.4 micrometres, adding 2.8 pg of Tabun to a 4 micrometre probe droplet over 1 second to observe a 2 nm change in radius. Naturally, a CWA is unlikely to exist as a pure aerosol droplet, but this accretion rate gives an idea of the potential limit of detection when the accretion rate is maximised.

The accretion experiments performed in this chapter were more refined than previous accretion rate measurements. Specifically, the design of the aerosol delivery system has been rigorously tested to optimise mass flux of aerosol into the probe droplet. Using OT1, a study of the stability in relative humidity when the cell was supplied with only the atomizer solution, was performed. It was concluded that the atomizer was most efficient at stabilising the cell RH when set up in non-recirculation mode. It was also concluded that

the introduction of aerosol should be as a minor component of a continuous RH controlled gas flow. This was found due to the enhanced stability in RH and droplet stability in the trap when the aerosol and gas flow were combined. On OT1 accretion rates between 1×10^{-3} to 0.2 pg s^{-1} were observed. Due to the lack of available MFCs an unreliable bubble valve was used to determine gas flow rate. It was found that the flow rate of the aerosol had little impact on the accretion rate, the primary influence was thought to be the mass concentration of aerosol.

A study of the mass concentration of aerosol passed through the cell during accretion was performed on OT2. This new setup involved two buffering volumes before and after the cell. An additional dilution flow was added to the bag before the cell to change the mass concentration of aerosol directed into the cell. As the flow rate of diluting humidified nitrogen increased, the rate of accretion tended to decrease. It was shown that a higher mass concentration of aerosol passed through the cell resulted in a higher accretion rate. An additional study into the impact of aerosol inlet orientation was performed. Experiments in which the aerosol was introduced in the axial orientation tended to have higher rates of accretion, suggesting that the expanding optical trap above the trapped droplets enhances the rate of accretion. It is hypothesized that the optical forces act to funnel the aerosol towards the trapped droplet. The rate of accretion on OT2 was 0.118 pg s^{-1} when the aerosol was introduced in the axial orientation, yet the accretion rate 0.047 pg s^{-1} when the aerosol was introduced in the radial orientation. More work is required to fully substantiate this hypothesis.

Overall, this thesis confirms the potential of the AOT as a technique for detecting CWAs, presents a procedure with a defined baseline, for benchmarking the noise characteristics of any future research grade optical tweezer instruments for detecting CWA. More work is required to determine the effect of cell volume on droplet equilibration rate, which could further improve the accretion rate, decreasing the time required for a detection event to occur. This would be valuable for the end user of a CWA detector as it would decrease the exposure time before detection of a CWA is completed. More experimental work is required to further enhance the rate of accretion, by improving the design characteristics of the aerosol delivery apparatus. It is thought that optimizing the combination of gas flow with aerosol sample will increase the stability of the probe droplet in the cell and enhance the probe droplet rate of equilibration. Future work should also address the possibility of detecting aerosol and or vapour phase CWAs to understand the limitations of the technique. The work in this thesis indicates that the detection of CWAs with AOT is possible due to

the high sensitivity of the technique, and that a thoughtfully designed instrument has potential for a detector of aerosol phase CWAs.

6. Bibliography

1 W. C. Hinds, *Aerosol technology : properties, behavior, and measurement of airborne particles*, Wiley, 1999.

2 A. Haddrell and J. P. Reid, *Real-time Sampling of Aerosol by Coalescence Capture: Dependence on Aerosol Size Distribution DSTL/AGR/00264/01 – Task 3 15*, 2016, vol. 1.

3 P. V. Hobbs, *Aerosol--cloud--climate interactions*, Academic Press, 1993.

4 T. Hussein, A. Puustinen, P. P. Aalto, J. M. Mäkelä, K. Hämeri and M. Kulmala, *Atmos. Chem. Phys.*, 2004, **4**, 391–411.

5 K. Kim, O. G. Tsay, D. A. Atwood and D. G. Churchill, *Chem. Rev.*, 2011, **111**, 5345–5403.

6 United States Environmental Protection Agency, https://www.epa.gov/, (February 2018).

7 A. A. Fatah, R. D. Arcilesi, J. C. Peterson, C. H. Lattin, C. Y. Wells and J. A. Mcclintock, *Guide for the Selection of Chemical Detection Equipment for Emergency First Responders, 3 rd Edition Guide 100-06 Supersedes DHS Guide 100-04, Guide for the Selection of Chemical Agent and Toxic Industrial Material Detection Equipment for Emergency First Responders, Volume I and Volume II, dated March 2005 1*, 2007.

8 LCD 3.3 - Person worn CWA and TIC detector | Smiths Detection, https://www.smithsdetection.com/products/lcd-3-3/, (accessed 1 August 2018).

9 Y. Sun, K. Y. Ong and CRC Press., *Detection technologies for chemical warfare agents and toxic vapors*, CRC Press, 2005.

10 H. H. Hill and G. Simpson, *F. Anal. Chem. Technol.*, 1997, **1**, 119–134.

11 Detection, https://www.opcw.org/our-work/assistance-protection/protection-against-chemical-weapons/detection/, (accessed 1 August 2018).

12 U. N. Organisation for the prohibition of Chemical Weapons, Detection of Chemical Weapons, https://www.opcw.org/our-work/assistance-protection/protection-against-chemical-weapons/detection/, (accessed 1 August 2018).

13 M. Liudvikas Jagminas, CBRNE - Chemical Decontamination: Overview, Purpose of Chemical Decontamination, Recognizing a Chemical Contamination, https://emedicine.medscape.com/article/831175-overview, (accessed 1 August

2018).

14 F. A. Cotton and D. M. L. Goodgame, *J. Am. Chem. Soc.*, 1960, **82**, 5771–5774.

15 F. A. Cotton, R. D. Barnes and E. Bannister, *J. Chem. Soc.*, 1960, **0**, 2199–2203.

16 H. J. VanTreeck, D. R. Most, B. A. Grinwald, K. A. Kupcho, A. Sen, M. D. Bonds and B. R. Acharya, *Sensors Actuators B Chem.*, 2011, **158**, 104–110.

17 J. C. Sheldon and S. Y. Tyree, *J. Am. Chem. Soc.*, 1958, **80**, 4775–4778.

18 S. O. Obare, C. De, W. Guo, T. L. Haywood, T. A. Samuels, C. P. Adams, N. O. Masika, D. H. Murray, G. A. Anderson, K. Campbell and K. Fletcher, *Sensors*, 2010, **10**, 7018–7043.

19 R. M. Crooks and A. J. Ricco, *Acc. Chem. Res.*, 1998, **31**, 219–227.

20 A. L. Jenkins, O. Manuel Uy and G. M. Murray, *Anal. Commun.*, 1997, **34**, 221–224.

21 V. Pavlov, Y. Xiao and I. Willner, *Nano Lett.*, 2005, **5**, 649–653.

22 EZRaman-I Series High Performance Portable Raman Spectrometer, http://www.tsi.com/EZRaman-Portable-Raman-Spectrometer/, (accessed 28 March 2018).

23 X. Hou, Y. He and B. T. Jones, *Appl. Spectrosc. Rev.*, 2004, **39**, 1–25.

24 TruScan™ RM Handheld Raman Analyzer, https://www.thermofisher.com/order/catalog/product/TRUSCANRM, (accessed 28 March 2018).

25 ThermoFisher Scientific, FirstDefender™ RMX Handheld Chemical Identification, https://www.thermofisher.com/order/catalog/product/FIRSTDEFENDERRMX, (accessed 1 August 2018).

26 Snowy Range Instruments, CBEx - SnRI, http://www.wysri.com/cbex/, (accessed 1 August 2018).

27 Agilent, Resolve – Through-Barrier Handheld Detection | Agilent, https://www.agilent.com/en/products/raman-spectroscopy/raman-spectroscopy-systems/handheld-chemical-identification/resolve, (accessed 1 August 2018).

28 Z. Zhang, R. J. Clewes, C. R. Howle and D. T. Reid, *Opt. Lett.*, 2014, **39**, 6005.

29 A. E. Haddrell, J. P. Reid, *Real-Time Sampling of Aerosol by Coalesence Capture: Dependence on Aerosol Size Distribution*, 2016.

30 C. F. Bohren and D. R. Huffman, Eds., *Absorption and Scattering of Light by Small Particles*, Wiley-VCH Verlag GmbH, Weinheim, Germany, 1998.

31 P. Kulkarni, P. A. (Paul A. Baron and K. Willeke, *Aerosol measurement : principles, techniques, and applications*, Wiley, 2011.

32 A. Marsh, R. E. H. Miles, G. Rovelli, A. G. Cowling, L. Nandy, C. S. Dutcher and

J. P. Reid, *Atmos. Chem. Phys.*, 2017, **17**, 5583–5599.

33 Y. Y. Su, A. Marsh, A. E. Haddrell, Z. M. Li and J. P. Reid, *J. Geophys. Res. Atmos.*, 2017, **122**, 12,317-12,334.

34 A. E. Haddrell, J. F. Davies, R. E. H. Miles, J. P. Reid, L. A. Dailey and D. Murnane, *Int. J. Pharm.*, 2014, **463**, 50–61.

35 C. Peng, M. N. Chan and C. K. Chan, *Environ. Sci. Technol.*, 2001, **35**, 4495–4501.

36 L. Tognotti, J. P. Longwell and A. F. Sarofim, *Symp. Combust.*, 1991, **23**, 1207–1213.

37 N. Hoffmann, A. Kiselev, D. Rzesanke, D. Duft and T. Leisner, *Atmos. Meas. Tech*, 2013, **6**, 2373–2382.

38 R. Tuckermann, S. Bauerecker and H. K. Cammenga, *Int. J. Thermophys.*, 2005, **26**, 1583–1594.

39 Y. Tian, R. G. Holt and R. E. Apfel, *Rev. Sci. Instrum.*, 1995, **66**, 3349–3354.

40 Y. Tian, R. G. Holt and R. E. Apfel, *J. Colloid Interface Sci.*, 1997, **187**, 1–10.

41 R. Tuckermann, S. Bauerecker and H. K. Cammenga, *Aspects*, 2007, **309**, 198–201.

42 H. Schiffter and G. Lee, *J. Pharm. Sci.*, 2007, **96**, 2274–2283.

43 W. Ran, J. R. Saylor and R. G. Holt, *J. Aerosol Sci.*, 2014, **67**, 104–118.

44 M. I. Cotterell, B. J. Mason, A. E. Carruthers, J. S. Walker, A. J. Orr, -4 Ewing and J. P. Reid, *J. P. Phys. Chem. Chem. Phys.*, 2014, **16**, 2118–2128.

45 M. I. Cotterell, T. C. Preston, A. J. Orr-Ewing and J. P. Reid, *Aerosol Sci. Technol.*, 2016, **50**, 1077–1095.

46 T. C. Preston, B. J. Mason, J. P. Reid, D. Luckhaus and R. Signorell, *J. Opt. (United Kingdom)*, 2014, **16**, 25702–11.

47 J. W. Lu, M. Isenor, E. Chasovskikh, D. Stapfer and R. Signorell, *Rev. Sci. Instrum.*, 2014, **85**, 95107.

48 A. E. Carruthers, J. S. Walker, A. Casey, A. J. Orr-Ewing and J. P. Reid, *Phys. Chem. Chem. Phys.*, 2012, **14**, 6741.

49 C. Cai, D. J. Stewart, T. C. Preston, J. S. Walker, Y.-H. Zhang and J. P. Reid, *Phys. Chem. Chem. Phys.*, 2014, **16**, 3162.

50 G. Hargreaves, N. O. A. Kwamena, Y. H. Zhang, J. R. Butler, S. Rushworth, S. L. Clegg and J. P. Reid, *J. Phys. Chem. A*, 2010, **114**, 1806–1815.

51 J. S. Walker, J. B. Wills, J. P. Reid, L. Wang, D. O. Topping, J. R. Butler and Y.-H. Zhang, *J. Phys. Chem. A*, 2010, **114**, 12682–12691.

52 R. M. Power, S. H. Simpson, J. P. Reid and A. J. Hudson, *Chem. Sci.*, 2013, **4**, 2597.

53 R. D. Davis, S. Lance, J. A. Gordon, S. B. Ushijima and M. A. Tolbert, *Proc. Natl. Acad. Sci. U. S. A.*, 2015, **112**, 15815–20.

54 A. E. Haddrell, R. E. H. Miles, B. R. Bzdek, J. P. Reid, R. J. Hopkins and J. S.

Walker, *Anal. Chem.*, 2017, **89**, 2345–2352.

55 J. H. Seinfeld and S. N. Pandis, *Atmospheric chemistry and physics : from air pollution to climate change*, J. Wiley, 2006.

56 A. E. Haddrell, J. S. Walker and J. P. Reid, *Optical Manipulation and Characterisation of Aerosols: Approaches for Real-Time Sampling of Aerosol by Coalescence Capture*, 2015.

57 K. J. Knox, *Light-Induced Processes in Optically-Tweezed Aerosol Droplets*, Springer Berlin Heidelberg, Berlin, Heidelberg, 2011.

58 N. Magome, M. I. Kohira, E. Hayata, S. Mukai and K. Yoshikawa, *J. Phys. Chem. B*, 2003, **107**, 3988–3990.

59 L. Mitchem and J. P. Reid, *Chem. Soc. Rev.*, 2008, **37**, 756.

60 R. E. H. Miles, J. S. Walker, D. R. Burnham and J. P. Reid, *Phys. Chem. Chem. Phys.*, 2012, **14**, 3037.

61 U. K. Krieger, C. Marcolli and J. P. Reid, *Chem. Soc. Rev.*, 2012, **41**, 6631.

62 S. Ingram, C. Cai, Y.-C. Song, D. R. Glowacki, D. O. Topping, S. O'Meara and J. P. Reid, *Phys. Chem. Chem. Phys.*, 2017, **19**, 31634–31646.

63 B. R. Bzdek, M. R. Pennington and M. V. Johnston, *J. Aerosol Sci.*, 2012, **52**, 109–120.

64 K. J. Zarzana, C. D. Cappa and M. A. Tolbert, *Aerosol Sci. Technol.*, 2014, **48**, 1133–1144.

65 B. R. Bzdek, R. M. Power, S. H. Simpson, J. P. Reid and C. P. Royall, *Chem. Sci.*, 2016, **7**, 274–285.

66 A. Ashkin, *Phys. Rev. Lett.*, 1970, **24**, 156–159.

67 A. Ashkin and J. Dziedzic, *Science (80-.).*, 1987, **235**, 1517–1520.

68 A. Ashkin, J. M. Dziedzic, J. E. Bjorkholm and S. Chu, *Opt. Lett.*, 1986, **11**, 288.

69 E. J. Davis, *Aerosol Sci. Technol.*, 1997, **26**, 212–254.

70 J. W. Lu, A. M. J. Rickards, J. S. Walker, K. J. Knox, R. E. H. Miles, J. P. Reid and R. Signorell, *Phys. Chem. Chem. Phys.*, 2014, **16**, 9819–9830.

71 J. Liu, M. Bergin, H. Guo, L. King, N. Kotra, E. Edgerton and R. J. Weber, *Atmos. Chem. Phys.*, 2013, **13**, 12389–12404.

72 A. Ashkin and J. M. Dziedzic, *Appl. Opt.*, 1981, **20**, 1803.

73 R. Symes, R. M. Sayer and J. P. Reid, *Phys. Chem. Chem. Phys.*, 2004, **6**, 474–487.

74 S. Lee, H. S. Wi, W. Jo, Y. C. Cho, H. H. Lee, S.-Y. Jeong, Y.-I. Kim and G. W. Lee, *Proc. Natl. Acad. Sci.*, 2016, **113**, 13618–13623.

75 S. D. Christesen, *Appl. Spectrosc.*, 1988, **42**, 318–321.

76 G. W. Faris and R. A. Copeland, *Appl. Opt.*, 1997, **36**, 2686.

77 R. Signorell and J. P. Reid, *Fundamentals and applications in aerosol spectroscopy*,

CRC Press, 2011.

78 S. G. Demos, R. N. Raman, S. T. Yang, R. A. Negres, K. I. Schaffers and M. A. Henesian, *Opt. Express*, 2011, **19**, 21050.

79 J. P. Reid and L. Mitchem, *Annu. Rev. Phys. Chem.*, 2006, **57**, 245–271.

80 AOT-100 Aerosol Optical Tweezers Online, https://www.biral.com/product/aot-100-aerosol-optical-tweezers, (February 2018).

81 T. C. Preston and J. P. Reid, *J. Opt. Soc. Am. B*, 2013, **30**, 2113.

82 R. E. H. Miles, J. S. Walker, D. R. Burnham and J. P. Reid, *Phys. Chem. Chem. Phys.*, 2012, **14**, 3037.

83 K. L. Hanford, L. Mitchem, J. P. Reid, S. L. Clegg, D. O. Topping and G. B. McFiggans, *J. Phys. Chem. A*, 2008, **112**, 9413–9422.

84 K. J. Knox, J. P. Reid, K. L. Hanford, A. J. Hudson and L. Mitchem, *J. Opt. A Pure Appl. Opt*,.2007, **9**, 180-188.

85 J. Buajarern, L. Mitchem, A. D. Ward, N. Hendrik Nahler, D. McGloin and J. P. Reid, *J. Chem. Phys.*,2006, **125**, 114506.

86 R. J. Hopkins, L. Mitchem, A. D. Ward and J. P. Reid, *Phys. Chem. Chem. Phys.*, 2004, **6**, 4924.

87 K. J. Knox, D. R. Burnham, L. I. McCann, S. L. Murphy, D. McGloin and J. P. Reid, *J. Opt. Soc. Am. B*, 2010, **27**, 582.

88 S. L. Clegg, P. Brimblecombe and A. S. Wexler, *J. Phys. Chem. A*, 1998, **102**, 2155–2171.

89 G. Rovelli, R. E. H. Miles, J. P. Reid and S. L. Clegg, *Atmos. Chem. Phys.*, 2017, **17**, 4369–4385.

90 M. Gysel, E. Weingartner and U. Baltensperger, *Environ. Sci. Technol.*, 2002, **36**, 63–68.

91 J. S. Walker, PhD Thesis, University of Bristol 2013.

92 *Miles_Report on Deliverable 1_Real Time Aerosol Manipulation and Characterisation*, 2014.

93 D. W. Allan and S. Leschiutta, *Alta Freq.*, 1974, **54**, 221–230.

94 A. E. Haddrell, R. E. Miles, B. R. Bzdek, J. P. Reid, R. J. Hopkins and J. S. Walker, *Anal. Chem.*, 2017, **89**, 2345–2352.

95 P. Spence, V. Gupta, D. J. Stephens and A. J. Hudson, *Eur. Biophys. J.*, 2008, **37**, 1335–49.

96 Signal to Noise Calculator, https://www.princetoninstruments.com/calculators/signal-to-noise.cfm, (accessed 29 July 2018).

97 *Miles_Report on Deliverable 2_Real Time Aerosol Manipulation and*

Characterisation , 2014.

98 Optical Particle Sizer 3330, http://www.tsi.com/optical-particle-sizer-3330/, (accessed 19 April 2018).

99 NanoScan SMPS Nanoparticle Sizer 3910;Spectrometer, http://www.tsi.com/nanoscan_smps_nanoparticle_sizer_3910/, (accessed 19 April 2018).

100 S. C. Wang and R. C. Flagan, *Aerosol Sci. Technol.*, 1990, **13**, 230–240.

101 G. Rovelli, R. E. H. Miles, J. P. Reid and S. L. Clegg, *J. Phys. Chem. A*, 2016, **120**, 4376–4388.

102 Y. Liu and P. H. Daum, *J. Aerosol Sci.*, 2008, **39**, 974–986.

103 M. I. Cotterell, B. J. Mason, T. C. Preston, A. J. Orr-Ewing and J. P. Reid, *Phys. Chem. Chem. Phys.*, 2015, **17**, 15843–15856.

104 G. J. Janz and United States. National Bureau of Standards., *Thermodynamic and transport properties for molten salts : correlation equations for critically evaluated density, surface tension, electrical conductance, and viscosity data*, Published by the American Chemical Society and the American Institute of Physics for the National Bureau of Standards, Washington, D.C. :, 1988.

105 Gas Correction Factors for Thermal-based Mass Flow Controllers, https://www.mksinst.com/docs/ur/MFCGasCorrection.aspx, (accessed 26 April 2018).

106 R. J. Rumble, Ed., in *CRC Handbook of Chemistry and Physics*, CRC Press/Taylor & Francis, Boca Raton, Florida, 98th edn., 2018, pp. 4–79.

107 L. Mitchem and J. P. Reid, *Chem. Soc. Rev.*, 2008, **37**, 756.

108 R. J. Hopkins, L. Mitchem, A. D. Ward and J. P. Reid, *Phys. Chem. Chem. Phys.*, 2004, **6**, 4924–4927.

6. Appendix I

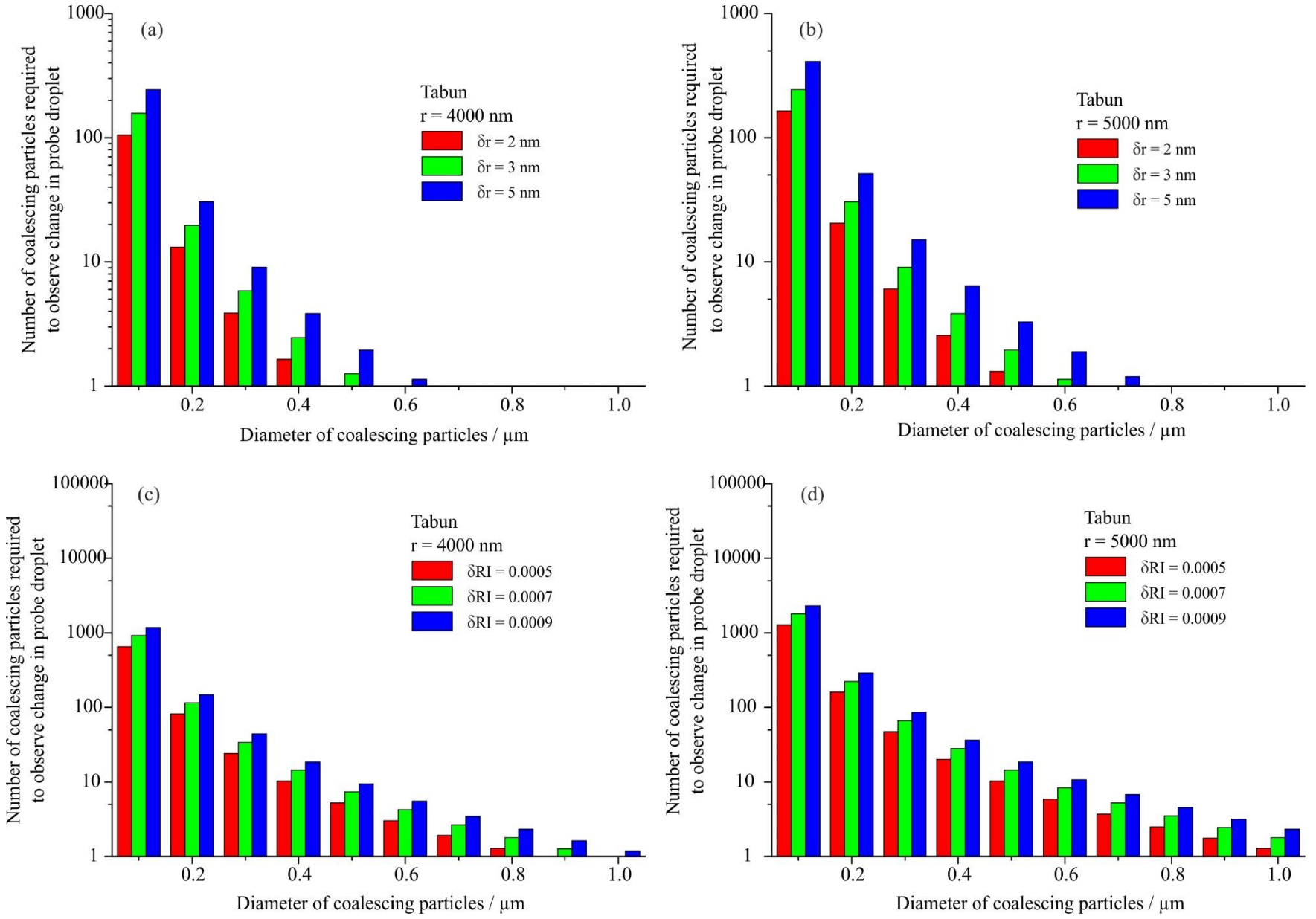
(a)
Tabun
r = 4000 nm
δr = 2 nm
δr = 3 nm
δr = 5 nm
Number of coalescing particles required to observe change in probe droplet
Diameter of coalescing particles / μm
1000
100
10
1
0.2
0.4
0.6
0.8
1.0
(b)
Tabun
r = 5000 nm
δr = 2 nm
δr = 3 nm
δr = 5 nm
Number of coalescing particles required to observe change in probe droplet
Diameter of coalescing particles / μm
(c)
Tabun
r = 4000 nm
δRI = 0.0005
δRI = 0.0007
δRI = 0.0009
Number of coalescing particles required to observe change in probe droplet
Diameter of coalescing particles / μm
100000
10000
1000
100
10
1
(d)
Tabun
r = 5000 nm
δRI = 0.0005
δRI = 0.0007
δRI = 0.0009
Number of coalescing particles required to observe change in probe droplet
Diameter of coalescing particles / μm

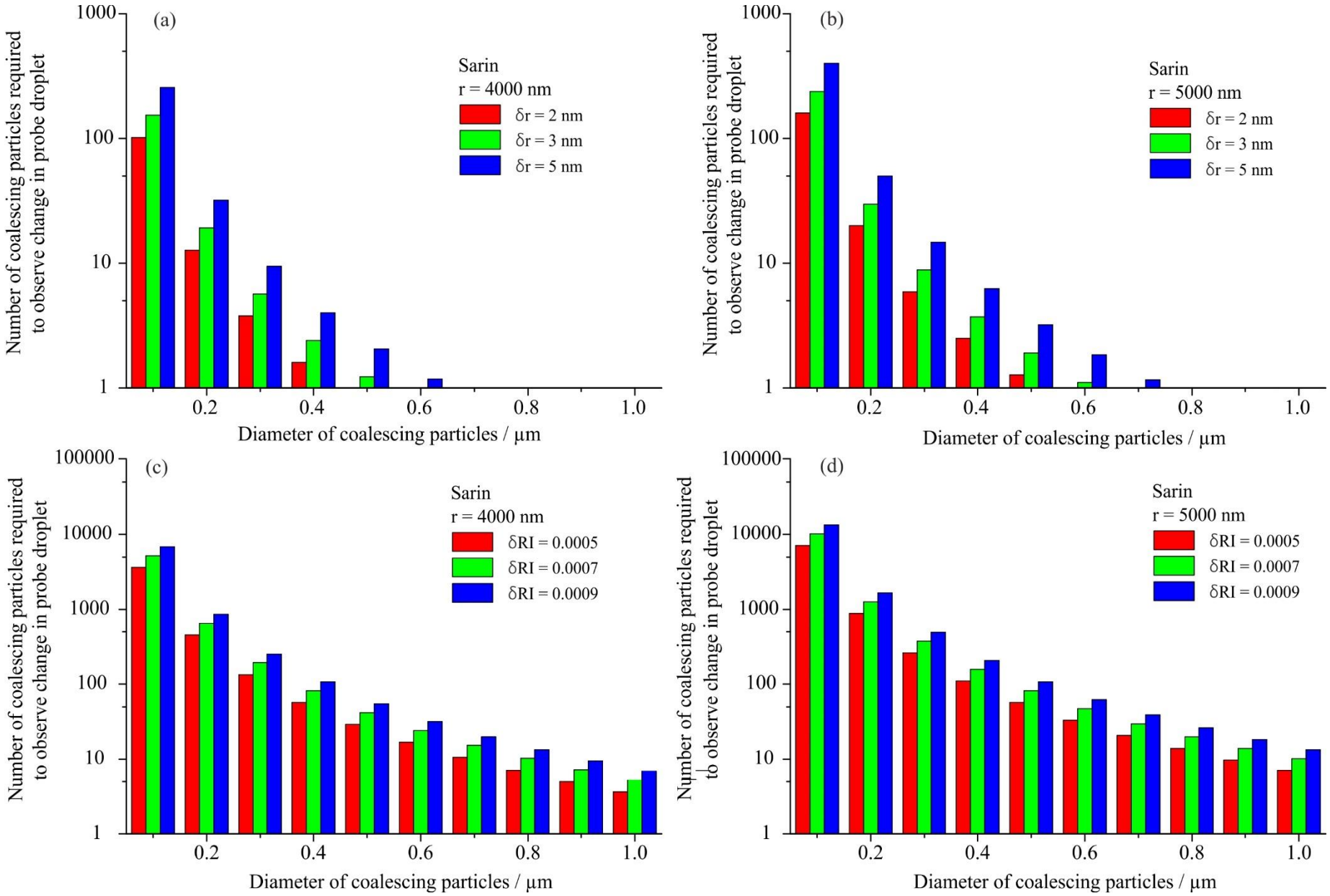
(a)
Sarin
r = 4000 nm
δr = 2 nm
δr = 3 nm
δr = 5 nm
Number of coalescing particles required to observe change in probe droplet
Diameter of coalescing particles / μm
1000
100
10
1
0.2
0.4
0.6
0.8
1.0
(b)
Sarin
r = 5000 nm
δr = 2 nm
δr = 3 nm
δr = 5 nm
Number of coalescing particles required to observe change in probe droplet
Diameter of coalescing particles / μm
(c)
Sarin
r = 4000 nm
δRI = 0.0005
δRI = 0.0007
δRI = 0.0009
Number of coalescing particles required to observe change in probe droplet
Diameter of coalescing particles / μm
100000
10000
1000
(d)
Sarin
r = 5000 nm
δRI = 0.0005
δRI = 0.0007
δRI = 0.0009
Number of coalescing particles required to observe change in probe droplet
Diameter of coalescing particles / μm

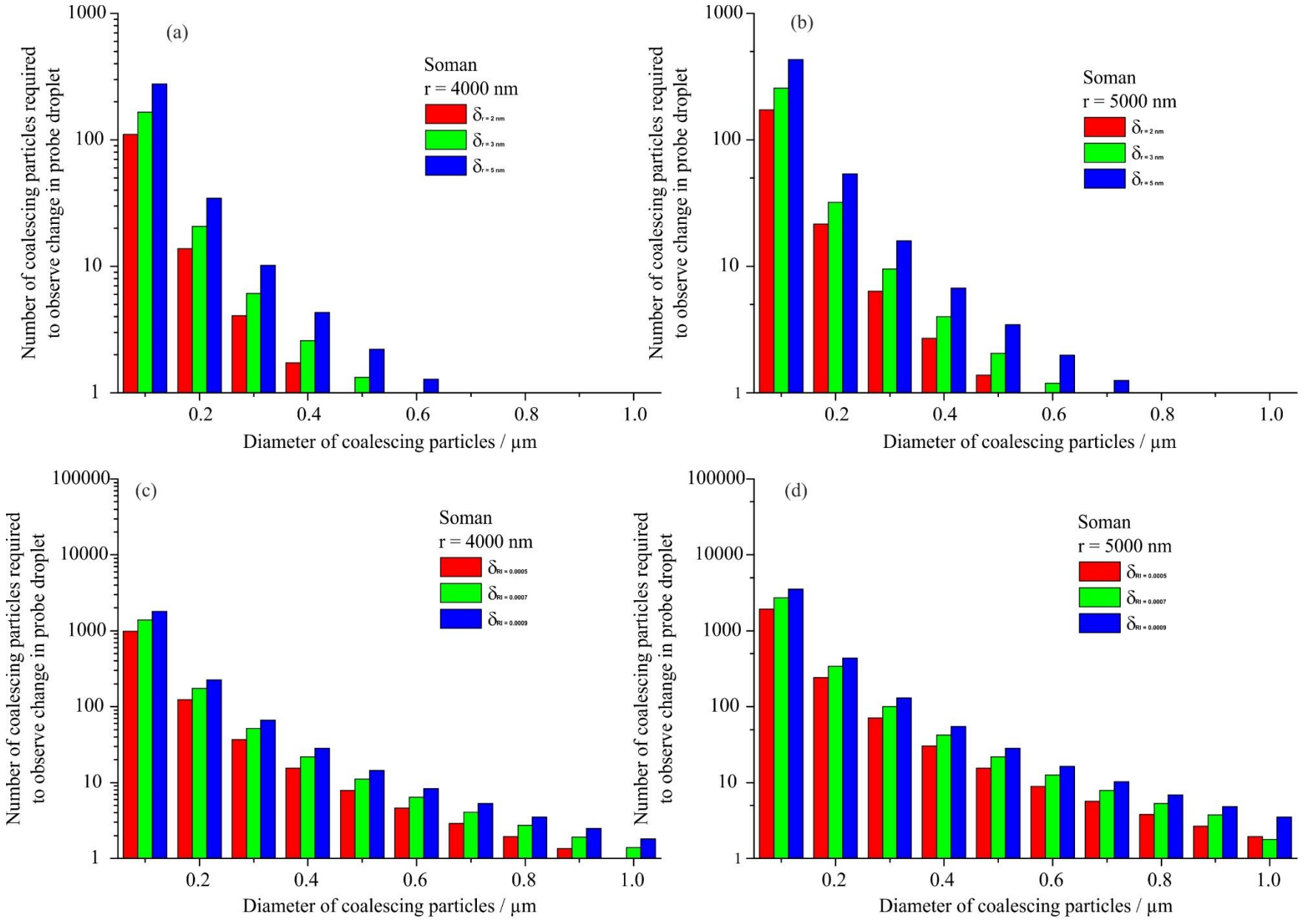
(a)
Soman
r = 4000 nm
δr = 2 nm
δr = 3 nm
δr = 5 nm
Number of coalescing particles required to observe change in probe droplet
Diameter of coalescing particles / μm
(b)
Soman
r = 5000 nm
δr = 2 nm
δr = 3 nm
δr = 5 nm
Number of coalescing particles required to observe change in probe droplet
Diameter of coalescing particles / μm
(c)
Soman
r = 4000 nm
δRI = 0.0005
δRI = 0.0007
δRI = 0.0009
Number of coalescing particles required to observe change in probe droplet
Diameter of coalescing particles / μm
(d)
Soman
r = 5000 nm
δRI = 0.0005
δRI = 0.0007
δRI = 0.0009
Number of coalescing particles required to observe change in probe droplet
Diameter of coalescing particles / μm

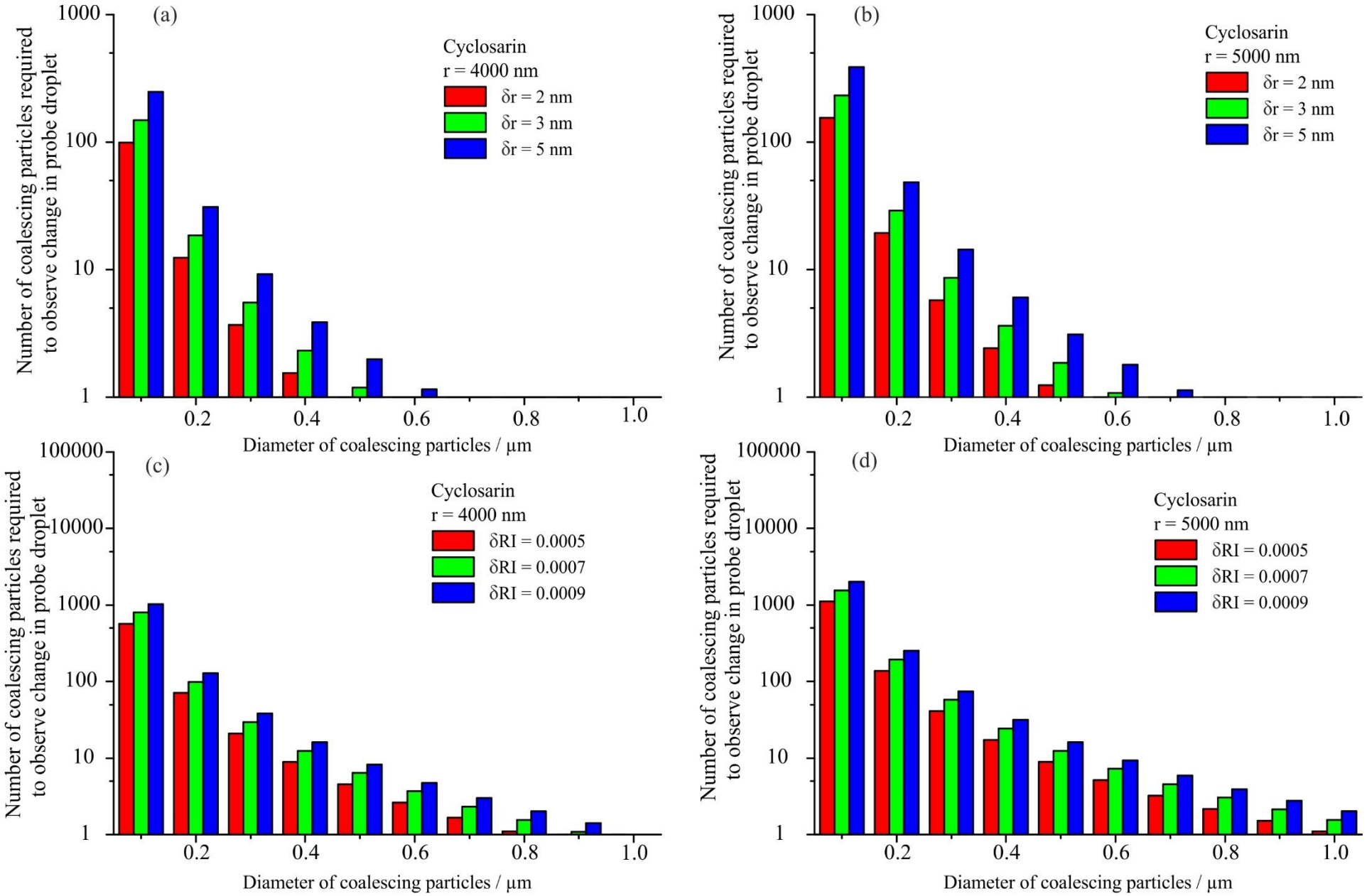
(a)
Cyclosarin
r = 4000 nm
δr = 2 nm
δr = 3 nm
δr = 5 nm
Number of coalescing particles required to observe change in probe droplet
Diameter of coalescing particles / μm
(b)
Cyclosarin
r = 5000 nm
δr = 2 nm
δr = 3 nm
δr = 5 nm
Number of coalescing particles required to observe change in probe droplet
Diameter of coalescing particles / μm
(c)
Cyclosarin
r = 4000 nm
δRI = 0.0005
δRI = 0.0007
δRI = 0.0009
Number of coalescing particles required to observe change in probe droplet
Diameter of coalescing particles / μm
(d)
Cyclosarin
r = 5000 nm
δRI = 0.0005
δRI = 0.0007
δRI = 0.0009
Number of coalescing particles required to observe change in probe droplet
Diameter of coalescing particles / μm

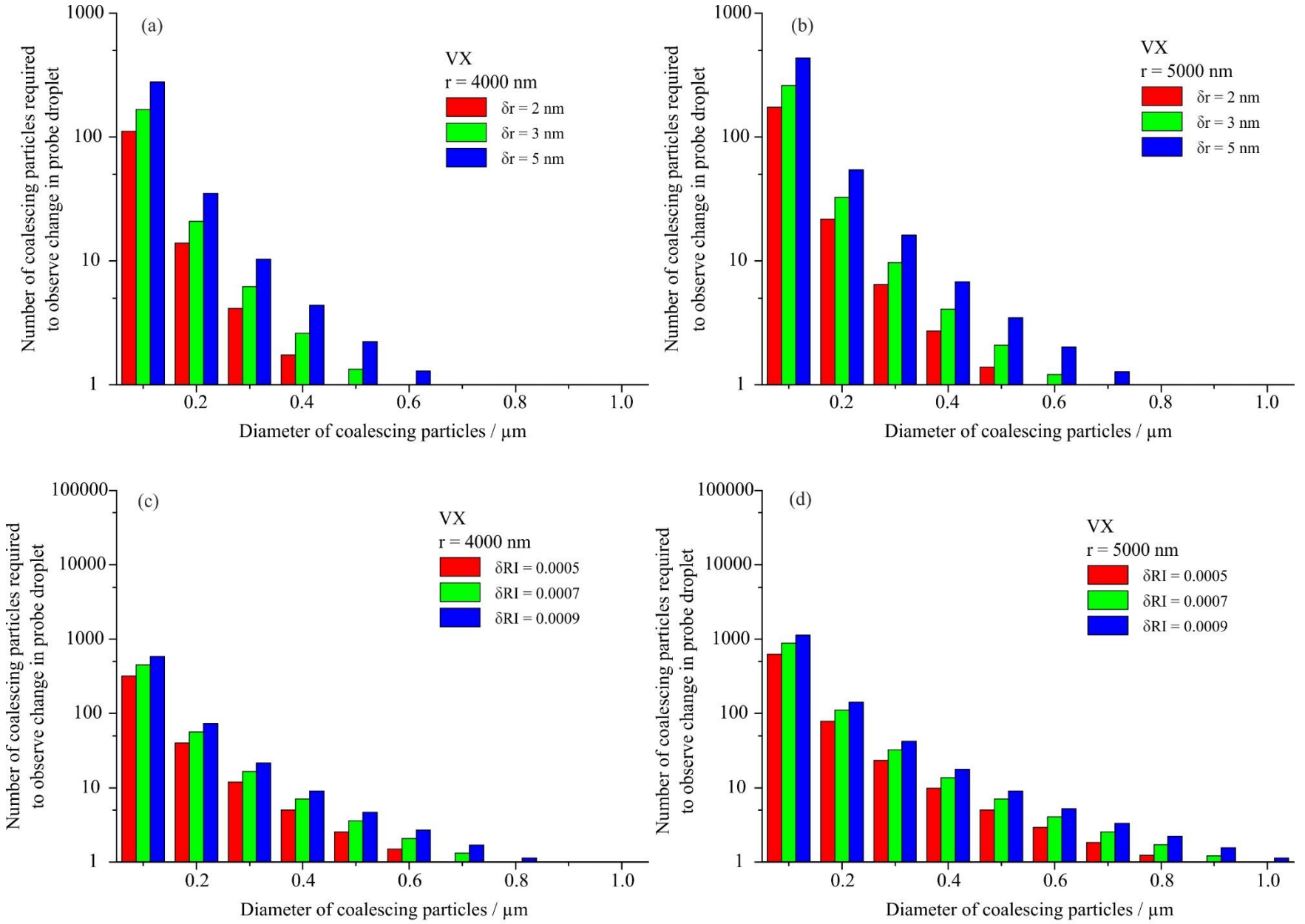
(a)
VX
r = 4000 nm
δr = 2 nm
δr = 3 nm
δr = 5 nm
Number of coalescing particles required to observe change in probe droplet
Diameter of coalescing particles / µm
1000
100
10
1
0.2
0.4
0.6
0.8
1.0
(b)
VX
r = 5000 nm
δr = 2 nm
δr = 3 nm
δr = 5 nm
Number of coalescing particles required to observe change in probe droplet
Diameter of coalescing particles / µm
(c)
VX
r = 4000 nm
δRI = 0.0005
δRI = 0.0007
δRI = 0.0009
Number of coalescing particles required to observe change in probe droplet
Diameter of coalescing particles / µm
100000
10000
1000
(d)
VX
r = 5000 nm
δRI = 0.0005
δRI = 0.0007
δRI = 0.0009
Number of coalescing particles required to observe change in probe droplet
Diameter of coalescing particles / µm

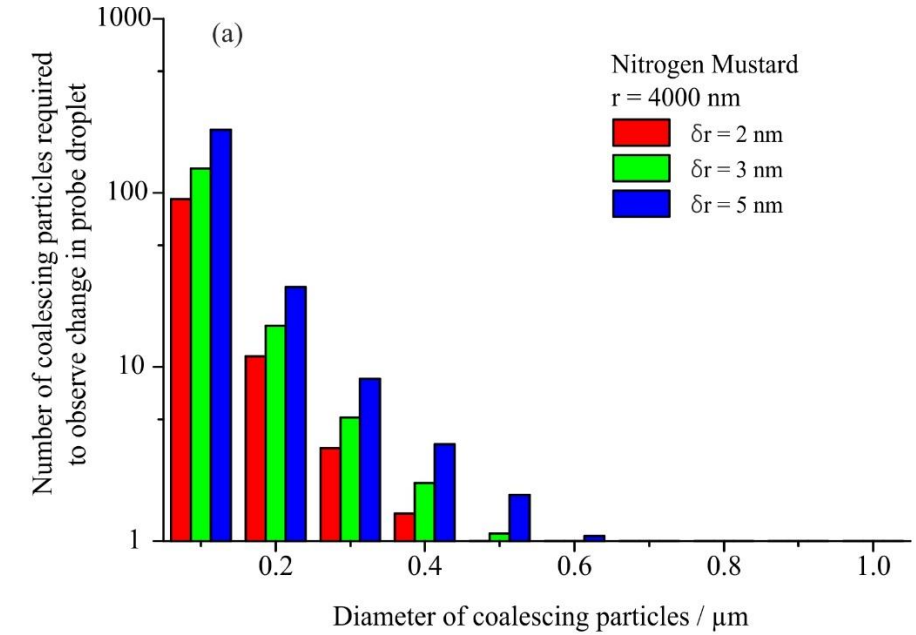
(a)
Nitrogen Mustard
r = 4000 nm
δr = 2 nm
δr = 3 nm
δr = 5 nm
Number of coalescing particles required to observe change in probe droplet
Diameter of coalescing particles / μm
1000
100
10
1
0.2
0.4
0.6
0.8
1.0

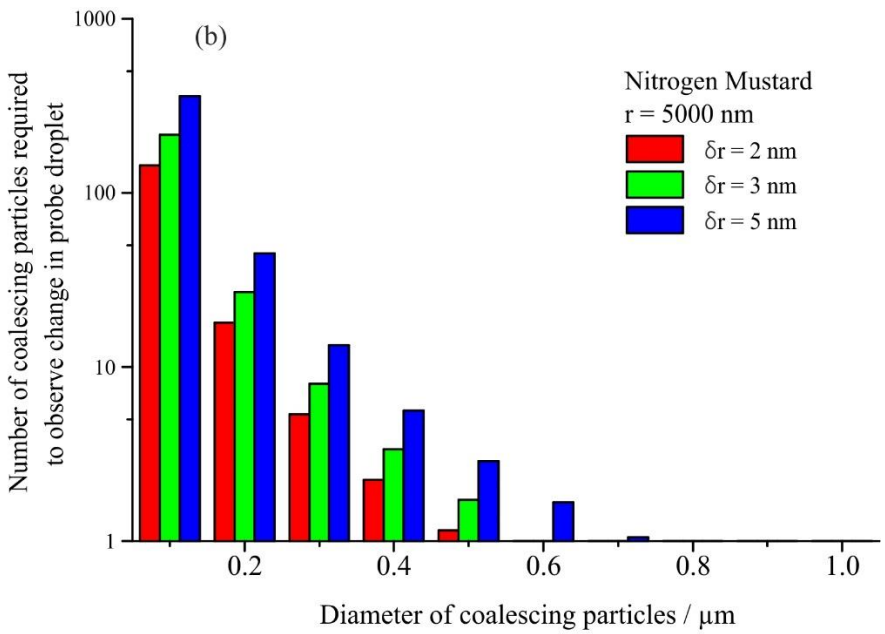
(b)
Nitrogen Mustard
r = 5000 nm
δr = 2 nm
δr = 3 nm
δr = 5 nm
Number of coalescing particles required to observe change in probe droplet
Diameter of coalescing particles / μm
1000
100
10
1
0.2
0.4
0.6
0.8
1.0

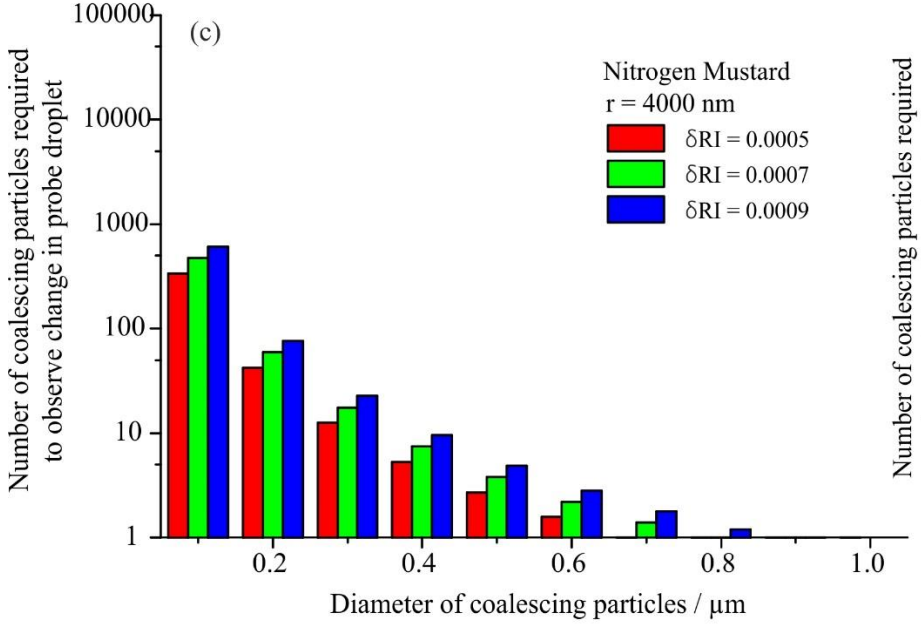
(c)
Nitrogen Mustard
r = 4000 nm
δRI = 0.0005
δRI = 0.0007
δRI = 0.0009
Number of coalescing particles required to observe change in probe droplet
Diameter of coalescing particles / μm
100000
10000
1000
100
10
1
0.2
0.4
0.6
0.8
1.0

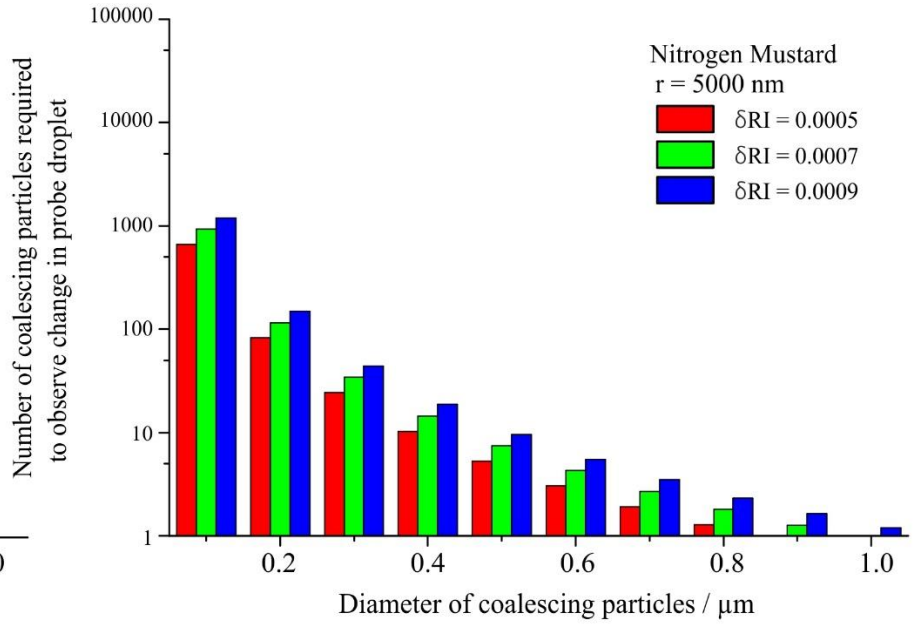
Nitrogen Mustard
r = 5000 nm
δRI = 0.0005
δRI = 0.0007
δRI = 0.0009
Number of coalescing particles required to observe change in probe droplet
Diameter of coalescing particles / μm
100000
10000
1000
100
10
1
0.2
0.4
0.6
0.8
1.0

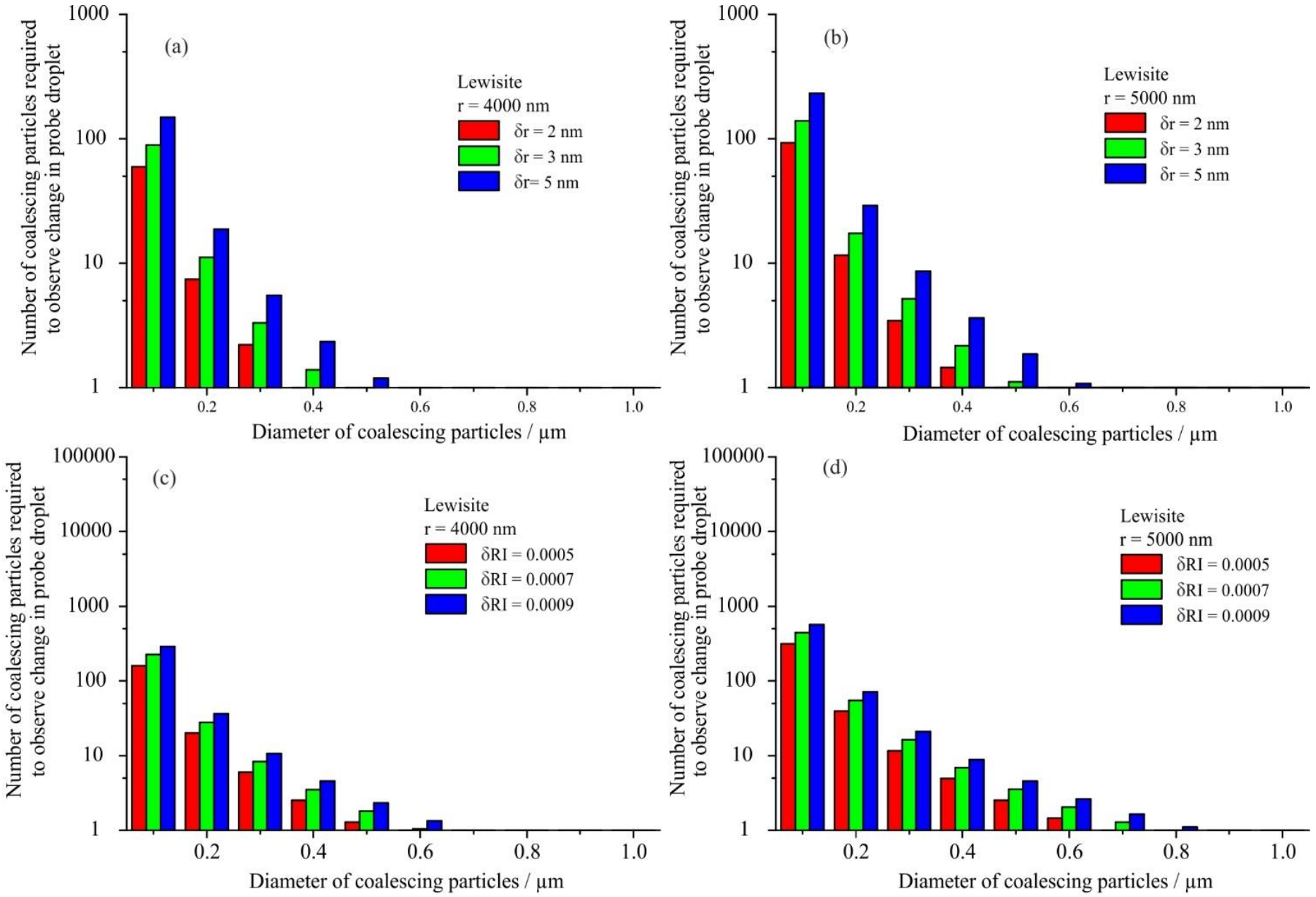
(a)
Lewisite
r = 4000 nm
δr = 2 nm
δr = 3 nm
δr= 5 nm
Number of coalescing particles required to observe change in probe droplet
Diameter of coalescing particles / μm
(b)
Lewisite
r = 5000 nm
δr = 2 nm
δr = 3 nm
δr = 5 nm
Number of coalescing particles required to observe change in probe droplet
Diameter of coalescing particles / μm
(c)
Lewisite
r = 4000 nm
δRI = 0.0005
δRI = 0.0007
δRI = 0.0009
Number of coalescing particles required to observe change in probe droplet
Diameter of coalescing particles / μm
(d)
Lewisite
r = 5000 nm
δRI = 0.0005
δRI = 0.0007
δRI = 0.0009
Number of coalescing particles required to observe change in probe droplet
Diameter of coalescing particles / μm